SOFT MATERIAL-ENABLED FLEXIBLE ELECTRONICS FOR DISEASE DIAGNOSTICS, THERAPEUTICS, AND HEALTHCARE

A Dissertation
Presented to
The Academic Faculty

By

Saswat Mishra

In Partial Fulfillment
of the Requirements for the Degree
Mechanical Engineering in the
Woodruff School of Mechanical Engineering

Georgia Institute of Technology
May 2019

SOFT MATERIAL-ENABLED FLEXIBLE ELECTRONICS FOR DISEASE DIAGNOSTICS, THERAPEUTICS, AND HEALTHCARE

Approved by:

Dr. Woon-Hong Yeo, Advisor
School of Mechanical Engineering
Georgia Institute of Technology

Dr. Seung Woo Lee
School of Mechanical Engineering
Georgia Institute of Technology

Dr. Todd Sulchek
School of Mechanical Engineering *Georgia Institute of Technology*

Dr. Markondeya Raj Pulugurtha
School of Electrical Engineering
Georgia Institute of Technology

Dr. Peter J. Hesketh
School of Mechanical Engineering
Georgia Institute of Technology

Date Approved: December 3rd, 2018

ACKNOWLEDGEMENTS

I would like to express my sincerest gratitude to my advisor, Dr. Woon-Hong Yeo. Without his perseverance and dedication towards scientific research, I would not have been able to successfully publish in high impact factor journals. His guidance has taken me through two schools and multi-disciplinary engineering projects.

I would also like to express my gratitude to my committee members, Dr. Todd Sulchek, Dr. Markondeya Raj, Dr. Peter Hesketh, and Dr. Seung Woo Lee for all their feedback during proposal leading up to my dissertation.

I would like to thank my lab mates from the past 3 years, Dr. Yongkuk Lee, Dr. Yun Soung Kim, Dr. Youngtae Kwon, Dr. Hyoryoung Lim, Musa Mahmood, Robert Herbert, Shinjae Kwon, Dong Sup Lee, and Nicolas Agee.

I had the privilege of working with many brilliant people from IEN at Georgia tech such as Richard Shafer, who would always provide me with insightful technical advice as well as basic life advice.

I would like to thank my family for all their support without their support I would not have persevered.

Finally, I would like to thank my fiancée and her family for all the motivation and confidence that they instilled me with.

TABLE OF CONTENTS

ACKNOWLEDGEMENTS iii

LIST OF TABLES vi

LIST OF FIGURES vii

LIST OF SYMBOLS AND ABBREVIATIONS xvi

SUMMARY xviii

CHAPTER 1. Introduction 1
1.1 Overview 1
1.2 Problem Statement and Objectives 6
1.3 Thesis Organization 9

CHAPTER 2. Literature Review 10
2.1 Disease Prevention and Therapeutics 10
2.2 Biopotentials and Biomedical Instrumentation 12
2.3 Human-Machine Interfaces 13
2.4 Eye Vergence Monitoring and Therapeutics 14
2.5 Wearable Devices: Skin Electronics 16
2.6 Fabrication Methods 19
2.6.1 Photolithography and microfabrication 19
2.6.2 Screen Printing 20
2.6.3 Inkjet Printing 20
2.6.4 Aerosol Jet Printing 21

CHAPTER 3. Electrooculograms for Human-Machine Interface 24
3.1 Methods for Electrooculogram – HMI 25
3.1.1 Finite element analysis 25
3.1.2 Fabrication of a soft bioelectrode 26
3.1.3 Measurement of mechanical behavior 27
3.1.4 In vivo measurement of EOG 29
3.1.5 Data acquisition 30
3.1.6 Human-wheelchair interface 30
3.1.7 Design and characterization of a soft electrode 31
3.2 Measurement of EOG Signals 33
3.3 Classification of EOG signals 37
3.4. Demonstration of a human-wheelchair interface 46
3.4 Summary 50

CHAPTER 4. Aerosol Jet Printing Processing and Characterizations 51
4.1 Overview 51
4.2 Methods and Limitations 52
4.3 AJP films characterization and results 55

4.3.1 AJP printed metals and polymers sintering experiment 56
4.3.2 AJP atomic characterization 59
4.3.3 Conclusion 61
4.4 AJP skin-electrode fabrication 62
4.5 Conclusion 69

CHAPTER 5. Electroculograms for Convergence Insufficiency 70
5.1 Overview of eye vergence and skin-electrode 71
5.2 Study of ocular vergence and electrode Positioning 78
5.3 Eye vergence optimization with signal processing and feature selection 81
5.4 Comparison of ocular classification accuracy between virtual reality and physical apparatus 85
5.5 VR-enabled vergence therapeutic system 88
5.6 Summary 91

CHAPTER 6. Radio Frequency Identification of Salivary Electrolytes 93
6.1 UHF-RFID Tag Fabrication and Programming 94
6.2 *In vitro* and *In vivo* methods and measurements of sodium 96
6.3 Summary 99

CHAPTER 7. Future Work 101
7.1 Summary and original contribution 101
7.1.1 Novelties - Chapter 3 103
7.1.2 Novelties – Chapter 4 104
7.1.3 Novelties – Chapter 5 104
7.1.4 Novelties – Chapter 6 105
7.2 Future direction 105
7.2.1 Fabrication expert 105
7.2.2 Aerosol Jet Printing expert 106
7.2.3 Classification and Algorithm expert 106
7.2.4 Circuit Design expert 107
7.2.5 Ocular applications expert 107

REFERENCES 109

LIST OF TABLES

Table 1	Table 1. Comparison of the classification accuracy between conventional and fractal electrodes (averaged values from three subjects; n=3). TP, FP, FN, and TN stand for true positive, false positive, false negative, and true negative, respectively.	45
Table 2	Root-mean-square values for three trials of conventional and three trials of fractals for all users.	49
Table 3	Literature comparison of this work's EOG-HMI and other EOG systems	50
Table 4	Bulk sample of young's modulus.	54
Table 5	Table 5. Two sets of samples sintered at different temperatures and time in an ambient oven.	58
Table 6	Table 6. Gold sintered at varying temperature and times	59
Table 7	Review of eye vergence studies in comparison to this work.	92
Table 8	Review of RFID data acquisition with various sensing mechanisms and materials.	100

LIST OF FIGURES

Figure 1	Cost of healthcare around the world data provided by International Federation of Health Plans. (a) Inpatient costs (b) Outpatient costs	2
Figure 2	General photolithography process after film deposition [3]**.**	4
Figure 3	Additive Manufacturing techniques in sub-micron, micron, and millimeter resolution. (a) Two-photon polymerization based 3D printing using nanoscribe [4] (b) Aerosol Jet Printing on a carbon fiber 3D part [5]. (c) Fused deposition modelling 3D printing of a prosthesis [**6].**	5
Figure 4	Biopotential recording techniques. (a) Conventional recording setup and (b) output EOG signal. (c) Electromyogram recording setup and (d) electroencephalogram setups are uncomfortable for long term wear.	7
Figure 5	Sensor technologies. (a) Gold-cup based gel electrode (b) Hydrogel adhesive based Ag/AgCl electrode. (c) Dry electrode contact based Ag/AgCl electrode (d) Needle electrode which probes at the closest location to the targeted site.	8
Figure 6	Prevalent health conditions in the United States which effects millions of people. (a) Neurodegenerative diseases such as Parkinson's disease results in loss of motor control due to rigidity as well long term tremors that limits the use of arms and legs. (b) Ocular disorders such as strabismus and vergence insufficiencies can cause learning disorders for children and loss of productivity for adults.	11
Figure 7	Example of human-machine interface controlling a drone with skin-electronics and human-computer interface controlling a game with skin-electronics on throat muscle.	14
Figure 8	Eye vergence apparatus for measuring vergence insufficiency using videooculograms and stereo displays; "gold standard" for ocular measurements [31].	15
Figure 9	Robust and Rigid vs. Soft and Comfortable. (a) Apple watch on the wrist is one of the most sophisticated smart wearables able to classify atrial fibrillation. (b) Soft electronic wearable patch over the heart seamlessly integrates with the human body.	16
Figure 10	Flexible, stretchable circuitry and sensor arrays developed for human health monitoring with elastomers on skin. (a) EEG electrode for temporal lobe measurements [42] (b) Smart wrist band to monitor ionic sweat analytes using potentiometric sensors [46]. (c) Intraoral retainer with a flexible and stretchable circuit placed on an elastomer for	18

measuring sodium analytes [47]. (d) Strain sensor used to measure respiration from the displacement of the diaphragm [43]. (e) Inkjet-printed electrodes for EMG recordings of facial gestures using PEDOT and silver[45]. (f) Graphene/PEDOT:PSS temperature sensor array printed using inkjet**[**44**].**

Figure 11 General drawbacks and advantages of inkjet and aerosol jet printing. 21

Figure 12 Overall integration of HMI with electrooculograms and skin-electrodes 25

Figure 13 Fabrication process. (a) A clean glass side is prepped and PMMA is spin coated. (b) Polyamide is spin coated. (c) Gold is deposited. (d) Photoresist is spin coated. (e) Photoresist is exposed and developed. (f) Gold and chrome is etched. (g) PI is etched. (h) PMMA is dissolved and the electrode is transferred to another elastomer. 26

Figure 14 Transfer process. (a) Electrode on glass slide is ready for transfer. (b) Water-soluble tape is attached to the electrode and peeled off. (c) The peeled electrode is transferred to a thin stretchable elastomer as a substrate and the water-soluble tape is dissolved. (d) A flexible connector is hot pressed onto the electrode contact pads, which is then transferred onto the skin for measurements. (e) EOG recordings are wirelessly transferred via Bluetooth communication onto a laptop for observations. 27

Figure 15 Mechanical stretcher and bending apparatus (a) Photo of an automated mechanical stretcher (top view) with four screw clamps that fix the sample to the stretcher with wire attachment for electrical resistance measurements. (b) The biaxial stretcher (left), multimeter (middle), and data acquisition laptop (right) is used to control the stretcher with a microcontroller and acquire resistance measurements with the multimeter. (c) Photo of bending apparatus at the 0 degree position with the sample attached by its own adhesive properties. (d) The bending apparatus is configured to a stepper motor controlled by the microcontroller. A multimeter acquires resistance measurements of the sample. 29

Figure 16 The design and structure for a “skin-like”, fractal electrode. (a) Dimension of a skin-like electrode. (b) Close-up view of the electrode including circular cells (radius = 500 μm) and fractal interconnects (width = 50 μm). (c) Layer composition of the electrode. 31

Figure 17 Computational modeling and experimental validation of a fractal structured electrode upon mechanical deformation. (a, b, c, d) Comparison between the finite element analysis (FEA) results and experimental observations with (a, b) biaxial tensile strains upto 30% and (c, d) bending upto 180 degrees with the radius of curvature (R) of 33

500 μm. (e, f) Quantification of electrical resistance according to the (e) applied strains and (f) bending; (e) cyclic mechanical test with repetition of loading and unloading and (f) cyclic mechanical bending test. The scale bars in the FEA data indicate the maximum principal strain applied on the electrode.

Figure 18 A representative set of EOG signals involving four kinds of eye movements. (a–d) Direct comparison of raw EOG signals measured from fractal and conventional gel electrodes: signals from (a) eyes 'up' and 'down' motions and (b) 'left' and 'right' motions. Bandpass (0.1–20 Hz) filtered EOG signals from (c) 'up' and 'down' motions and (d) 'left' and 'right' motions. 34

Figure 19 Comparison of electrode sensitivity. (a) An experimental setup targeting a series of circles to measure the angle-dependent EOG sensitivity. (b) Normalized EOG signal amplitudes according to the angle change of an eye where black and yellow bars represent conventional and fractal electrode, respectively. Error bars show the standard deviation (n=3). 35

Figure 20 Comparison of electrode sensitivity. (a-b) Photos of fractal electrodes mounted on the skin (conventional electrode is located on the contralateral site) and the corresponding EOG signals comparing the signal strength between fractal and conventional electrodes. The signal strength is dependent of the electrode size; (a) full size and (b) quarter size electrode. (c) Averaged SNR values comparing the size effect of fractal electrodes with a fixed rigid electrode (error bars from n=8 with the standard deviation). 36

Figure 21 Comparison of infrared thermographs measured with (a) conventional and (b) fractal electrodes to reveal the side effect of the gel contacted to the skin (forearm) for more than 5 h. (c) Photo and thermograph of a gel electrode mounted on the forehead, causing skin rash. 37

Figure 22 Signal processing sequence with a LDA classifier. (a) Raw EOG signals measured from eye movements of "blink" and "down". (b) Preprocessed signals via filtering. (c) Absolute derivative signals to pinpoint target peak signals and apply a threshold boundary. (d) Sliding window algorithm using the detected peaks to parse the dataset into centered signals. (e) Machine learning algorithm using five distinct features from the centered signals and a LDA classifier to distinguish 4 classes of eye movements (up, down, left, and right). 38

Figure 23 Threshold detection is the first of the three logic inputs. 39

Figure 24 Peak detection is the second input of the three. 40

Figure 25	The final input is the window detection which resolves the final window for classification	41
Figure 26	LDA classification of signals in real-time algorithm. (a, b) Comparison of confusion matrix from (a) conventional rigid electrodes and (b) soft fractal electrodes; The averaged classification accuracy from three subjects shows 91.9% and 94.1% for conventional and fractal electrodes, respectively.	43
Figure 27	The final input is the window detection which resolves the final window for classification.	44
Figure 28	Wheelchair interface with microcontroller (a) The wheelchair control board accepts signals for forward, left, right, and neutral for our application. (b) Bluetooth module configures with the tablet; digital to analog converters allow step input to control the speed of the wheelchair. (c) Microcontroller configures the DACs. (d) 3-D printed assembly with layer 1, microcontroller. (e) Layer 2 and Layer 3 incorporate the protoboard module and wheelchair control board. (f) Fully assembled 3-D printed module. (g) Front view of the wheelchair with surface tablet attached. (h) Back view of the wheelchair with data acquisition software. (i) Classification interface from the tablet.	46
Figure 29	(a) Top view of entire pathways of a robotic wheelchair; classified EOG signals from eye movements are wirelessly transmitted from the fractal electrode/DAQ to the wheelchair control interface via Bluetooth. (b) A series of photos capturing a real-time, wireless control of the wheelchair via eye movements. There are four control commands generated by different eye movements including “up”, “right”, “left”, and “down”. Insets show the raw EOG signals in correspondence with the eye movement from a subject.	47
Figure 30	Berkovich tip with a half-angle of 65.3 degrees with a used to calculate the area function for hardness and modulus measurements	52
Figure 31	Loading and unloading curve of the nanoindenter at sample depth of 100 nm.	53
Figure 32	Various materials were printed on a silicon wafer for imaging and characterization. Only material not shown here is the PDMS sample.	55
Figure 33	The different atomization techniques used in this work. (a) Pneumatic atomization with a single jet. (b) Ultrasonic atomization using a piezo transducer for excitation. (c) The aerosol stream is transferred to the deposition print head.	56

Figure 34	Sintered materials at (a) 250 °C for 1 hour and (b) 300 °C for 12 hours with the plotted young's modulus. The PDMS sample was cured at 110 °C	57
Figure 35	The third set of samples were tested for the sinterability of gold at temperatures 200 °C, 250 °C, and 300 °C for 1, 3 and 12 hours.	59
Figure 36	XPS results of (a) silver and (b) gold sample with a change in (c) oxygen adsorbed due to the ambient environment.	60
Figure 37	SEM images of Ag, Au and Ni. (a) Ag sintered at 250 °C for 1 hour; (b) Au sintered at 250 °C for 1 hour; (c) Au sintered at 300 °C for 12 hours; (d) Ni turned into nickel oxide nanoparticles sintered at 200 °C for 1 hour.	61
Figure 38	(a) Aerosol jet printing out of deposition head with a close up of deposition of a skin sensor. (b) Atomization begins in the ultrasonic vial and a carrier gas (N2) flows the ink droplets through tubing, the diffuser, and the deposition head where a sheath gas focuses the particles into a narrow stream with ~ 5 μm diameter.	63
Figure 39	(a) Platen is heated to ensure evaporation of the solvents, but surface treatment with plasma cleaner enables clean lines (top). Otherwise the traces tend to form into low energy bubbles over a large area. (b) High focusing ratio with low width/thickness ratio enables lower resistivity. (c) Resistivity measurements from four point probe was determined for various sintering temperatures and time. (d) Ultimately, the resistance of the electrodes needs to be low so a two point probe measurement demonstrates the resistance across a fractal electrode in series.	64
Figure 40	Design of electrode. Skin-electrode dimensions are 1x1 cm^2 and approximately 1 mm diameter circles. The fractal pattern is maximizing surface area for best contact, but also increases resistance from end-to-end of the electrode. The radius of each curve is 100 μm with a trace width ranging from 20 μm – 60 μm depending on the type process used.Design of electrode. Skin-electrode dimensions are 1x1 cm2 and approximately 1 mm diameter circles. The fractal pattern is maximizing surface area for best contact, but also increases resistance from end-to-end of the electrode. The radius of each curve is 100 μm with a trace width ranging from 20 μm – 60 μm depending on the type process used.	65
Figure 41	(a) AgNPs capped with oleylamine fatty acid that prevents agglomeration ends up breaking down after low temperature and high temperature sintering. The grain size for small NPs increases at low temperatures and then bigger NPs at higher temperatures. (b) SEM images indicate the dissociation of the binder material after sintering (c) XRD analysis shows larger crystallization peaks after sintering and the recrystallization of peaks along (111), (200), and (311) crystal planes.	66

(d) Raman spectroscopy demonstrates the loss off carbon and hydrogen peaks from the binder dissociation near wave number 2900 cm-1.

Figure 42 (a) After atomization and deposition, a full electrode array is ready to be processed by dry etching. There are two options for dry etching, first option is to just go ahead and etch the polyimide after printing and second option (b) is to deposit photoresist onto the silver patterns by alignment. A close up shows the deposition location and the beam diameter of 5 μm. (c) After depositing all electrodes on the substrate, the sample can be treated in oxygen plasma to etch the polyimide. (d) After etching, oxygen has impinged the silver and needs to be reduced or (e) the photoresist stays intact and the silver is untouched but the polyimide is etched away. (f) The final reduction step is conducted in a RIE with argon gas which removes most of the oxygen. (g) The final electrode array comes out of the RIE bright white after removing photoresist or reducing. 68

Figure 43 Therapeutic device with training program and wearable devices for disease diagnoses. (a) Virtual reality headset with skin electrodes are subtly placed underneath the gear VR. (b) Near-> Intermediate -> Distance signals are shown for the electrodes as the user follows the training program for the corresponding color and position. 72

Figure 44 Apparatus for testing eye vergence motions Physical apparatus (top) and Virtual Reality (bot). Dimensions of the (a) physical apparatus consists of positions that approximate to 1º, 2º, and 3º of motion. (b) The VR images are offset for each eye to simulate binocular vision in the real world. 73

Figure 45 (a) A close up of the skin-electrode conformality and small form factor makes it ideal for contoured regions such as the nose. (b) A rolled up flex device can still continue to function with a bending radius of 13 mm. (c) A section in between the ADC and the Bluetooth radio has been bent with a radius of 1 mm showing low strain; the corresponding experimental test shows the device still functional. (d) Further X-ray images along the 13 mm bending radius shows the IC internals and all the soldered components. 74

Figure 46 Flex device fabrication process. (a) Flex device fabrication is possible using a clean silicon wafer on which to build (b) a layer of PMMA and polyimide. (c) Sputter copper and then (d) etch the copper with APS-100. (e) Spin cast two layers of polyimide and etch the holes. (f) Deposit copper to fill in holes and create top interconnect layer. (g) Spin cast polyimide and etch away the top layer. (h) Finished design is ready to transfer after removing any copper oxides using stainless steel flux. 75

Figure 47	Skin electrode and Flex Device transfer process. (a) Flex device is submerged in a bath of acetone at 60 ºC overnight (b) while the skin-electrode is processed in the acetone bath for 1 hour. (c) Use the water soluble tape to transfer the device off the silicon wafer and (d) skin-electrode off the glass slide. (e) Prepare the ecoflex gel and ecoflex 30 mixture for the device and transfer simultaneously prepare the (f) ecoflex gel sample on PVA for the skin-electrodes. (g) Solder the IC chips onto the thin film flex board and (h) attach ACF wires to the skin-electrodes then configure the device and the skin-electrodes together.	76
Figure 48	Experimental bending of EOG Device. Device is compared to the American quarter showing the size of the device. Successive bending of the device from 90°- 180° shows minor fluctuations in resistance and continuous operation of the device. Additional simulations indicate low strain near the bending locations.	77
Figure 49	Skin-mounted above eye and disease diagnostic. (a) An unstretched electrode on the skin near the site of the ocular electrode positions. (b) Electrode is stretched to show the 180 degree bending characteristics (c) Removing the electrode still ensure functional electrode. (d) The strabismus diagnosis of esotropia and (e) exotropia can be extracted from a machine learning classification of numerous patients that can also be transmitted directly to a doctor.	78
Figure 50	Eye vergence signals. (a) Forwards and backwards motion of the eye resemble eye vergence for 1° – 3° of motion. These signals are normalized from 0 to 1 for better clarity.	79
Figure 51	Electrode positioning with corresponding classification results. (a) Conventional EOG positioning based off synchronized eye movement demonstrates (b) low classification accuracy. (c) Ocular vergence 1 positioning with similar number of electrodes as conventional demonstrates much (d) higher classification accuracy. (e) Ocular vergence 2 (f) enhances classification accuracy with individual reference electrodes for each eye.	80
Figure 52	Data preprocessing to feature extraction: (a) Raw signal is acquired real-time via Bluetooth data acquisition unit and its corresponding derivative is shown. (b) The data is preprocessed with a bandpass Butterworth 0 phase filter with the corresponding derivative of that data raised to the second power. (c) The filtered data is further processed with a 500 point median filter and the corresponding derivative is raised to the 6th power. A coefficient is multiplied to increase the amplitude of the 2nd order and 6th order differential filter. (d) A comparison of the 6th order and 2nd order differential filter shows an increased range of the 6th order data by calculating the signal to noise ratio. The 6th order data is used for thresholding the signal for real-time classification of the	82

dataset. (e) The data from the sliding window is inputted into the ensemble subspace classifier which is shown by the decision boundaries of two dimensions of the feature set.

Figure 53 Percent of accuracy with permutations of features from all three channels for position and velocity. 84

Figure 54 Training and testing direction for eye vergence. The procedure for recording and training eye vergence involves following a linear procedure to extract all eye motions equal number of times. (a) Direction 1 and (b) direction 2 are repeated four times. 85

Figure 55 Eye vergence normalized amplitudes and peak velocity for classification results: (a) The normalized signal set with mean and deviation for flex device with subject 11 in VR apparatus and subject 9 with physical device. (b) Peak velocity comparison to normalized amplitude for the ideal case of eye vergence. (c) Cross validation results of subject 11 with flex device in the VR apparatus and subjects 6-10 with the physical apparatus. 86

Figure 56 Normalized eye vergence motions recorded with subjects 6-10 using the physical apparatus. The normalized signals for each user for all vergence motions indicate high variability with signal collection with physical apparatus. 87

Figure 57 Normalized eye vergence motions recorded with subjects 11-13 using the virtual apparatus. The normalized signals for each user for all vergence motions indicate more precise responses in the VR display. 88

Figure 58 Therapeutic programs with corresponding signals and VR Rehabilitation. (a) Brock string program enables customizability of bead distance without the need of a physical object; the corresponding signal pin points the position of the user's vergence motion. (b) Eccentric circle program replaces conventional stereogram activities with customizability of the card distance. The user can practice crossing eyes at different distances to evoke the "third card" in the center. (c) Successive use of our VR program shows preliminary results of increasing accuracy using OV2 electrode positioning. (d) The same electrode positioning can assist in detecting strabismus conditions while using pencil pushups. (e) Pencil pushups evoke a strabismus response in the right eye. 90

Figure 63 Aerosol jet printed fabrication process using unconventional lithography. (a) A 3 micron copper sheet is laminated onto Kapton tape. (b) Photoresist is deposited onto the substrate and (c) the copper is etched. (d) Soldering takes place after placing the substrate onto an elastomer layer. 95

Figure 60	Digital multimeter results. (a) DMM results on the fingers show lower resistance while the (b) wrist location shows higher noise, resistance, and lower sensitivity.	97
Figure 61	Sensor configuration for AMS. (a) Sensor front end configuration on the AMS to be able to read GSR directly from the skin. (b) Sensitivity of the sensor for change in skin resistance of 1 MΩ for load resistors from 1 MΩ - 8 MΩ	98
Figure 62	Sensor recording on the skin. (a) Top and bottom view of the tag on the skin shows the sensor in contact with the skin and the tag pointed up. (b) Data comparison between DMM and skin tag for GSR recordings.	99
Figure 63	Face mold to develop a custom soft material mask for higher precision eye vergence recordings is recommended during therapeutic clinical trials.	108

LIST OF SYMBOLS AND ABBREVIATIONS

ACF	Anisotropic Conductive Film
ADC	Analog-Digital-Converter
Ag	Silver
AgNP	Silver nanoparticle
AJP	Aerosol Jet Printing
BLE	Bluetooth Low Energy
CI	Convergence Insufficiency
CITT	Convergence Insufficiency Treatment Trial
Cu	Copper
DAC	Digital to Analog Converter
DAQ	Data Acquisition
ECG	Electrocardiogram
EEG	Electroencephalography
EMG	Electromyogram
EOG	Electrooculogram
FR	Focusing Ratio
HCI	Human-Computer Interface
HF	High Frequency
HMI	Human-Machine Interface
IoT	Internet of Things
LDA	Linear Discriminant Analysis
Ni	Nickel

OBVT	Office Based Visual Therapy
PA	Pneumatic Atomizer
PDMS	Polydimethysiloxane
PI	Polyimide
PMMA	Polymethylmethacrylate
PVA	Polyvinyl Alcohol
RFID	Radio Frequency Identification
SEM	Scanning Electron Microscopy
SNR	Signal-Noise-Ratio
SNR	Signal-noise-ratio
UA	Ultrasonic Atomizer
UHF	Ultra High Frequency
VOG	Videooculography
VR	Virtual Reality
XPS	Xray photoelectron spectroscopy
XRD	Xray diffraction

SUMMARY

The United States healthcare costs are approaching half a trillion dollars annually while mortality rates continue to rise from neurodegenerative and systemic diseases. Preemptive and therapeutics care is an alternative to expensive surgeries in order to reduce costs. Popularity with wearable devices enables *in vivo* biosensing platforms, but the existing devices are heavy, rigid, and bulky which inherently disrupts high-quality data recording and causes discomfort. This proposal optimizes the mechanics and materials for a soft material platform integrated with open-mesh, serpentine structures for extreme flexibility and stretchability.

However, preventative care is only half the problem for exorbitant health care costs so we dwelled into a wearable platform for ocular therapy systems enabled by electrooculograms. Our therapeutic platform aims to facilitate users from debilitating diseases such as Parkinson disease and convergence insufficiency. The wearable "skin-like" electrodes enhance the recording and classification of ocular signals to control a wheelchair for Parkinson disease patients. Additionally, a similar platform enables us to record contrasting eye vergence motions with a virtual reality headset for home-based visual therapy. In this proposal, a set of materials, mechanics, and system integration methods is presented and discussed to unite preemptive and therapeutic care using electrooculograms with wearable devices.

INTRODUCTION

1.1 Overview

Health care in the United States has ballooned to unprecedented costs with the improvement of medical devices over the last fifty years. The lack of regulation of costs associated with inpatient and outpatient visits is a political issue. In this thesis however, I will address a set of devices and the point of care methods that scientists and engineers can target to improve healthcare further by contributing to big data analytics as well as reducing costs in other areas. The healthcare industry in the United States is one of the most expensive in the world due to multiple facets. A few of these facets are due to the extreme costs associated with emergency room visits, invasive surgical procedures, and health monitoring methodologies. For example, costs associated with monitoring blood pressure at home vs monitoring at a doctor's office can save up to $1000 over a 10 year period[1]. A 2012 update by the International federation of health plans indicates an average cost discrepancy for inpatient and outpatient procedures between 2-4x more expensive than the next most expensive country, as shown in Figure 1 [2]. The two forms of care are in progress of becoming supplemented by more home-based health diagnostics with wearable electrocardiogram (ECG), electromyogram (EMG), blood pressure monitoring, and other monitoring techniques. To prevent more inpatient and outpatient visits the data collected

from the home health monitoring methods needs to be transmitted to a trained professional for analysis.

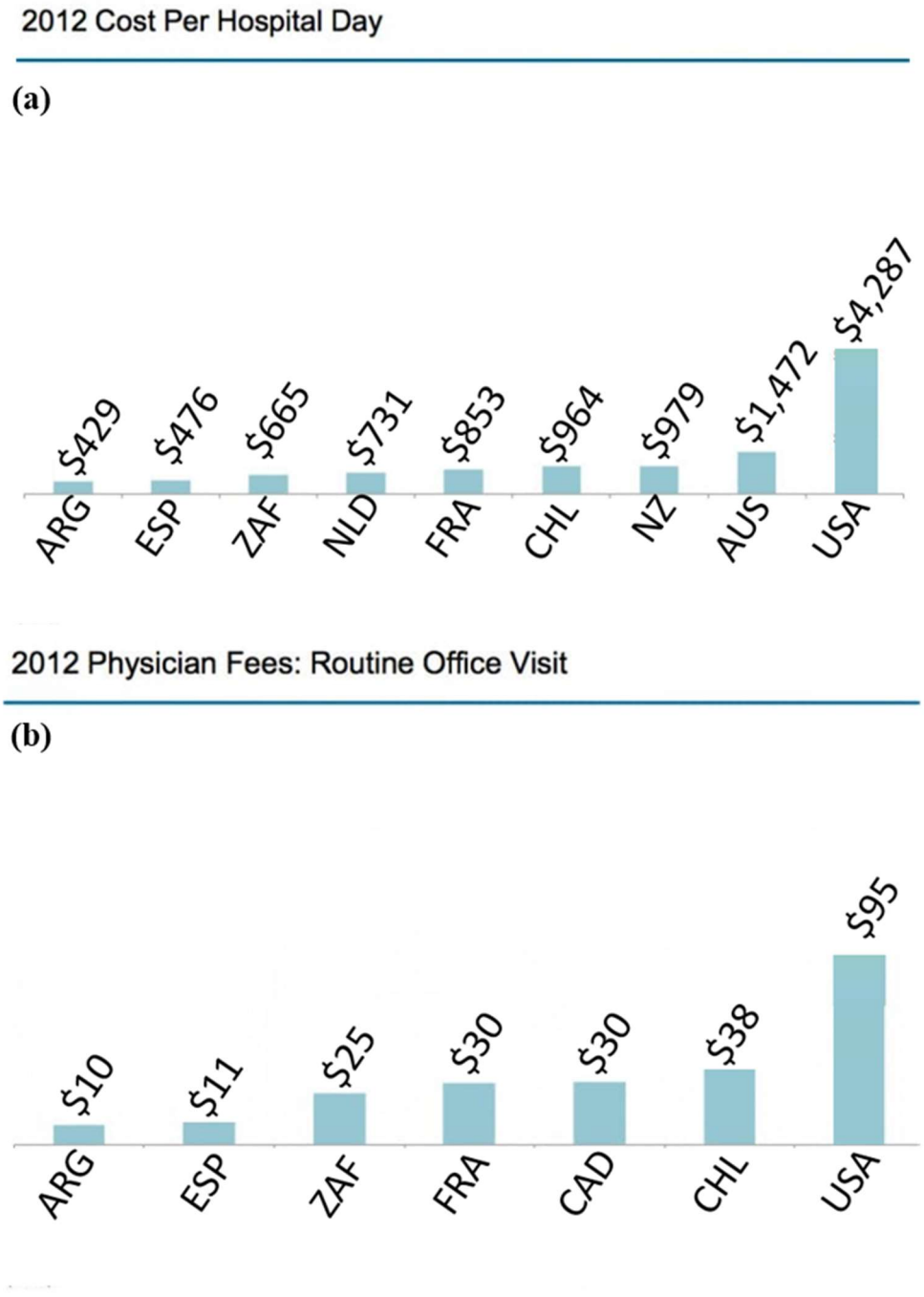

Figure 1. Cost of healthcare around the world data provided by International Federation of Health Plans. (a) Inpatient costs (b) Outpatient costs

Human health monitoring and interfacing has historically been limited to lab or medical procedures at an office but with the increasing use of smartphones and external antenna circuits the two can be integrated on the human body with IoT capabilities. This is enabled by the last few decades of enhancing, wireless communication, IC design, and classification systems. However, the backbone of this hardware is the fabrication and processing technology that enables it.

Utilizing all the facets of a wearable data acquisition system for human health monitoring requires a bottom up fabrication approach. (1) Designing the sensor mechanics and fabrication process is primary. (2) Design and implementation of the printed circuit board (PCB) (3) Testing the PCB for data acquisition. (4) Repeating steps 2 and 3 for on-skin analyses. (5) Analyzing the data for the health monitoring technique. (6) Develop an algorithm for classification of dataset.

Establishing the sensor mechanics is typically initiated on a computer aided design program such as AutoCAD, Solid works, or Rhino. After the model is created, it is uploaded into the appropriate Finite Element Analysis (FEA) software, ABAQUS, ANSYS or COMSOL. Each solver has its unique methodology, however for this thesis, ABAQUS is the appropriate solver used due to its capabilities in solving non-linear mechanics of elastomers and large displacements of materials.

A reliable fabrication process is necessary to form intricate patterns for the skin-electrodes that withstand the strain of skin. Two different fabrication techniques, subtractive and additive, are the printing methods investigated in this thesis to assess its feasibility for reliable skin electronics. Subtractive methods using photolithography are

grandfathered processes for producing micro and nanostructures in the semiconductor and packaging industry. A simple flow of photolithography is shown in Figure 2.

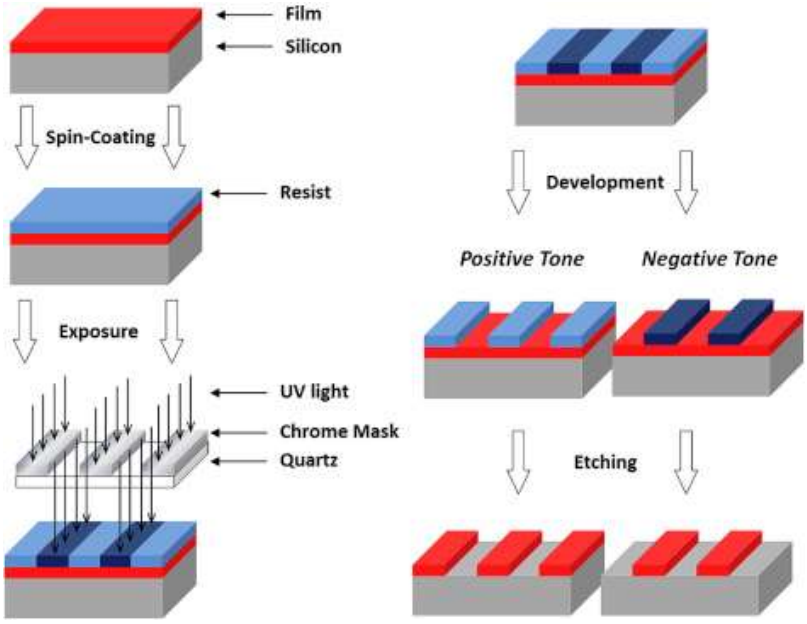

Figure 2. General photolithography process after film deposition [3].

Additive processes are recently developed methods of producing 2-D and 3-D structures in the sub-micron scale using tools such as the nanoscribe printer(Figure 3a), micron size using aerosol jet printing(Figure 3b), or millimeter size using fused deposition modelling 3D printers (Figure 3c). In this thesis I will discuss the use of photolithography and its limitations as compared to aerosol jet printed skin electronics.

A limited understanding of variants of patterning designs and process methods of skin electronics leaves a lack of knowledge of the conformality and recording capabilities of devices for experimentation. The design for human health monitoring devices is contingent upon the target area of recording. In this thesis I uncover the complexities of recording and classifying electrooculogram signals for eye movement and eye vergence. Conventional electrooculograms require sensors to be placed in multiple locations around

the face which are spaced too far apart to be packaged on the same interface as the board. Therefore, wires are needed to connect from the circuit board to the sensors. This complicates the device because the sensors need to connect to a single instrumentation amplifier and should be as close as possible to the amplifier. The improved hardware in this device will be discussed as it provides enhanced electrooculogram recordings along with the device and sensor positioning.

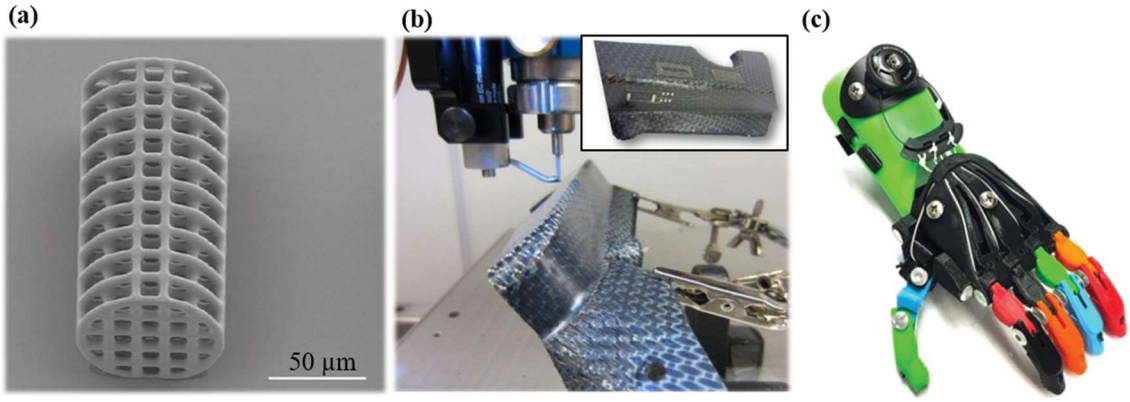

Figure 3. Additive Manufacturing techniques in sub-micron, micron, and millimeter resolution. (a) Two-photon polymerization based 3D printing using nanoscribe [4] (b) Aerosol Jet Printing on a carbon fiber 3D part [5]. (c) Fused deposition modelling 3D printing of a prosthesis [6].

After the recordings are collected, the data is sent to a software program for digital preprocessing and then post processing with a custom algorithm. The appropriate features and classifier for electrooculogram data is assessed and discussed in comparison to the classifiers used in the literature. A fast and accurate classifier is necessary for real-time control of machines, however for human health monitoring a slower classifier is acceptable as long as the output accuracies are precise. This thesis describes the lack of quantitative health monitoring of office therapies and how an all-inclusive system can advance home health monitoring and control.

1.2 Problem Statement and Objectives

Wearable electronics is a general umbrella term composed of fields of textile electronics, rigid wearable devices, and the most important one, soft electronics. In this thesis I will discuss the use of soft-electronics, which is gaining traction but lacks the mechanical stability for utilization in hospitals and clinics. Furthermore, there is a lack of a cost-effective fabrication technique to enable the use of soft-electronics in clinical settings. In order to implement more soft-electronic sensors and devices outside of research, the fabrication processes of the electronics are investigated towards targeted therapeutics and preemptive healthcare by investigating aerosol jet printing's feasibility. An optimized fabrication process could bring costs down but the ultimate cost reduction is due to the connectivity of devices.

Improved connectivity in the 21st century amongst multiple devices is made possible with the incorporation of Internet of Things (IoT). The enhanced network communication makes transmitting data from patients to doctors facile. The improvements are due to infrastructure enhancements in 3G, 4G, and fiber based broadband networks. Wi-Fi networks allow us to directly interface with the internet to upload and transmit data, similarly, Bluetooth Low Energy (BLE) transmits data locally from one device to another. Integrating BLE with other low power passive and active components allows for the use of small form factor batteries in data collection. Open-source platforms enable these efficient data transfer protocols over several meters. A few authors have even utilized these systems passively, but for this work it is not feasible to operate without a battery due to the sheer quantity and transfer rates of datasets.

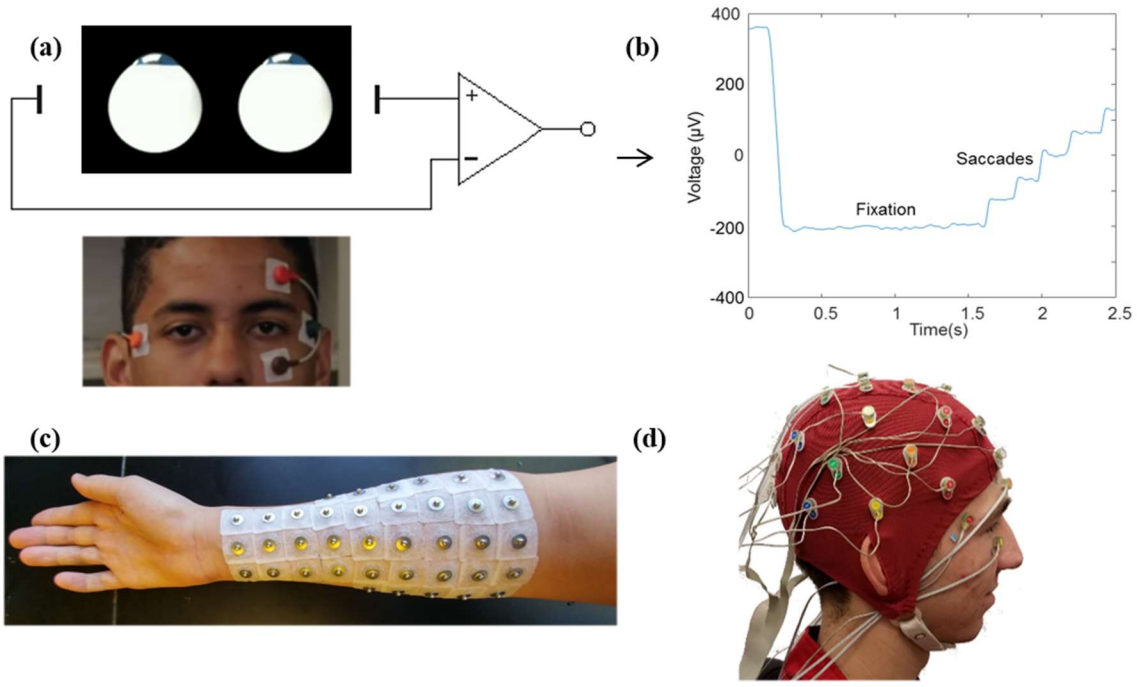

Figure 4. Biopotential recording techniques. (a) Conventional recording setup and (b) output EOG signal. (c) Electromyogram recording setup and (d) electroencephalogram setups are uncomfortable for long term wear.

The advancement of IoT capabilities and high fidelity integrated circuits simplifies biosensing methodologies. In this thesis I investigate the usage of electrooculograms (EOG) with skin electronics in the range of 5 μV to 1 mV (Figure 4a-b). Typically, a gel based electrode is obtrusively placed on the outer canthi of the head and above and below the left eye. Addition of more electrodes (Figure 4c) and a headcap (Figure 4d) makes these recording methods obtrusive and uncomfortable which prevents long term wear by patients. Bulky gel based sensors and data acquisition units are currently utilized for its robustness, but the long wires and uncomfortable placement does not enable it for long term wear. A few types of sensors exist, the gel based cup electrode is the oldest (Figure 5a), but more recently the hydrogel based electrodes are the gold standard (Figure 5b). In order to avoid the gel electrodes people started using higher resistance dry electrodes

(Figure 5c), but the most sensitive method is the needle electrode which penetrates the stratum corneum to hit the target site (Figure 5d). This thesis addresses the issues with utilizing such a system and why an alternative is necessary.

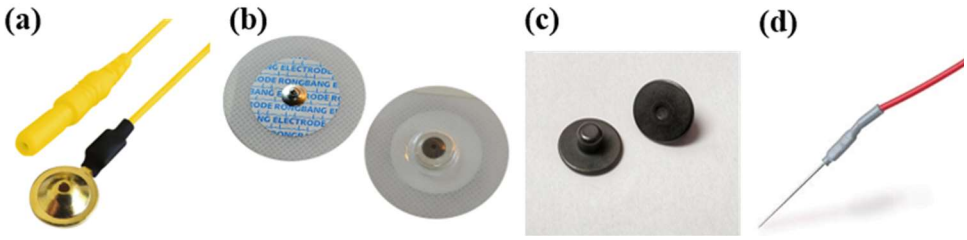

Figure 5. Sensor technologies. (a) Gold-cup based gel electrode (b) Hydrogel adhesive based Ag/AgCl electrode. (c) Dry electrode contact based Ag/AgCl electrode (d) Needle electrode which probes at the closest location to the targeted site.

Skin-electronics are best known for production using the subtractive conventional lithography process. However, with the enhancements in additive manufacturing it is possible to produce devices without waste and multi-step processing. Since conventional lithography requires depositing multiple layers prior to achieving the desired pattern, this makes additive manufacturing preferable. Very few publications depict the use of inkjet printing (IJP) in developing wearable devices as most strictly pertain to the printing characteristics of IJP. Consequently, aerosol jet printing publications for wearable devices are non-existent, which is why this thesis aims to shed understanding upon producing large array sensors at the maximum possible speed for large scale manufacturing.

The goal of this thesis is to develop a better additive manufacturing and subtractive processing for skin-electronics enabled by reliable mechanics modelling. An all-inclusive system requires an understanding of the mechanics of the circuits in its serpentine or fractal form. The patterns need to demonstrate conformality and comfortability to skin as well as

resilience to human motions. They need to be integrated into the sensors and devices for enhanced mechanics and resilience towards long term testing on a human subject. The device must provide high resolution recordings with as little electrical noise as possible and transmit this data wirelessly. After transmitting this data, it must be analyzed autonomously with the demonstration of an application to prove its functionality with the classification system. However all of this would not be possible without an in depth understanding of the fabrication processes comparing the advantages and disadvantages of microfabrication and aerosol jet printing.

1.3 Thesis Organization

This thesis is outlined in the following manner: Chapter 2 describes the literature with the current state of healthcare in the United States, research in skin-electronics, human-machine interfaces, electrooculograms, and printed electronics processing. Chapter 3 describes the improvements in human-machine-interfacing with electrooculograms using skin electronics and a case study. Chapter 4 describes the first human computer-interface with a VR stimulus for ocular therapeutics and recordings. Chapter 5 describes the materials characterization involved with AJP films, the processing parameters of AJP, and the sensor fabrication using AJP. Chapter 6 uncovers more applications and technology related to radio-frequency identification devices with AJP sensors. Finally, I conclude the thesis with future works and goals that should be set in order to innovate from my work.

LITERATURE REVIEW

This section will further breakdown the subdisciplines indicated in the introduction. A comparison of current medical devices that are available commercially and in research will be shown. The current state of mechanics of wearable electronics along with the materials integration and compatibility of processes will be discussed. This thesis will also emphasize the advantages and disadvantages of microfabrication technologies using subtractive and additive methods. Finally, to conclude state of the art review, various machine-learning classifiers and their advantages will be summarized. The use of all the previous information is incorporated with bio signal analyses for healthcare.

1.4 Disease Prevention and Therapeutics

Biosignals can improve quality of life for two diseases which impacts the United States with increased costs each year: (1) Motor Disabilities, (2) Convergence Insufficiency (CI)

A recent study shows that more than 10% of the US population has some type of motor disability [7]; 3.6 million people rely on wheelchairs and 6.7 million people have difficulty grasping low weight objects. For those with frail grip strength, an alternative wheelchair interface is needed, which can be helped by human-machine interfaces (HMI). Users that struggle with grip strength require the use of a smart wheelchair because of symptoms such as tremors, bradykinesia, and balance issues.

The next issue involves eye vergence conditions that can be destructive to a child's learning progress and an adult's day to day schedule. Convergence Insufficiency affects

about 6% of children less 19 years old in the US and 40% of adults and military personnel with mild traumatic brain injury[8-10]. Symptoms of CI can include headaches, blurred vision, fatigue, and attention loss[11]. These symptoms have been indicated to cost up to $1.2 billion dollars towards computer related visual complaints [11]. This thesis aims to implement novel technology to improve the quality of life of sufferers.

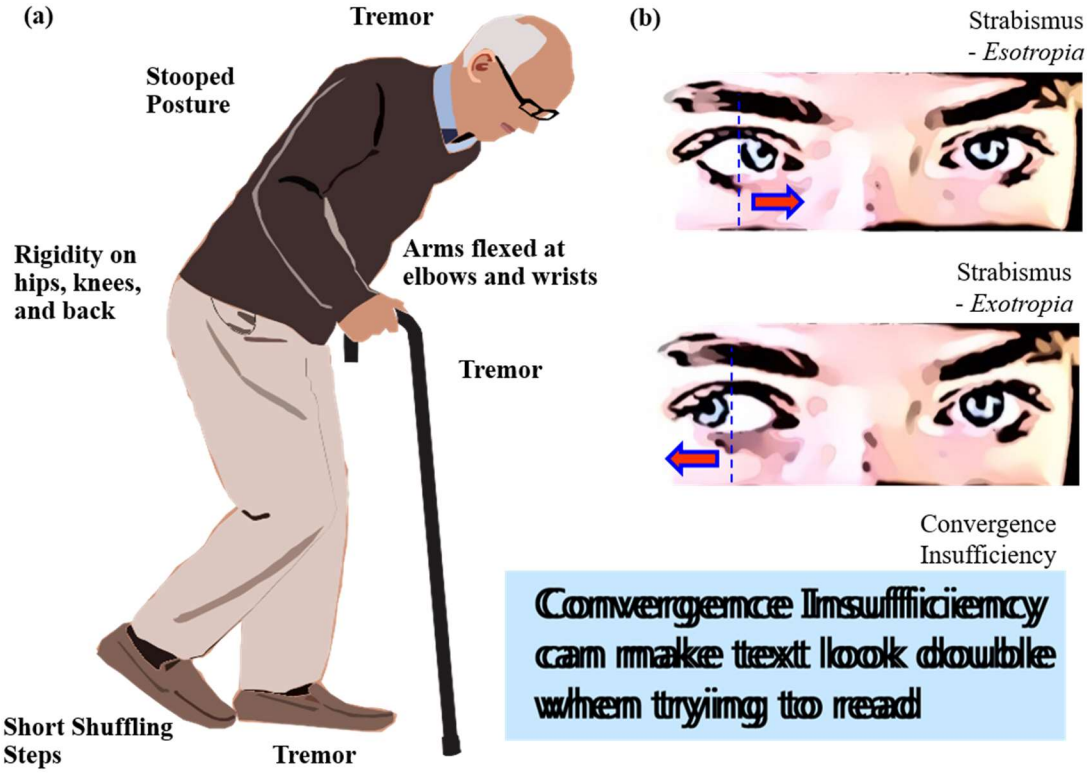

Figure 6. Prevalent health conditions in the United States which effects millions of people. (a) Neurodegenerative diseases such as Parkinson's disease results in loss of motor control due to rigidity as well long term tremors that limits the use of arms and legs. (b) Ocular disorders such as strabismus and vergence insufficiencies can cause learning disorders for children and loss of productivity for adults.

1.5 Biopotentials and Biomedical Instrumentation

Numerous biopotential outputs exist across the human body, ranging from lower potentials of the electroencephalogram to the higher potentials of the electrocardiogram. The potentials originate from the cellular level due to the concentration of Na^+ and K^+ ion as well as a little bit from Ca^+ ions [12]. The movement of these ions controls the voltage potential offset at that location. These ions are at a steady state potential when diffusion of the ions ceases from intracellular to extracellular locations at -70 mV. If a neuron activates the local region then the ions diffuse to the location of the action potential resulting in a change in potential. Electrodes observe these responses in varying amplitudes depending on the proximity of the electrode to the electrical signal.

This change in ions controlled by neuron based action potentials controls the response picked up by electrodes for electrocardiogram, electromyogram, and electroencephalogram (EEG) recordings. However, electrooculograms (EOG) is the focus of this thesis and it does not rely solely on neuronal changes to control the flow of ions, rather the potential difference between the retina and the lens develops moving potentials as the lens moves away or towards an electrode. This results in high variability of potentials from the number of activated rods and cones on the retina from incident light in different lighting conditions. EOG is easily contaminated by drift and DC polarization, but can be controlled with the right electronic hardware.

Appropriate hardware for recording and transmitting data is necessary for older and newer generation platforms. Electrodes are placed onto the skin as the sensor for recording biopotentials; wet electrodes consist of a gel base solution of NaCl ions within a cup

electrode or a hydrogel base, as show in Figure 5. Other types of electrodes includes dry contact without the need of a gel. However, the best electrode is an invasive needle electrode that is inserted into the organ for maximum potentials with little corruption from artifacts arising from the skin and other organs. In addition to the sensor, other components affect the recordings of biopotentials such as common mode rejection ratio (CMRR), input impedance, and resolution. These limitations of conventional devices require a customized hardware combination that is more compliant with the application. In this thesis, a comparison between non-invasive wet and dry electrodes is demonstrated with a conventional and customized data acquisition circuit for electrooculogram recordings and classification.

1.6 Human-Machine Interfaces

Multiple studies have demonstrated HMI applications [13-18] and activity tracking [19, 20] via non-invasive electrooculograms. EOG signals are derived from the potential that is created by the dipole of the eye from the positively charged lens and negatively charged retina. Typical amplitudes of signals range from 50 to 3500 μV and are caused by the amount light incident on the retina [17, 21]. The most important factor for successful HMI is to have high accuracy in signal classifications that are utilized for machine control. The end outcome of HMIs are similar to human-computer interfaces (HCIs) but the difference is that the output is relayed to actuation of a physical entity rather than a virtual one. Algorithms to enable multi-class differentiation use various features for maximized accuracy of subject-dependent signals. The continuous wavelet transform, Haar wavelet, is one of the most widely used features for EOG recognition [15, 16, 19, 20]. For example,

this feature was included in a classification method [22] for multiple task recognitions such as copy, read, write, video, browse, and null.

Figure 7. Example of human-machine interface controlling a drone with skin-electronics and human-computer interface controlling a game with skin-electronics on throat muscle.

A recent use of EOG [16] shows 90% accuracy of eye movements using both EOG and electroencephalograms for computer interfacing and 80% accuracy for manipulation of a robotic arm [23]. Nevertheless, the critical issue comes from the use of gels and sticky tapes, which cause skin irritation known as erythema. To address the issues, prior works introduced a "skin-like" electronic system, which offered a non-invasive, high quality recording of biopotentials on the skin [24-29].

1.7 Eye Vergence Monitoring and Therapeutics

Therapeutic techniques are in surplus for convergence insufficiency with the best overall method being office based visual therapy (OBVT). Typical convergence orthoptics requires a patient to visit an optometrist's office for 60 minutes a week for 12 weeks of procedural therapy targeting two ocular feedback methods, vergence and accommodation. The two therapeutic methods in conjunction, allow humans to converge on near point and far point objects. OBVT with pencil pushups for the home training procedure has shown

success rates as high as 73% but, home based vision therapy results in diminishing success rates of 33%[30].

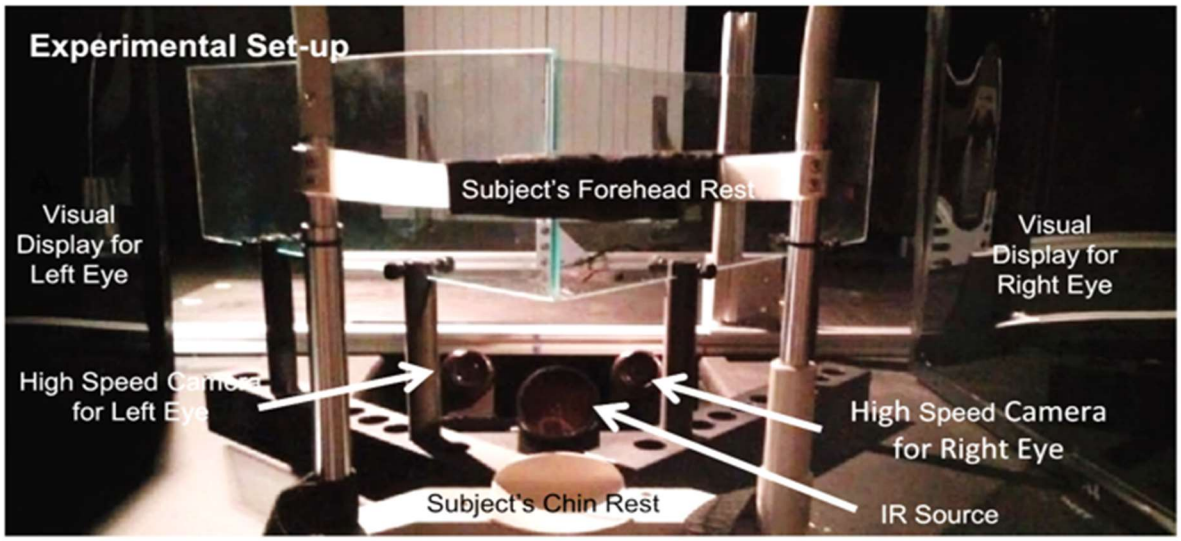

Figure 8. Eye vergence apparatus for measuring vergence insufficiency using videooculograms and stereo displays; "gold standard" for ocular measurements [31].

Thus, an alternative method is urgently required to reduce timely outpatient visits and ineffective home based visual therapy. Instilling a virtual reality (VR) therapy system with a smart appliance would be one of candidates that can provide an easy-to-use home therapeutics. Alternative stereo displays are common for vision therapy but a VR headset maintains binocular vision while disabling head motions for eye vergence precision. A new limitation is invoked from using the VR apparatus that interferes with the most common technique of measuring vergence motions, video-oculography (VOG) and electrooculography (EOG). VOG uses a high-speed camera that is stationary (Figure 8) or attached to a pair of goggles with a camera oriented towards the eye. Conventional EOG techniques utilize a set of Ag/AgCl electrodes, mounted on the skin, to non-invasively record eye potentials. VOG has received attention in disease diagnosis of Autism, Parkinson's disease, and multiple system atrophy due to miniaturization of electronics [32,

33]. A few studies demonstrate the capability of using VOG for CI assessments in vergence rehabilitation[34, 35] and testing of reading capabilities of children[36]. Unfortunately, VOG is still limited for a portable, home-based therapeutics due to the required immobility of a user, obtrusive system, and inaccessibility with a VR system[37].

1.8 Wearable Devices: Skin Electronics

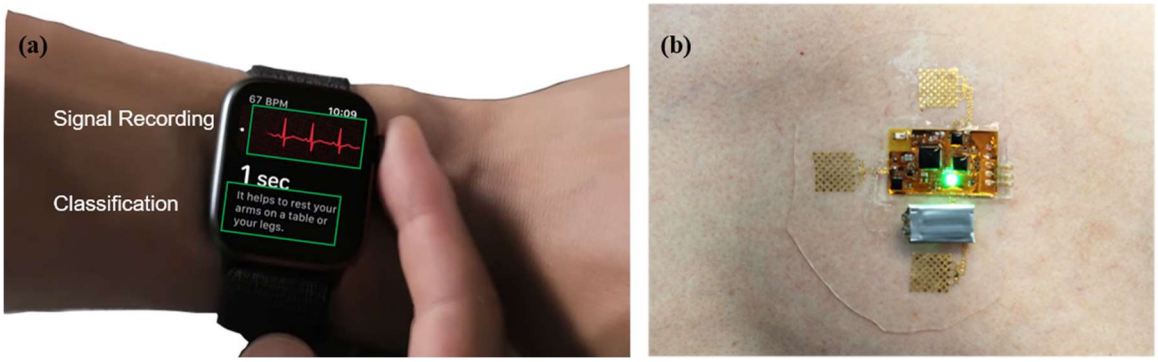

Figure 9. Robust and Rigid vs. Soft and Comfortable. (a) Apple watch on the wrist is one of the most sophisticated smart wearables able to classify atrial fibrillation. (b) Soft electronic wearable patch over the heart seamlessly integrates with the human body.

Wearable devices have conjured new fields of research over the last 10 years from energy harvesting to human health monitoring. These fields are consistently pushing the limits of materials processing and device efficiency into innovating applications. However wearable electronics can be separated into a rigid and robust category and soft, comfortable category. An example of rigid wearable platforms is the apple watch series 4 with its robust design that replaces traditional mechanical watches. Apple's smart watch is an FDA approved EKG sensor and classification platform for health monitoring (Figure 9a). This form of wearable monitoring system is revolutionary for 6.5 million individuals suffering from heart failure in 2017[38]. The alternative soft material electronics is solely observed in research geared towards various sensing platforms such as ECG right over the heart (Figure

9b). The comfortability of soft material devices enables long term compliance with the human skin. Since this thesis covers skin-electronics, most if not all the summarized devices will be soft material based electronics in the research.

Companies such as BrainCo, Neurosky, Delsys, and MC10 have perfected the rigid and robust platforms to collect data into their proprietary user interfaces by collecting EEG, EMG, and ECG signals. However, they are still devices that are not comfortable because they are not compliant to the human skin, with the exclusion of the MC10 device which utilizes meandered interconnects and boards with a rigid casing protecting the soft materials.

Asides MC10, meandered interconnects and sensors are limited to research due to limitations in the understanding of its mechanics after ICs are assembled onto it, resistance issues and long-term reliability of sensor platform. Many authors have developed microfabricated sensors to measure electrophysiology[24, 39-42] similar to gel electrodes, but some authors have also used conventional strain sensors to measure respiration on the diaphragm[43]. The innovations of printed electronics and nanoparticle synthesis has revolutionized the ability to develop prototype circuits and sensors. Metals such as, gold, copper, and silver can be printed easily but each requires careful post processing. On the other hand, polymers and ceramics can also be printed but may be difficult for long term processing. Inkjet printing has paved the way in skin-electronics[44, 45] for a newer printing technique, aerosol jet printing, which has not seen much advancement in large array sensor or circuit printing got wearable devices. This thesis seeks to mitigate disconnection between wearable skin sensors and aerosol jet printing.

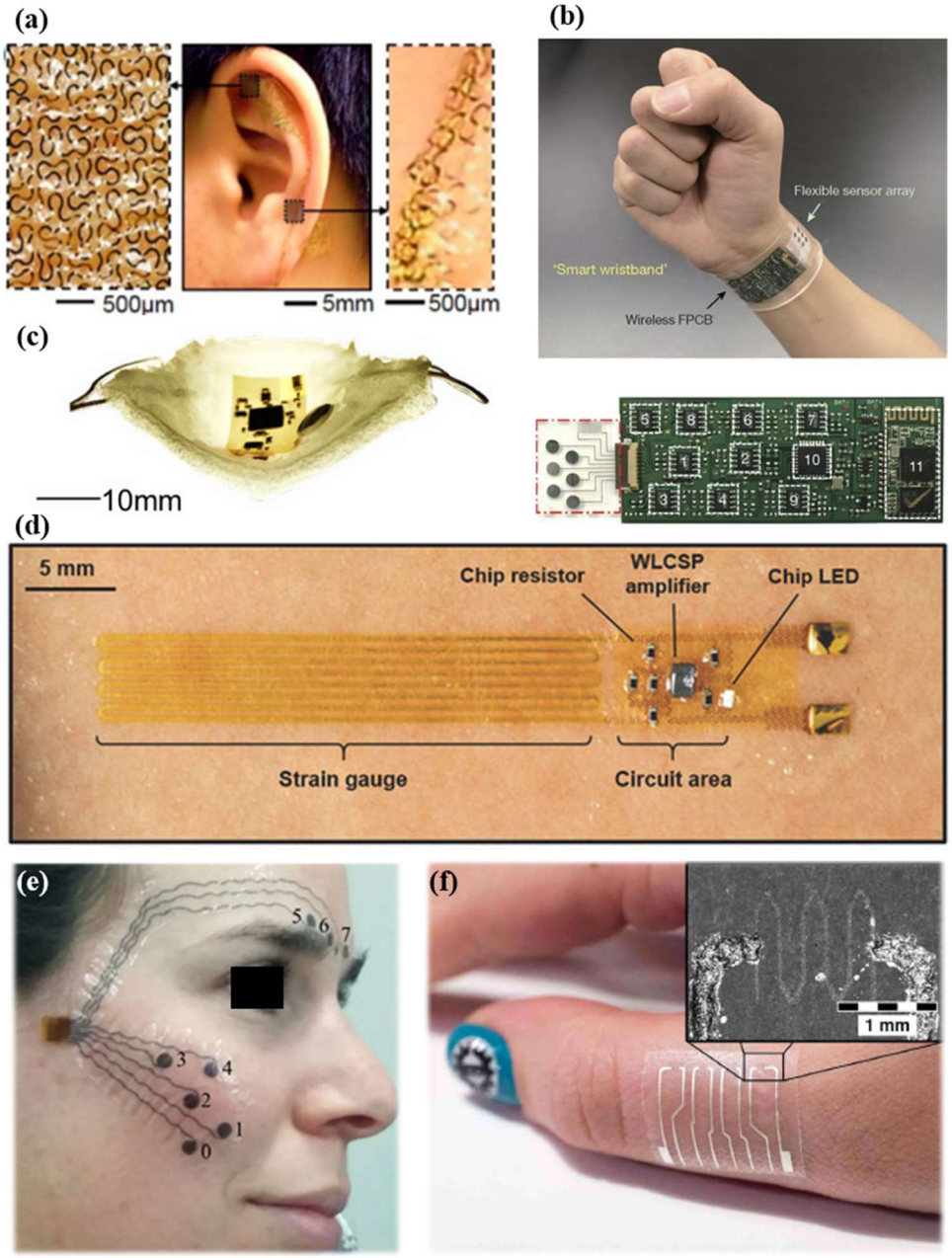

Figure 10. Flexible, stretchable circuitry and sensor arrays developed for human health monitoring with elastomers on skin. (a) EEG electrode for temporal lobe measurements [42] (b) Smart wrist band to monitor ionic sweat analytes using potentiometric sensors [46]. (c) Intraoral retainer with a flexible and stretchable circuit placed on an elastomer for measuring sodium analytes [47]. (d) Strain sensor used to measure respiration from the displacement of the diaphragm [43]. (e) Inkjet-printed electrodes for EMG recordings of facial gestures using PEDOT and silver[45]. (f) Graphene/PEDOT:PSS temperature sensor array printed using inkjet[44].

1.9 Fabrication Methods

In this section I will provide some insight into fabrication processes that have been used for developing wearable electronics consisting of two different umbrella terms: Subtractive and Additive. Fabrication processes involving inkjet and aerosol jet printing are additive processes, but photolithography and some screen printing process are subtractive. Both methods produce devices with different material characteristics from crystallinity to substrate compatibility.

1.9.1 Photolithography and microfabrication

Microfabrication and photolithography methods has existed for almost 50+ years in creating microstructures. This method involves a series of stringent processes of cleaning, metallization, oxidation, spin casting, light exposure, and etching and developing. The numerous processing steps contribute to the likelihood of contamination and device failure rates. However, a successful fabrication result would be the completion of a device capable of sensing, stimulating, or communicating signals.

Common procedures for soft electronic fabrication involves cleaning a silicon wafer and spin coating several layers of polymers including a sacrificial polymer. Afterwards, either e-beam evaporation or sputtering deposition is used for low temperature deposition. A layer of positive or negative photoresist is spin cast and then exposed with 375 nm ultraviolet (UV) light with a chrome photomask. Afterwards the metal is etched away resulting in metal ion waste while the patterns on the substrate remain. The photoresist is cleaned off and the process continues or is completed and ready for the transfer process.

Microfabrication and photolithography is a robust processing method that results in materials waste or reprocessing. This can be bad for the environment[48] as well as costly[49]. It can also be rather time consuming due to the repetitive adding and subtracting of materials. More recently the detrimental impacts of individuals in the semiconductor industry is apparent in their offspring[50]. Alternative additive methods are also preferable because it avoids the costs to the environment and businesses. Many additive manufacturing technologies exist, but to replace photolithography each system has to be compared for its individual strengths constituted by speed, resolution, and print reliability.

1.9.2 Screen printing

Screen printing is a common printing technique for electronics since before the 1970s[51]. It is a cheap technique for printing circuit boards and it has been more recently applied towards flexible sensors that do not require a high resolution print[52]. To print the pattern, a squeegee forces ink through a silkscreen producing the targeted patterns on the substrate. This is like dispensing solder onto a PCB using a stencil for solder reflow process with lead free solder paste. Screen printing may be cheap but it cannot achieve the desired resolution of the next two techniques due to a maximum resolution of 7 mils or ~175 micron[51].

1.9.3 Inkjet printing

Inkjet printing on the other hand is also an additive printing method but instead of utilizing a physical stencil, a computer program translates a digital CAD model into precise motions on a set of stepper motors attached to a print head. This print head moves around a heated platen to deposit droplets onto a substrate. Typical inkjet printers use piezo drive but can also be controlled by a thermal bubble, but both methods use displacement to force the

droplet out. A relatively newer method is the electrohydrodynamic IJP where a large electric field difference between the substrate and the print head pushes the ink onto the substrate. The largest issue with all these techniques is the formulation of the ink which requires the viscosity, particle loading, and surface tension to be low[53]. A general summary of inkjet vs aerosol jet printing is shown in Figure 11.

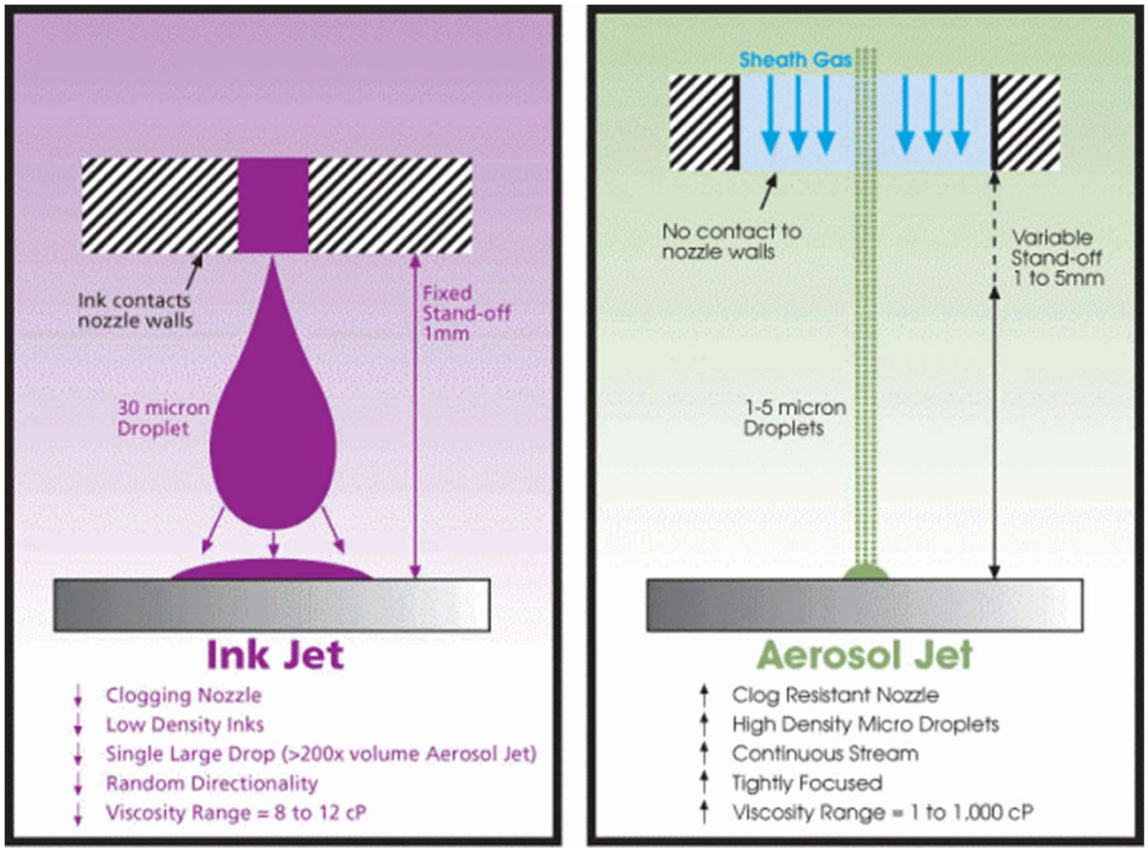

Figure 11. General drawbacks and advantages of inkjet and aerosol jet printing.

1.9.4 Aerosol jet printing

Aerosol jet printing (AJP) involves the usage of multiple mass flow controllers channeling nitrogen gas into either (1) Ultrasonic or (2) Pneumatic atomizer. The involvement of this inert gas enables the transportation of aerosolized inks from the atomizer container to the deposition head without modifying the inks properties. The Ultrasonic atomizer (UA) relies on excitation from a piezoelectric transducer which transfers the ultrasonic energy via water bath medium which has a controllable temperature setting from 0 – 50 °C. The UA is reliable in atomizing inks up to 5 cPs in viscosity but other inks can have its viscosity reduced by increasing its temperature.

The alternative, Pneumatic atomizer (PA) is the main appeal for the AJP because it can atomize inks up to 1000 cPs. This makes the PA more appealing from the entrenched inkjet printer. In order to atomize such high viscosities the PA relies on high velocity flow rates that pushes nitrogen down a stem out of a diffuser. At the same time the ink is sucked up through the same diffuser hole. This type of atomization creates large and small agglomerates of the ink that are filtered through a virtual impactor and a HEPA filter. The remaining smaller agglomerates pass through the deposition head onto the substrate same as the UA.

Numerous challenges exist with direct printing that also exists in other fabrication techniques. Most polymers consist of very low surface energy which requires precise tailoring of the surface tension of the ink that is deposited on a polymer. Other materials such as metal surfaces have relatively high surface energy which may not be a significant hindrance to ink deposition. Therefore the inks have to be tailored to wet the surface with either a low surface tension ink or a high energy substrate. This prevents disconnections in printed patterns.

AJP requires the control of many variables for long term deposition processes with high throughput. Majority of researchers are working on devices in the microscale for antennas[54], strain sensors[55], and biological samples[56] that do not require rapid deposition rates and platen velocities. In this thesis I will address AJP with inks from lower (0.5 mm/s) to higher platen speeds (10 mm/s). A materials characterization study of AJP inks after sintering is also investigated for its electrical conductivity and mechanical elastic modulus. Current applications of these inks are shown along with a brief discussion of future applications.

ELECTROOCULOGRAMS FOR HUMAN-MACHINE INTERFACE

In this EOG work we focus on soft bioelectronics and wireless wheelchair interface (Figure 12). This ergonomic HMI system incorporates conformal biosensors and a Bluetooth unit interfacing the bioelectrode with a robotic wheelchair. The “skin-like” bioelectrode enables a high-fidelity recording of EOG, supported by the direct comparison with conventional rigid electrodes. This soft bioelectronic system demonstrates mechanical compliance in both stretchability (30%) and bendability (up to 180°). A newly designed classification algorithm with an optimized set of features shows the accuracy of 94% with five different eye movements, which is used to demonstrate a hands-free control of a robotic wheelchair via EOG.

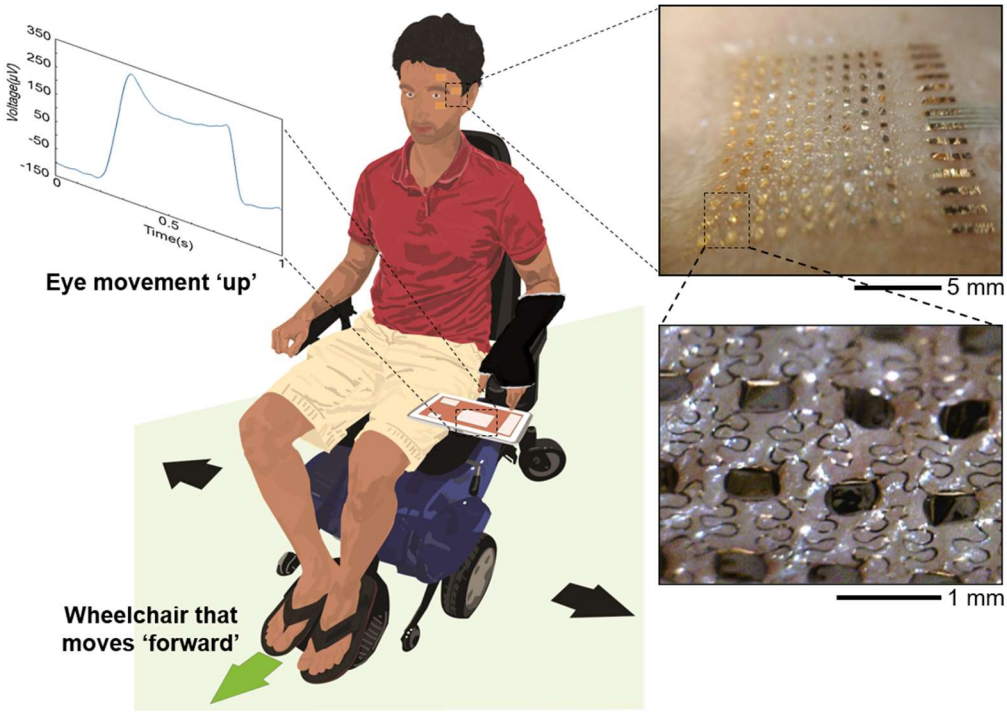

Figure 12. Overall integration of HMI with electrooculograms and skin-electrodes

3.1 Methods for Electrooculogram – HMI

1.9.5 Finite element analysis

Three-dimensional finite element analysis using a software (ABAQUS, Dassault Systems, Waltham, MA) was conducted to investigate mechanical behaviors of an electrode upon skin deformations: bending and stretching [57, 58]. The soft electrode used in EOG measurement was composed of three layers including 300 nm-thick Au, 1 μm-thick polyimide (PI; HD MicroSystems, Parlin, NJ), and 5 μm-thick silicone elastomer. Young's modulus (E) and Poisson ratio (v) of materials used in the modeling are $E_{silicone}$ = 69 kPa [28] and $v_{silicone}$ = 0.49 [59] for a silicone elastomer; E_{Au} = 78 GPa and v_{Au} = 0.44 for Au [59]; E_{PI} = 2.5 GPa and v_{PI} = 0.34 for polyimide [59]. The maximum principal strain on Au was mainly investigated to determine the mechanical stability upon multi-modal

deformations. Note that Au membrane was used as an electrode, PI was a supporting layer to hold the membrane, and silicone elastomer was a substrate to mount the electrode for handling the sensor.

1.9.6 Fabrication of a soft bioelectrode

Fabrication of a soft electrode was based on the combination of a conventional photolithography (Figure 13) with material transfer printing (Figure 14). A glass slide (Ted Pella, Redding, CA) was prepared by a cleaning process using acetone, IPA, and rinse with DI water. Afterwards, a primer (MicroChem Corp., Westborough, MA) was coated on the substrate for enhanced adhesion. Multi-layer coating and curing of PMMA and PI was followed. The electrode patterning started with Au deposition on the PI and photolithography defined patterns. A second layer of PI was encapsulated while exposing the skin contacted patterns and wire connection pads.

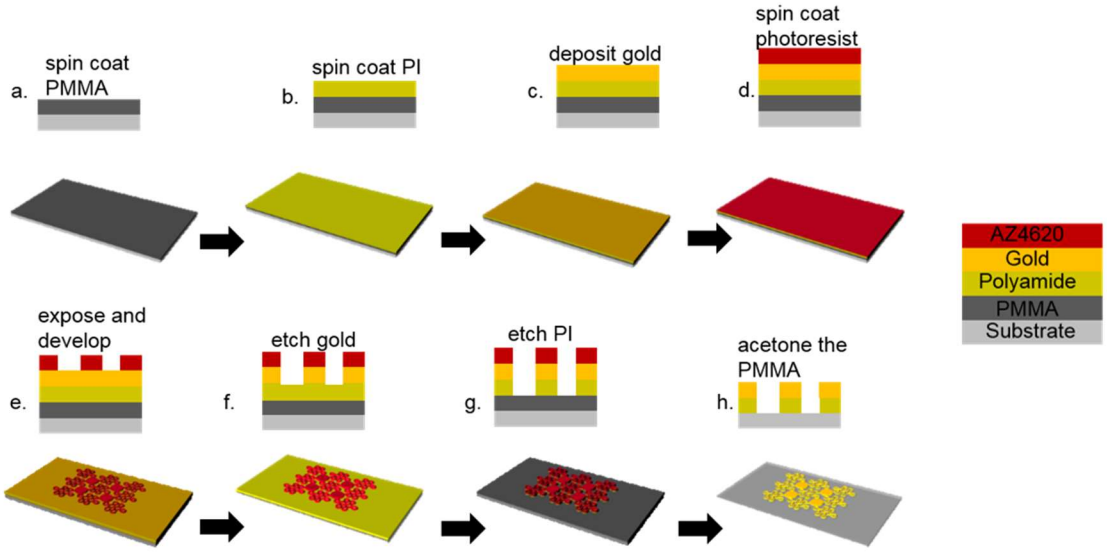

Figure 13. Fabrication process. (a) A clean glass side is prepped and PMMA is spin coated. (b) Polyamide is spin coated. (c) Gold is deposited. (d) Photoresist is spin coated.

(e) Photoresist is exposed and developed. (f) Gold and chrome is etched. (g) PI is etched. (h) PMMA is dissolved and the electrode is transferred to another elastomer.

The electrode was retrieved by a water soluble tape after dissolving the sacrificial PMMA in solvent. Afterwards, it was transfer printed on an ultrathin elastomeric membrane (5 μm in thickness) on a polyvinyl alcohol film. Lastly, a flexible film was attached onto contact pads for connection with a wireless system (BioRadio; Great Lakes NeuroTechnologies, Cleveland, OH).

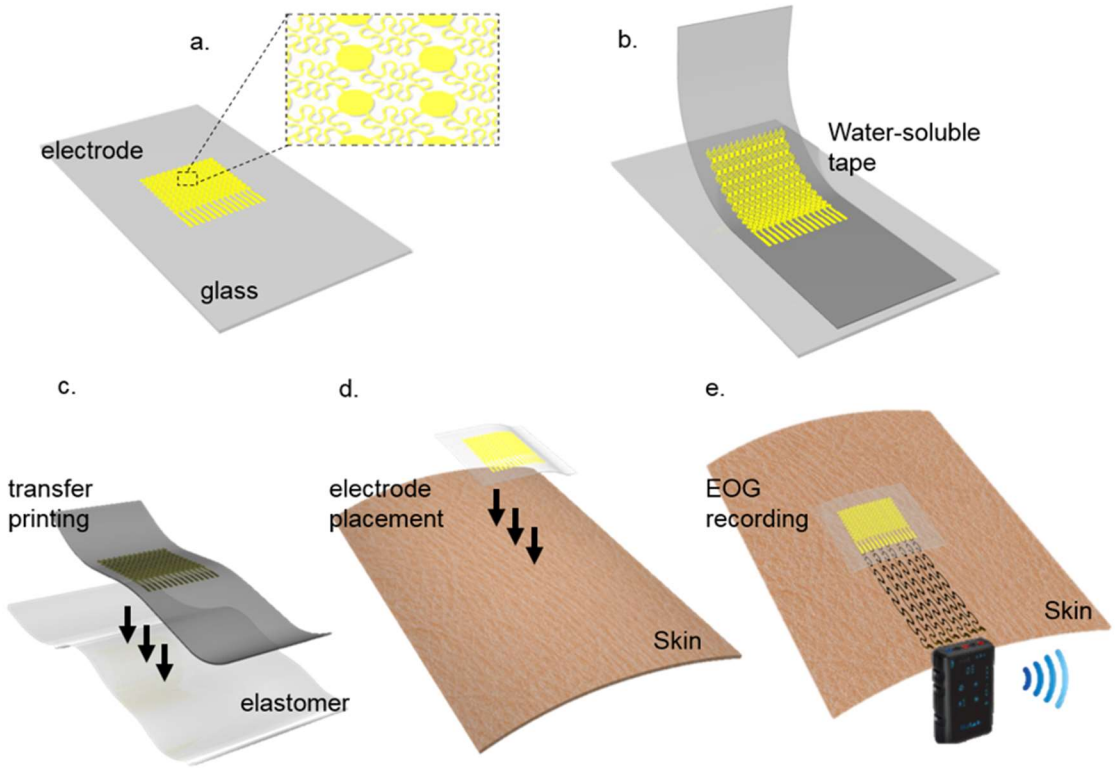

Figure 14. Transfer process. (a) Electrode on glass slide is ready for transfer. (b) Water-soluble tape is attached to the electrode and peeled off. (c) The peeled electrode is transferred to a thin stretchable elastomer as a substrate and the water-soluble tape is dissolved. (d) A flexible connector is hot pressed onto the electrode contact pads, which is then transferred onto the skin for measurements. (e) EOG recordings are wirelessly transferred via Bluetooth communication onto a laptop for observations.

1.9.7 Measurement of mechanical behavior

Biaxial stretching of the fabricated electrode was conducted on a programmable stretcher (Figure 15). The stretcher held a sample with four clamps. Precise control of the travel distance by an Arduino and stepper motors determined the applied strains. Ultrathin copper wires (100 μm in diameter) were connected to the electrode for recording of resistance change by a digital multi-meter (Model 2100, Keithley, Cleveland, OH). In a bending test, a sample was placed on a flexible plastic film, which allowed bending from 0 to 180° with the radius of curvature of 500 μm. Similar to the stretching test, electrical resistance was monitored according to the degree of bending. We utilized a portable microscope (Dino-Lite, Torrance, CA) to inspect any localized, microscale fracture.

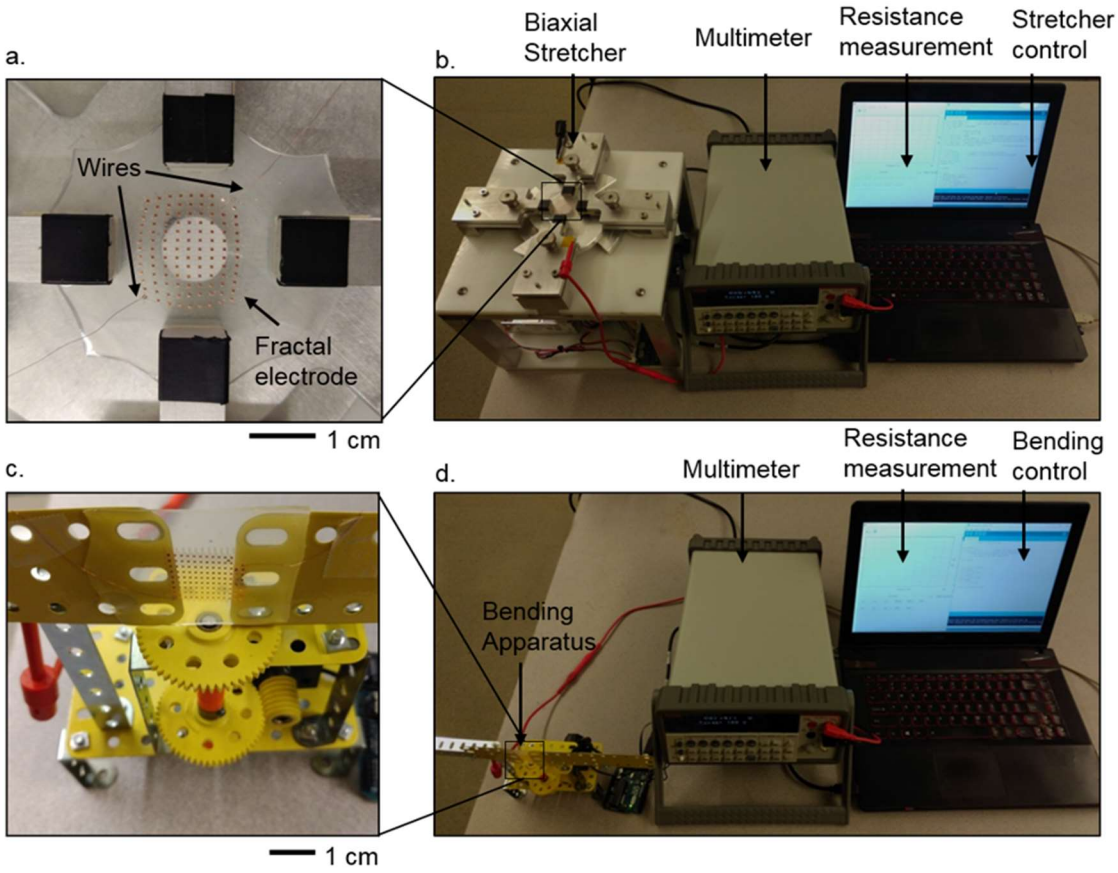

Figure 15. Mechanical stretcher and bending apparatus (a) Photo of an automated mechanical stretcher (top view) with four screw clamps that fix the sample to the stretcher with wire attachment for electrical resistance measurements. (b) The biaxial stretcher (left), multimeter (middle), and data acquisition laptop (right) is used to control the stretcher with a microcontroller and acquire resistance measurements with the multimeter. (c) Photo of bending apparatus at the 0 degree position with the sample attached by its own adhesive properties. (d) The bending apparatus is configured to a stepper motor controlled by the microcontroller. A multimeter acquires resistance measurements of the sample.

1.9.8 In vivo measurement of EOG

Three healthy males, aged from 20 to 25, participated in EOG measurement based on the approved protocol (HM20001454) at Virginia Commonwealth University. All subjects with 20/20 vision were given an explanation for the study and signed a consent form. For EOG recording, two sets of electrodes were placed on the skin around the eyes. For horizontal eye movements, each electrode was positioned 1 cm away from the outer

canthus of each eye. For vertical eye movement, left eye was selected; one was mounted 1 cm away from the eyebrow and the other was positioned 1 cm away from lower eyelid. A common ground was positioned on the forehead.

1.9.9 Data acquisition

Fractal bioelectrodes were configured to work with a commercial wireless unit. A two channel setup was configured with a sampling rate of 500 Hz. We made a quantitative signal comparison between commercial Ag/AgCl electrodes (MVAP II, Newbury Park, CA) and fractal electrodes. The measured EOG signals were wirelessly transmitted to a receiver connected to a laptop or tablet interface with a data acquisition interface.

1.9.10 Human-wheelchair interface

A subject was given auditory commands to start training by following the direction of the customized interface. A total of 40 trials were obtained for four classes (up, down, left, and right). Afterwards, each user tested the accuracy of trained data. Again, auditory commands were given to initiate the classification. Twenty commands for five classes were provided in the classification interface. Users repeated this process three times for conventional and fractal electrodes. The overall accuracy was acquired from the sum of all three trials.

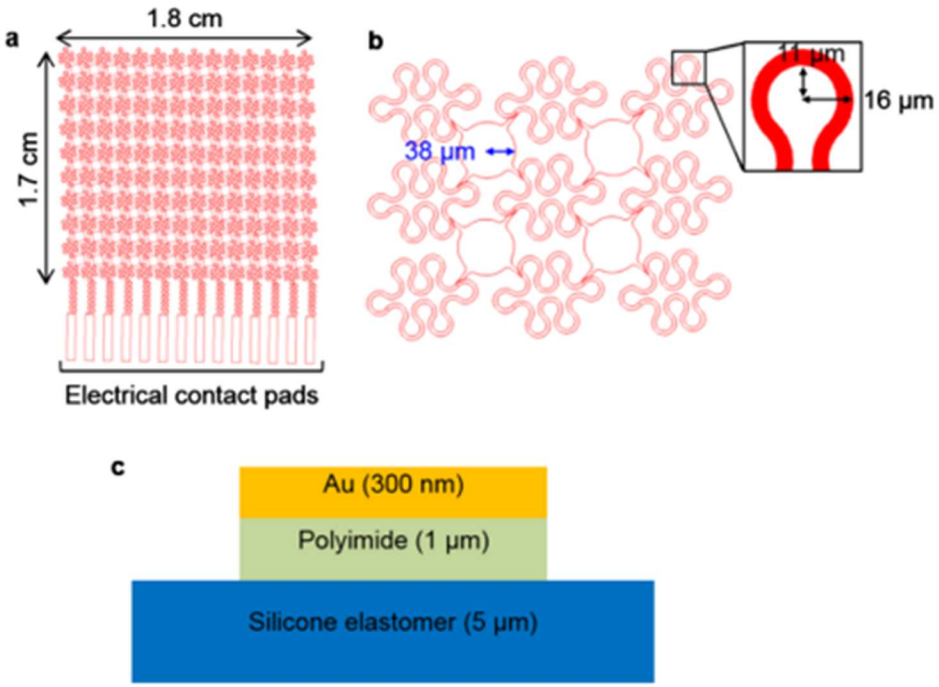

Figure 16. The design and structure for a "skin-like", fractal electrode. (a) Dimension of a skin-like electrode. (b) Close-up view of the electrode including circular cells (radius = 500 µm) and fractal interconnects (width = 50 µm). (c) Layer composition of the electrode.

1.9.11 Design and characterization of a soft electrode

Skin-wearable, soft electrodes were designed to have mechanical stretchability for intimate contact to the dimpled skin and avoiding any failure caused by dynamic skin deformations. Finite element analysis (FEA) played a key role to design a highly deformable structure. We explored a self-similar, open-mesh structured 'fractal' patterns (Figure 13) [40, 60]. We used an array of circular disks, interconnected by the fractals, which offered an improved areal coverage for an enhanced signal-to-noise ratio. The FEA result in Figure 14a and Figure 14c captures the stretching behavior of the electrode upon tensile strains and bending; the fractal interconnects in the design absorb the applied stress to isolate it from the disks. The maximum principal strain, applied to Au, is less than 2%

under the biaxial strain (30%) (Figure 14a), which is well under the fracture strain (5%). A microscopic observation and quantitative mechanical test follows to validate the mechanics analysis (Figure 14b and Figure 14d). A microscopic investigation monitors visual defects on the structure, caused by mechanical fracture during cyclic stretching (Figure 14b) and bending (Figure 14d). Two-point resistance measurement upon repetitive loading and unloading quantifies the structural safety since any abrupt spike in the plot captures unexpected fracture. A cyclic mechanical test includes an increment of 5% tensile strains and 10° folding for the stretching and bending test, respectively. In this mechanical study, we apply additional safety factors by considering a maximum strain upto 30% and bending upto 180° (with 500 μm of radius of curvature), which still shows negligible resistance change on the electrode (Figure 14e and 14f). Note that normal human external tissues stretch upto ~20% without tissue damage [28] and typical skin deformation does not exceed the selected bending curvature [40]. Overall, the FEA and experimental results ensure that the fractal structure makes a suitable electrode even if a user has unusually developed dimples and habits to create exaggerated facial expressions [61].

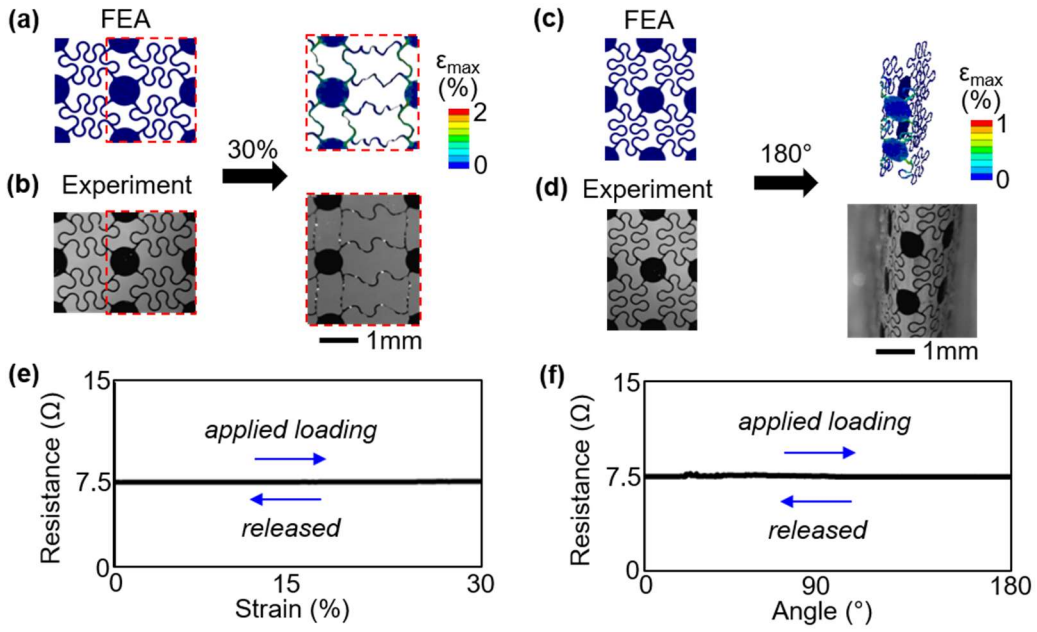

Figure 17. Computational modeling and experimental validation of a fractal structured electrode upon mechanical deformation. (a, b, c, d) Comparison between the finite element analysis (FEA) results and experimental observations with (a, b) biaxial tensile strains upto 30% and (c, d) bending upto 180 degrees with the radius of curvature (R) of 500 μm. (e, f) Quantification of electrical resistance according to the (e) applied strains and (f) bending; (e) cyclic mechanical test with repetition of loading and unloading and (f) cyclic mechanical bending test. The scale bars in the FEA data indicate the maximum principal strain applied on the electrode.

1.10 Measurement of EOG Signals

A set of the fractal-structured electrodes was used to record target EOG signals on the skin. For a long-term, persistent HMI demonstration, we conducted electrophysiological measurement, without the use of any conductive gels and acrylic adhesives. The fractal electrode measured four kinds of EOG signals from different eye movements involving up, down, left, and right (Figure. 18a). The same experimental procedure was applied for both conventional and fractal electrodes for side-to-side comparison. The EOG data recorded by skin mounted electrodes were wirelessly transmitted to a data acquisition unit for signal processing. Raw EOG signals in Fig. 15a, measured by vertically mounted electrodes,

compare ‘up’ and ‘down’ movements. Both conventional and fractal settings show very similar signal amplitudes along with the baseline noise. Horizontal electrodes (Figure 18b) capture higher EOG signals (600 - 750 µV) than the vertical motions (~400 µV) where the signal strength is dependent on the amount of angle change of the eyes. The direct signal comparison via derivative filtering (Figure 18c and 18d) makes clearly distinguishable features of target signals. This filtering step decides the correct threshold for data processing in a classification algorithm. In the given data, threshold values can be chosen in the range of 3 - 5 µV/s, dependent on a user’s training data.

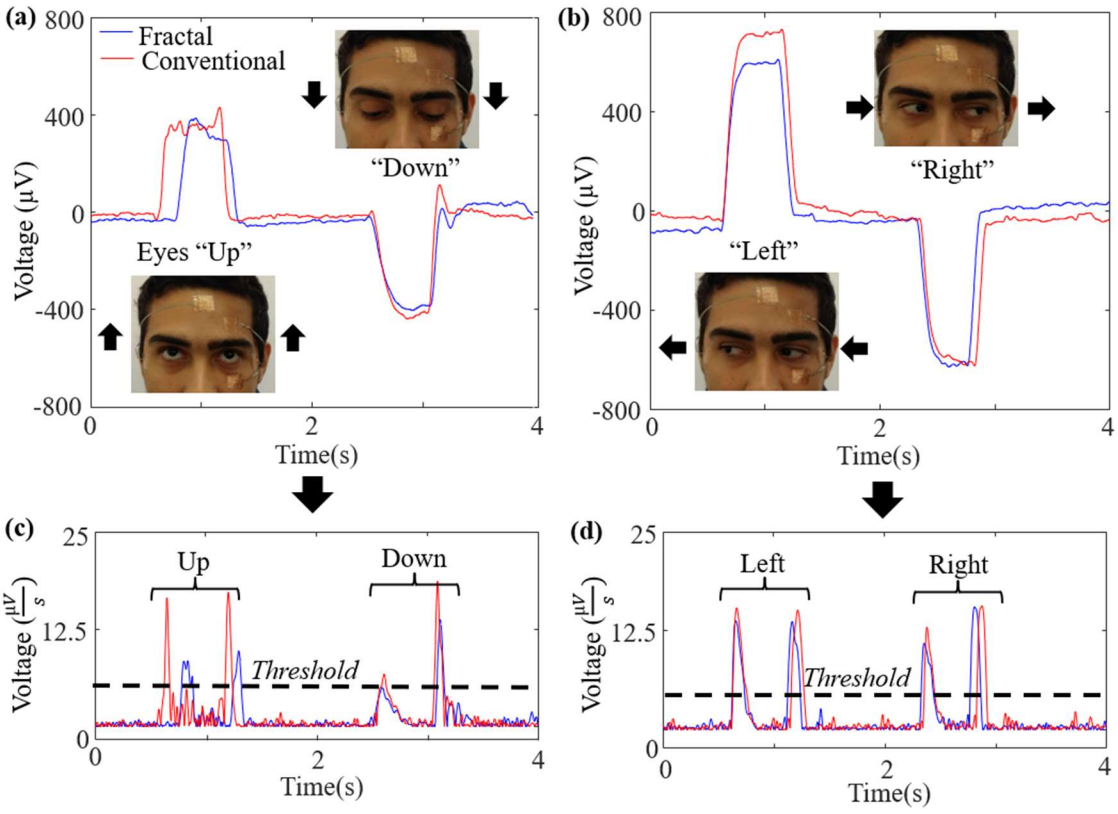

Figure 18. A representative set of EOG signals involving four kinds of eye movements. (a–d) Direct comparison of raw EOG signals measured from fractal and conventional gel electrodes: signals from (a) eyes ‘up’ and ‘down’ motions and (b) ‘left’ and ‘right’

motions. Bandpass (0.1–20 Hz) filtered EOG signals from (c) ‘up’ and ‘down’ motions and (d) ‘left’ and ‘right’ motions.

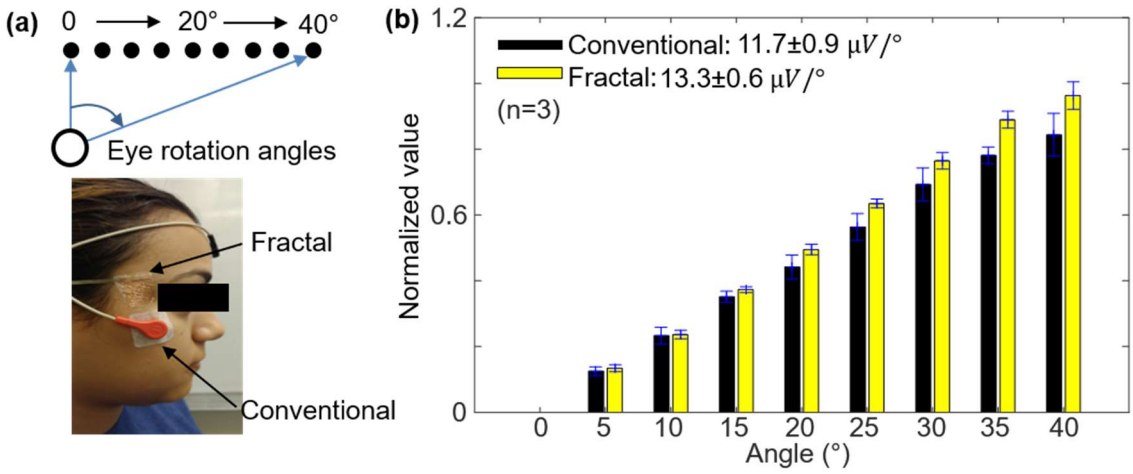

Figure 19. Comparison of electrode sensitivity. (a) An experimental setup targeting a series of circles to measure the angle-dependent EOG sensitivity. (b) Normalized EOG signal amplitudes according to the angle change of an eye where black and yellow bars represent conventional and fractal electrode, respectively. Error bars show the standard deviation (n=3).

Changes of EOG amplitudes according to eye rotation angles (Figure 19a and 19b) quantify the sensitivity of two types of electrodes (fractal and conventional). A test subject wears two differential electrodes, positioned 1 cm away from the outer canthus of each eye for concurrent comparison (Figure 19a). The sensitivity measurement asks the subject to trace a series of circular targets (diameter = 1 cm), located 60 cm away from the eyes. Each target corresponds to 5 degree changes of eye rotation. Filtered EOG signals in Figure 19b presents amplitude variations according to eye motions from 0 to 40°. The calculated resolutions are 13.3±0.6 and 11.7±0.9 μV/° for fractal and conventional electrode, respectively. The higher sensitivity from the fractals is explained by considering the signal-to-noise (SNR) related to the skin contact area. The skin-like electrode covers ~3.1 cm^2 to maximize the available area on the skin, while the rigid electrode (MVAP II, Newbury

Park, CA) including a gel occupies only ~0.8 cm^2, limited by the required adhesive pad to affix on the skin. The direct contribution of the contact area to the signal strength is measured by changing the size of fractals, while the rigid electrode stays intact (Figure 20a – 20b). A user wearing both horizontal electrodes focuses on three target locations corresponding to -40, 0, and +40° in the horizontal direction. The result shows that SNR values decrease as the size of fractals shrinks from full to half and quarter (Figure 21c; averaged values based on 8 trials); the quarter-sized electrode (contact area: 0.78 cm^2) shows comparable SNR values to the rigid one. A slight DC baseline drift in Figure 20a and 20b would come from the low frequency signals with respect to skin potential changes[18].

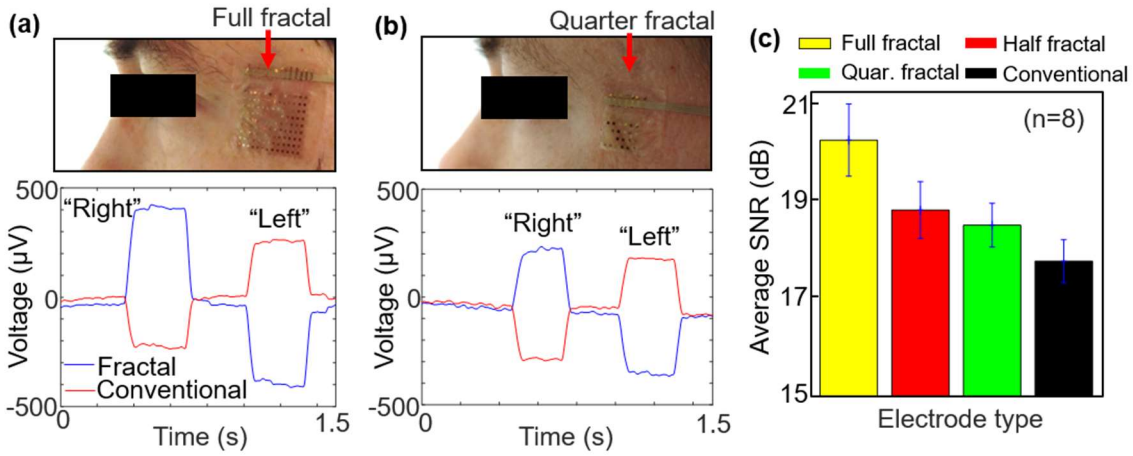

Figure 20. Comparison of electrode sensitivity. (a-b) Photos of fractal electrodes mounted on the skin (conventional electrode is located on the contralateral site) and the corresponding EOG signals comparing the signal strength between fractal and conventional electrodes. The signal strength is dependent of the electrode size; (a) full size and (b) quarter size electrode. (c) Averaged SNR values comparing the size effect of fractal electrodes with a fixed rigid electrode (error bars from n=8 with the standard deviation).

Skin assessments by infrared thermography and contact microscopic observation (Figures 21a – 21b) capture the advantage of the fractal bioelectrode over the gel-covered rigid electrode. Electrolyte gels on the metal electrode causes an adverse effect (erythema)

on the skin by increasing the localized temperature (Figure 21b; 5 hours of skin contact), while the fractal electrode shows a negligible effect even with lamination over 10 hours (Figure 21b). In addition, an adhesive pad, used to mount the rigid electrode, exfoliates the epidermis, which causes pains and skin rashes (Figure 21c). Collectively, the comparative assessments demonstrate the novelty of the soft biosensor for a comfortable, long-term usable human-machine interface.

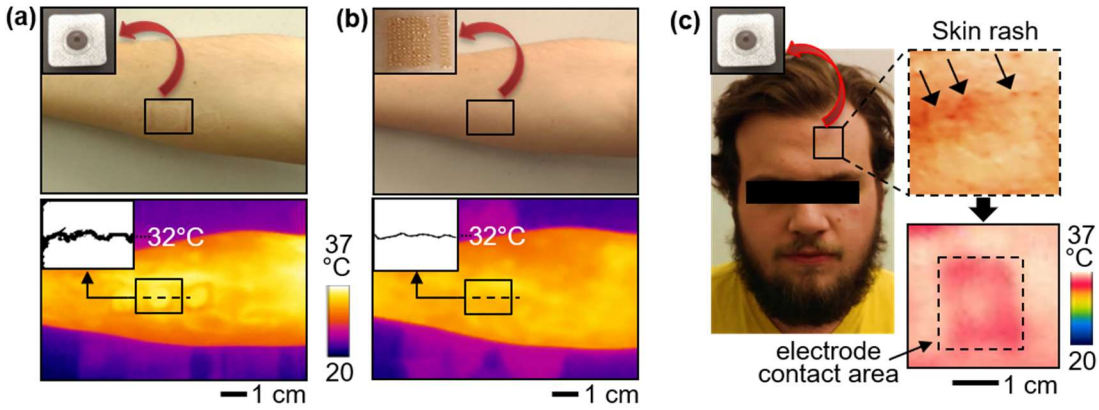

Figure 21. Comparison of infrared thermographs measured with (a) conventional and (b) fractal electrodes to reveal the side effect of the gel contacted to the skin (forearm) for more than 5 h. (c) Photo and thermograph of a gel electrode mounted on the forehead, causing skin rash.

1.11 Classification of EOG signals

A signal processing algorithm, designed by Matlab (Mathworks, Natick, MA), captures targeted EOG from eye movements of "blink" and "down" (raw data; Figure 22a). The next step is to process the signals via a 3rd order bandpass filter (Butterworth) at the range of 0.1 - 20 Hz to remove high frequency noise (Figure 22b). Afterwards, a series of peak detection methods are implemented (Figure 22c). The selected start and end positions are pertinent to the signal classification by increasing the detection accuracy. Examples of two

sliding windows in Figure 22d (left: “blink” and right: “down” movement) align the signals in the center since a misalignment results in incorrect classification. Lastly, the sliding window data are transferred into a linear discriminant analysis (LDA) classifier where a test dataset is compared to the training dataset. The LDA classification plot in Figure 22e shows a set of representative training data including both correct (o) and incorrect (x) classes.

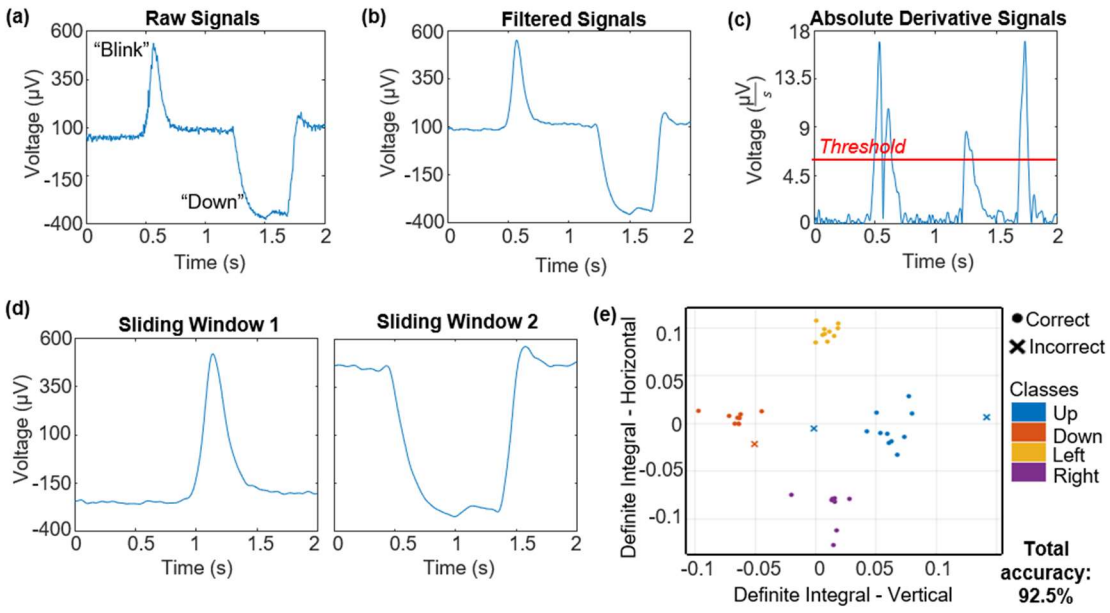

Figure 22. Signal processing sequence with a LDA classifier. (a) Raw EOG signals measured from eye movements of “blink” and “down”. (b) Preprocessed signals via filtering. (c) Absolute derivative signals to pinpoint target peak signals and apply a threshold boundary. (d) Sliding window algorithm using the detected peaks to parse the dataset into centered signals. (e) Machine learning algorithm using five distinct features from the centered signals and a LDA classifier to distinguish 4 classes of eye movements (up, down, left, and right).

Three separate logic algorithms are implemented, these are shown in Figures 23-25.

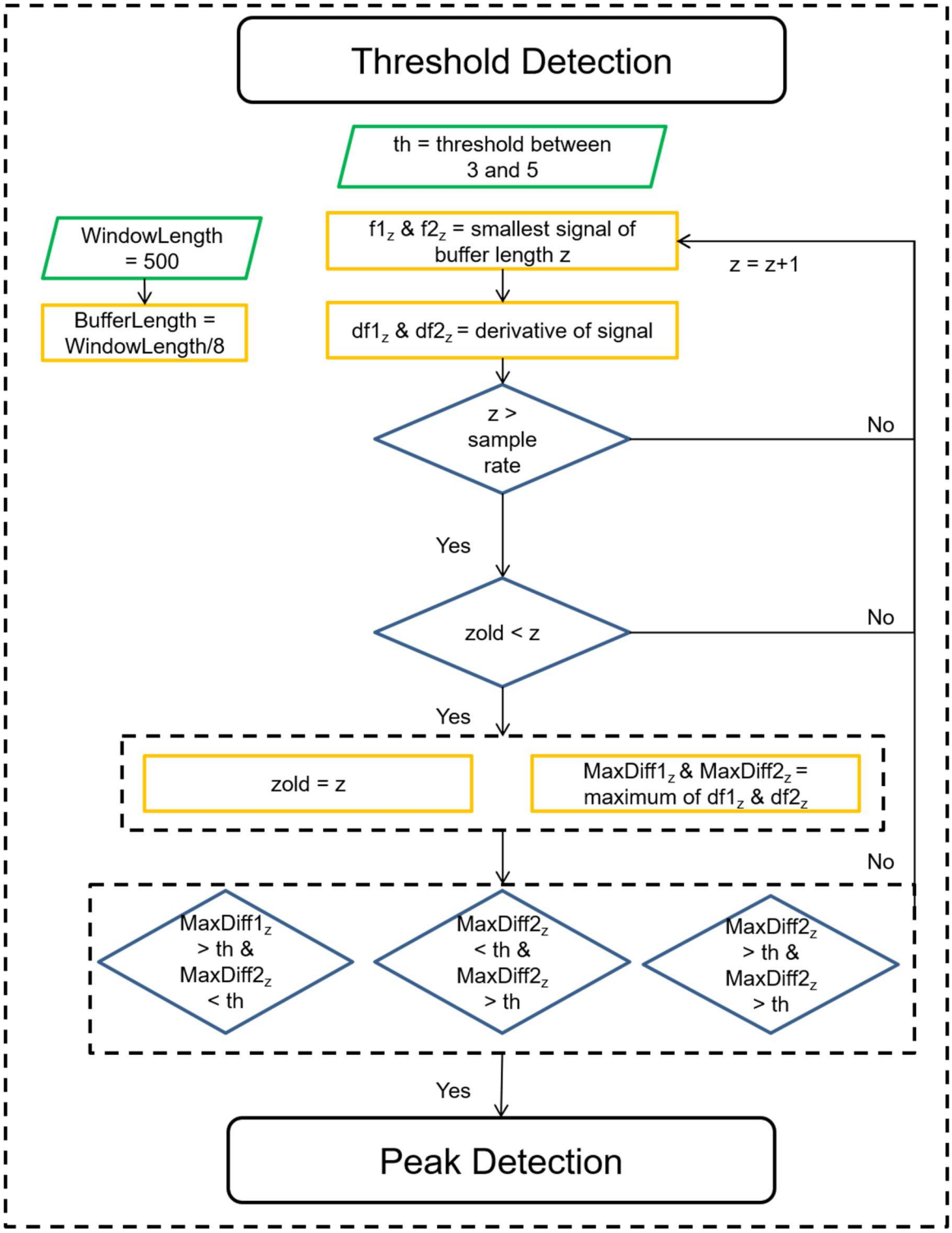

Figure 23. Threshold detection is the first of the three logic inputs.

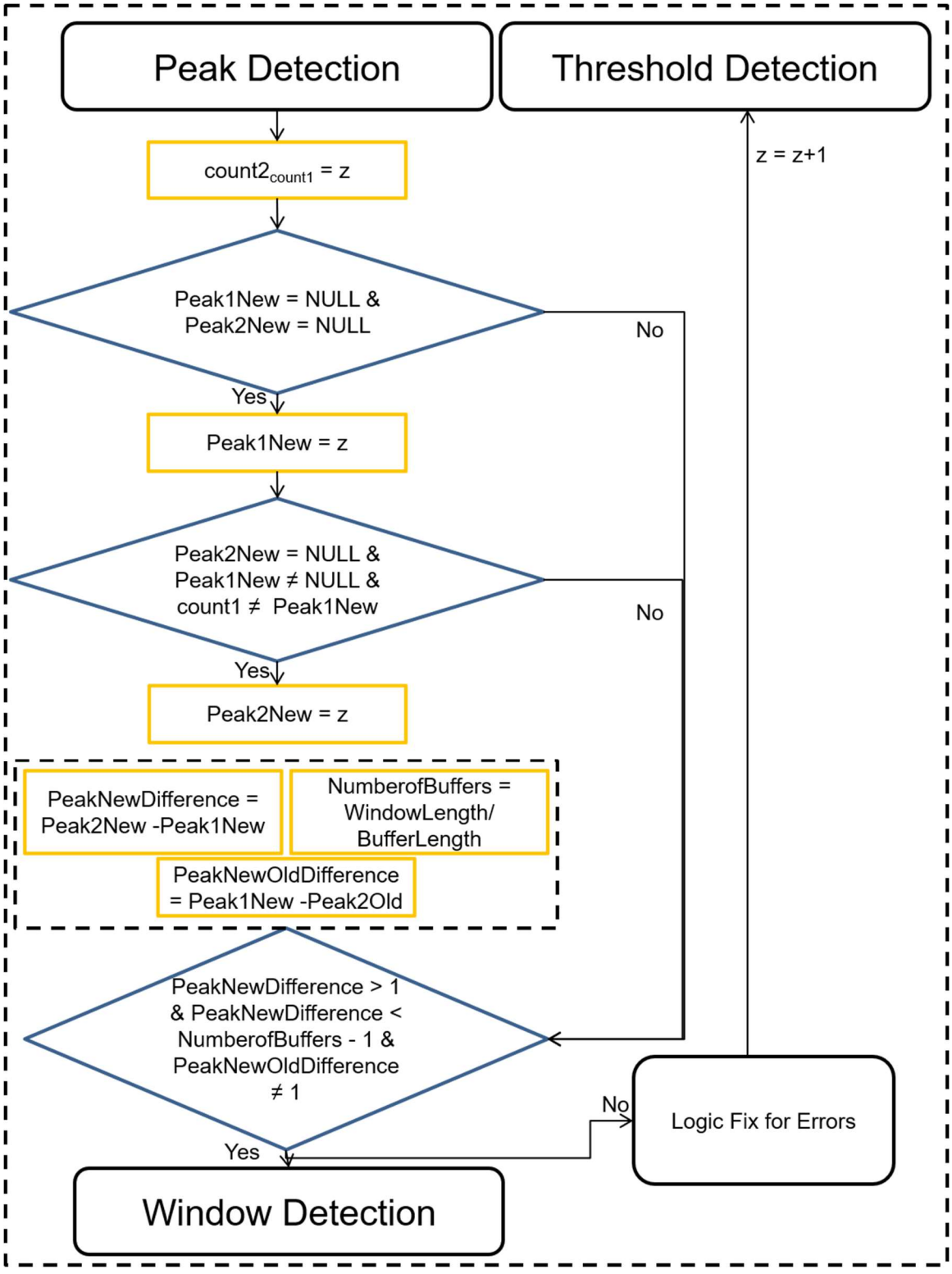

Figure 24. Peak detection is the second input of the three.

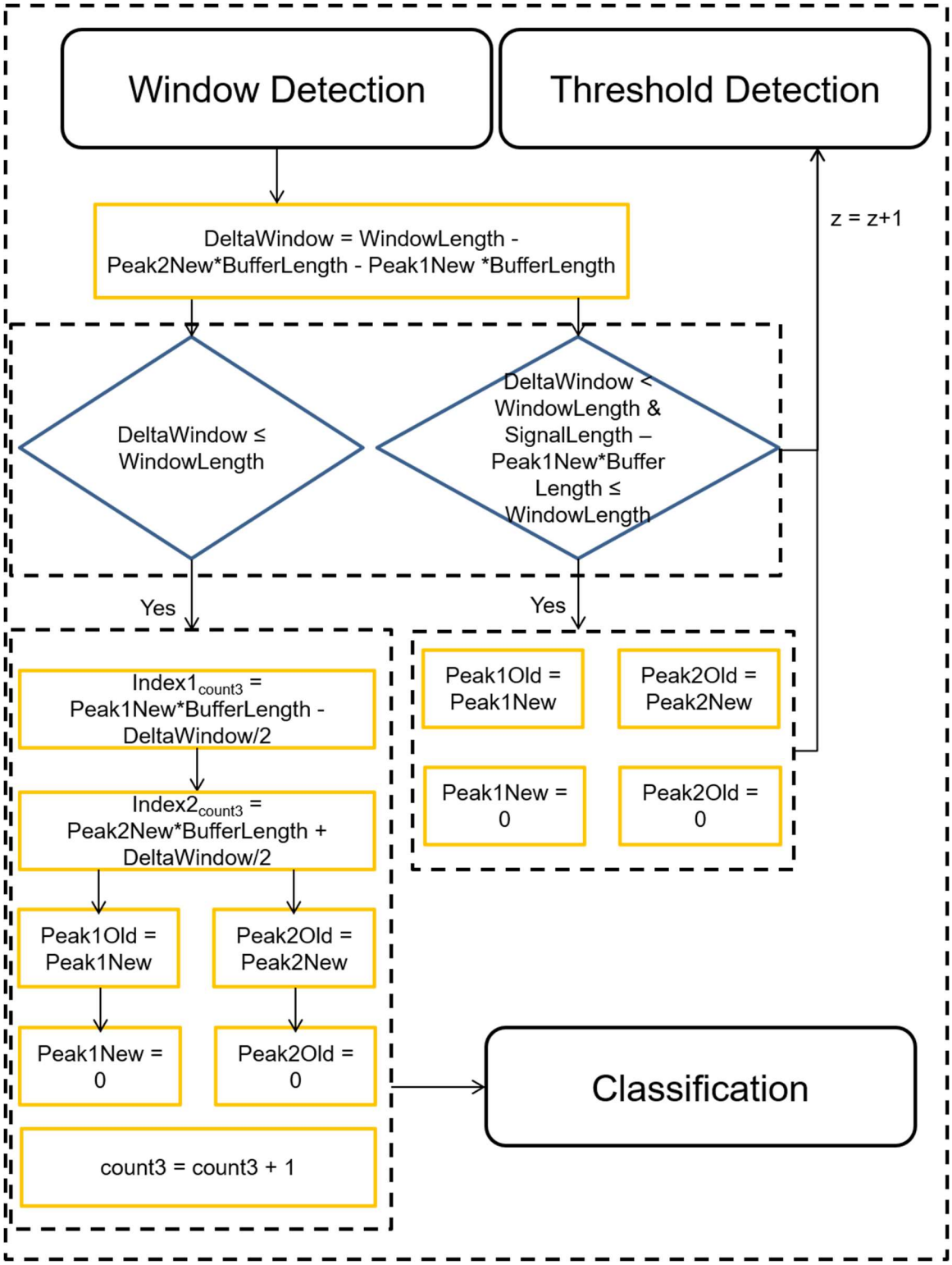

Figure 25. The final input is the window detection which resolves the final window for classification

The classification algorithm includes five features: definite integral, amplitude, velocity, signals mean, and wavelet energy. A common factor in the features is the sliding window indices, identified by t_1 and t_2. The area under the curve of the filtered signal (eq. 1) is acquired using the trapezoidal method. The signal amplitude (eq. 2) is determined from the derivative filtered signal, in which A_{t_1} and A_{t_2} are two consecutive peaks surpassing a threshold. A difference between the two peaks explains the order of the positive and negative peaks for each channel. The velocity (eq. 3) is simply the amplitude difference divided by the time difference and signal mean (eq. 4) is the average of the filtered signals. The Haar wavelet energy transform (eq. 5) outputs a set of scaled coefficients ($C_{a,b}$). The absolute multiplication of the coefficients creates the scalogram matrix, which is summed to resolve the desirable wavelet energy feature.

$$Definite\ integral = \int_{t_1}^{t_2} f(t)dt \tag{1}$$

$$Amplitude = A_{t_1} - A_{t_2}, where\ A = max\left(\frac{d(f(t))}{dt}\right) \tag{2}$$

$$Velocity = \frac{A_{t_1} - A_{t_2}}{t_1 - t_2} \tag{3}$$

$$Signal\ mean = \frac{1}{N}\sum_{t_1}^{t_2} f(t), where\ N = number\ of\ samples \tag{4}$$

$$Wavelet\ energy = \sum \left|C_{a,b} * C_{a,b}\right|, where\ C_{a,b} = \int_{t_1}^{t_2} f(t)\ \varphi_{a,b}(t)\ dt \tag{5}$$

A simulated program was used to make an accuracy assessment of the developed algorithm. Confusion matrices in Figure 26a and 26b compare the overall accuracy of two types of electrodes based on four classes of eye movements. The averaged accuracy from three subjects shows 91.9 and 94.1% for the conventional (Figure 26a) and fractal (Figure

26b) electrodes, respectively. The result presents an enhanced classification accuracy of the fractal electrode, while offering user-comfortable, intimate contact to the skin. The accuracy discrepancy between those electrodes is caused by the limited contact area of the rigid electrode (Figure 20c). Such an occurrence results in inconsistent signal recording of EOG. In addition, users wearing the rigid electrode expressed slight motion constraints caused by the rigidity of the electrode and adhesive pad, which might limit angular rotation of eyes.

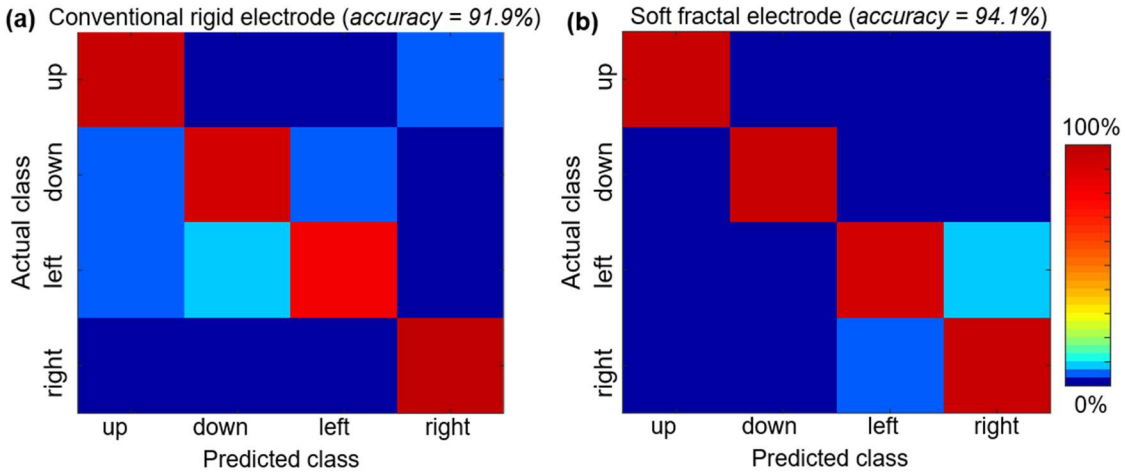

Figure 26. LDA classification of signals in real-time algorithm. (a, b) Comparison of confusion matrix from (a) conventional rigid electrodes and (b) soft fractal electrodes; The averaged classification accuracy from three subjects shows 91.9% and 94.1% for conventional and fractal electrodes, respectively.

Only the fractal electrodes demonstrate accuracy higher than 98% (average from three users) for ‘up’ and ‘down’ motions in the real-time EOG measurement. The maximum accuracy was achieved by optimization of five types of classification features in the LDA classifier (Figure 27), which was used to analyze all EOG signals for confusion matrices in this work. Comprehensive assessments (true positive, false positive, false negative, and true negative) of the classification, summarized in Table 1, supports the

enhanced device performance of the fractal electrodes, compared to the conventional setting. We validate our confusion matrix accuracy of each class with a secondary indicator by using the following calculation (eq. 6), where TP, TN, FP, and FN refer to true positive, true negative, false positive, and false negative, respectively.

$$Accuracy = \frac{TP+TN}{TP+TN+FP+FN} \tag{6}$$

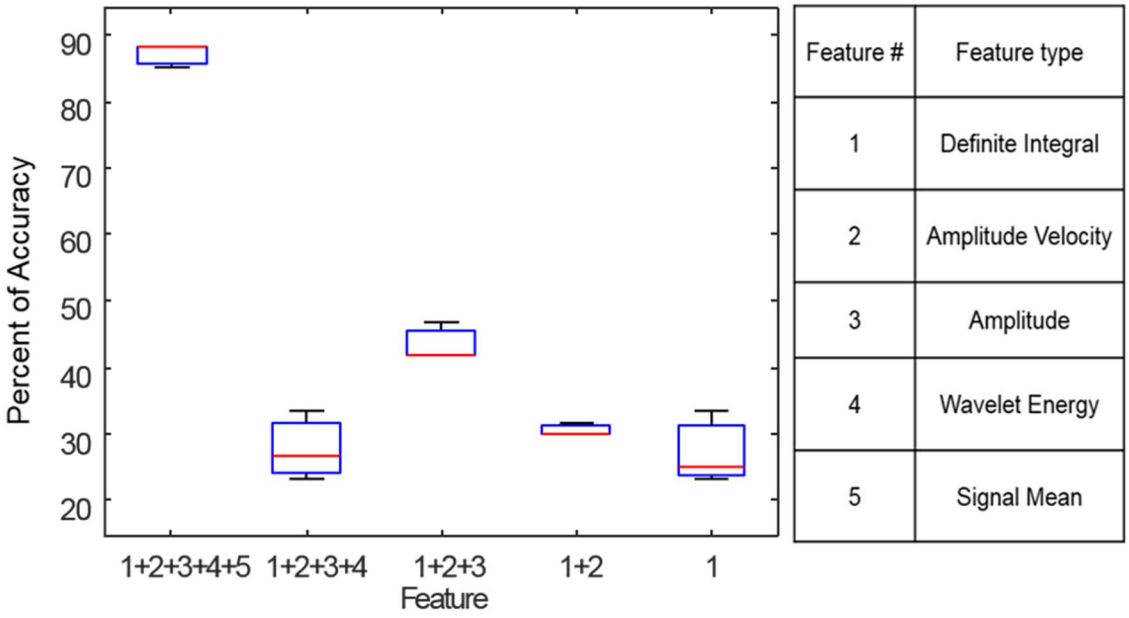

Figure 27. The final input is the window detection which resolves the final window for classification.

The true positive is determined from the value of each class on the diagonal of the confusion matrix, whilst the false positive is the value of the incorrect classifications of that individual class. The other two measurements resemble the data from other classes not from the observed class. As observed in the comparative accuracy test, the fractal device shows higher successful rates in classification than the conventional electrode. Table 1 shows that one of subjects using conventional electrodes has a high baseline noise that

gives low SNR, which attribute to a large number of false positives and false negatives in the "down" and "left" class. The SNR is calculated for each user individually using the first second of the trial as background noise and each sequential motion as the signal. The root mean square (RMS; eq. 7) of each window is used to calculate the SNR and then averaged for each channel of each user to quantify the cause of classification errors (summarized values in Table 2). Collectively, this quantitative comparison clearly captures the novelty of the soft electrode for persistent, ergonomic HMI applications.

$$RMS = \sqrt{\frac{1}{N}\sum_{n=1}^{N} |X_n|^2} \tag{7}$$

Table 1. Comparison of the classification accuracy between conventional and fractal electrodes (averaged values from three subjects; n=3). TP, FP, FN, and TN stand for true positive, false positive, false negative, and true negative, respectively.

	Conventional electrode					**Fractal electrode**				
Class	TP	FP	FN	TN	Accuracy	TP	FP	FN	TN	Accuracy
"Up"	127	13	8	369	95.92%	129	4	6	379	98.06%
"Down"	124	13	11	372	95.36%	129	4	6	379	98.02%
"Left"	112	9	23	384	93.92%	122	9	13	386	95.84%
"Right"	133	9	2	363	97.83%	128	15	7	380	95.80%

3.4. Demonstration of a human-wheelchair interface

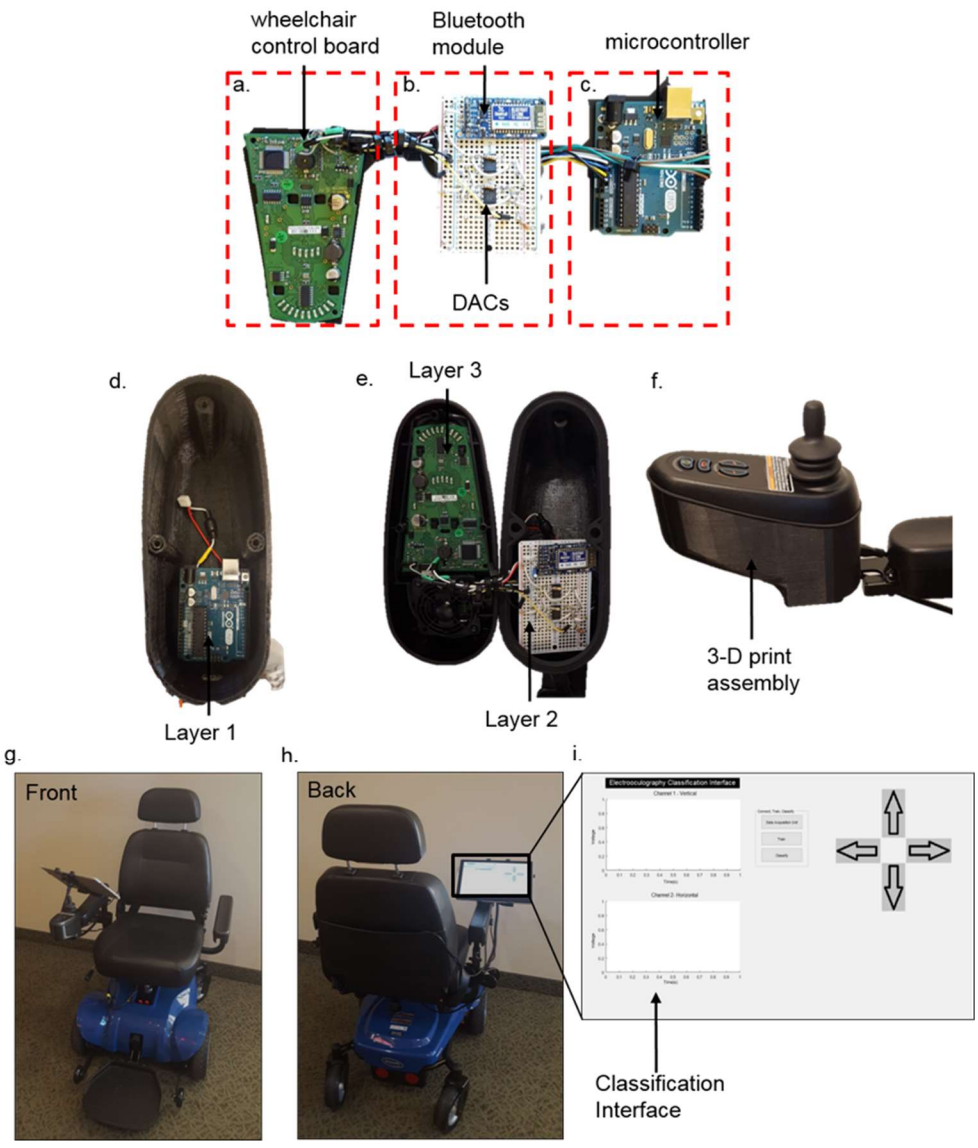

Figure 28. Wheelchair interface with microcontroller (a) The wheelchair control board accepts signals for forward, left, right, and neutral for our application. (b) Bluetooth module configures with the tablet; digital to analog converters allow step input to control the speed of the wheelchair. (c) Microcontroller configures the DACs. (d) 3-D printed assembly with layer 1, microcontroller. (e) Layer 2 and Layer 3 incorporate the protoboard module and wheelchair control board. (f) Fully assembled 3-D printed module. (g) Front view of the wheelchair with surface tablet attached. (h) Back view of the wheelchair with data acquisition software. (i) Classification interface from the tablet.

EOG signals acquired from the skin-like electrodes control a commercial wheelchair (Invacare™ Pronto, Elyria, OH) that includes the data acquisition system with real-time classification capability. A microcontroller (Arduino, Adafruit, New York City, NY) and digital-to-analog converters replace the wheelchair joystick; voltage signals are smoothly transferred to the wheelchair's DC motors and a designed Arduino code adjusts the speed settings to limit motion artifacts from the wires connected to the Bluetooth data acquisition unit (Figure 28). Four types of eye movements (up, down, left, and right), detected by the soft, fractal electrode around the eyes, control the robotic wheelchair: 'up' to go forward, 'down' to stop movement, 'left' to turn counter-clockwise, and 'right' to turn clockwise (Figure 29a and 29b).

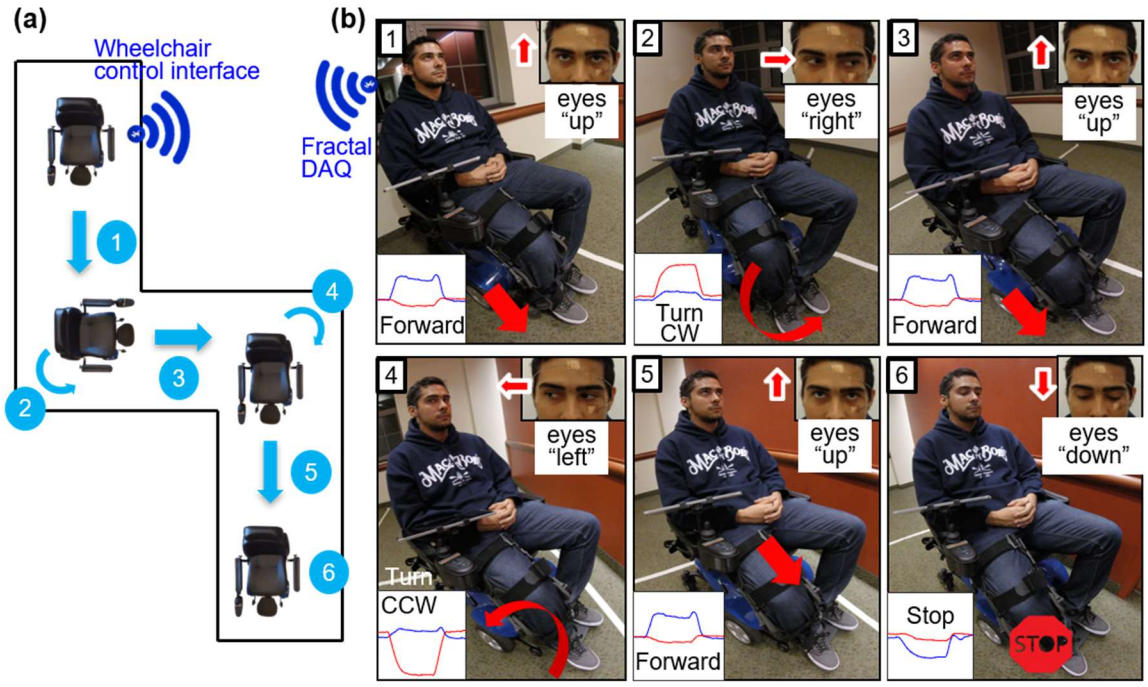

Figure 29. (a) Top view of entire pathways of a robotic wheelchair; classified EOG signals from eye movements are wirelessly transmitted from the fractal electrode/DAQ to the wheelchair control interface via Bluetooth. (b) A series of photos capturing a real-time, wireless control of the wheelchair via eye movements. There are four control commands

generated by different eye movements including “up”, “right”, “left”, and “down”. Insets show the raw EOG signals in correspondence with the eye movement from a subject.

Six consecutive commands operate the wheelchair in real-time to navigate the designed pathway from the position 1 to position 6 (Figure 29a). Each eye movement is recorded by two sets of vertical and horizontal fractal electrodes. A smart appliance (Windows-based tablet; Microsoft Surface Pro 4) provides the concurrent signal display and data saving options to the user.

Table 2. Root-mean-square values for three trials of conventional and three trials of fractals for all users.

	Conventional		Fractal	
User 1	Vertical(dB)	Horizontal(dB)	Vertical(dB)	Horizontal(dB)
Trial 1	25.56	27.66	17.69	26.15
Trial 2	20.96	26.77	15.66	26.31
Trial 3	29.07	19.32	17.98	32.76
Average	**25.20**	**24.58**	**17.11**	**28.40**

	Conventional		Fractal	
User 2	Vertical(dB)	Horizontal(dB)	Vertical(dB)	Horizontal(dB)
Trial 1	13.58	15.33	10.69	23.06
Trial 2	22.97	17.85	25.27	22.08
Trial 3	16.86	24.29	28.17	30.55
Average	**17.80**	**19.16**	**21.38**	**25.23**

	Conventional		Fractal	
User 3	Vertical(dB)	Horizontal(dB)	Vertical(dB)	Horizontal(dB)
Trial 1	20.86	31.96	17.69	26.15
Trial 2	16.35	25.71	16.27	26.21
Trial 3	22.25	26.70	20.53	27.82
Average	**19.82**	**28.12**	**18.17**	**26.73**

Total Average	**20.94**	**23.95**	**20.10**	**28.69**

1.12 Summary

In this chapter I resolved to develop a custom algorithm with a snappy classifier and my individual feature set for high accuracy classification of electrooculogram signals. Table 3 shows this works impacts compared to the literature. The signals were acquired for the first time using skin-electrodes, and because of these electrodes I was able to assess the quality of the signals based off the dimension of the electrode. This concludes that the gaps in the open mesh skin-electrodes do not affect the data collection as much as the placement of the electrode on the face. Additionally, the decreasing total area of the electrode reduces signal strength but is still comparable to conventional electrode.

Table 3. Literature comparison of this work's EOG-HMI and other EOG systems

	Sensor	Classifier	Classes	Accuracy	Real time	Application	Channels
[16]	Gel	Linear	6	85.2%	Y	HCI	2
[15]	Ag - Gel	SVM & HMM	5	98%	Y	HMI-wheelchair	3
[20]	Ag- Gel	DE - SVM	6	83%	N	Activity Recognition	2
[19, 62]	Ag-Gel/Dry	SVM	6	73%	Y	Activity Recognition	2
This work	Open-mesh skin-electrode	LDA	4/5	94.1%	Y	HMI-Wheelchair	2

AEROSOL JET PRINTING PROCESSING AND CHARACTERIZATIONS

1.13 Overview

Aerosol jet printing is a novel processing technology that has come out with numerous updates that enables it to replace standardized photolithography tools in various industries. Printed electronics are expected to improve costs, efficiency, and reduce environmental impacts in comparison to conventional photolithography. However the limitations of screen, inkjet, and other printing methods will not be able to overtake aerosol jet printing's fine resolution and superior versatility with not only the type of inks but also with deposition and etching capabilities. Due to those versatilities in the AJP system, a lack of materials understanding exists in films printed by AJP. Although similar to inkjet printing, various inks exist on the market that have not be characterized, such as Gold, Nickel, PDMS, Copper and Carbon Black. Other inks such as Silver and polyimide are frequently used even in AJP, but will still be characterized in respect to their compatibility with the other inks. These materials are heavily utilized in the flexible electronics, packaging, and bio devices industries. This chapter will shed some extravagant results on how to fine-tune the stiffness of the materials and devices by changing a few parameters. Other parts of the AJP such as the pneumatic atomizer and ultrasonic atomizer will be discussed in detailed to determine the appropriate method to use. And finally, the process techniques to fabricate the sensors will be discussed and the advantages of each.

1.14 Methods and limitations

In this work, nanoindentation of the aerosol jet printed thin films was conducted using a Hysitron Triboindenter (Hysitron, MN). Unfortunately, adhesion testing via scratching was not possible due to current system limitations. Consequentially, laser sintering was also not feasible due to inadequate consistency in intensities of the laser system. However, since copper and nickel inks require a special environment for sintering, they were characterized after rapid thermal annealing in a 2% formic acid vapor at 2 Torr. This environment ensures oxidation doesn't occur, but there are other methods such as photonic and laser sintering which allows sintering these materials in air. Due to the rapid annealing, limited oxidation occurs.

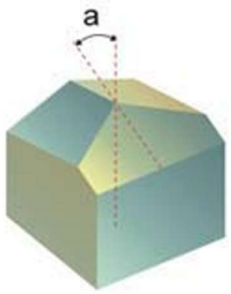

Figure 30. Berkovich tip with a half-angle of 65.3 degrees with a used to calculate the area function for hardness and modulus measurements

Nanoindentation of the Aerosol jet printed (AJP) films was possible by using a berkovich tip on the Hysitron Triboindenter, shown in Figure 30. The berkovich tip consists of a set of standards for calculations [62] such as the minimum thickness of indentation required for accurate measurements which is based off the area function, A.

$$h = \sqrt{A/25} \tag{8}$$

Equation 1 indicates the appropriate probing thickness (100 nm) required for measurements based off the area function that is empirically determined by probing a fused silica sample as the standard with a young's modulus of 70 GPa. The fused silica sample is probed 9 times to determine 8 coefficients that are used to fit the data points from the 9 successive forces applied on the sample. These coefficients translate into a short version of the area function indicated in equation 2.

$$A = 24.675h^2 + 0.562h + 0.003216 \quad (9)$$

After the area function is determined to be accurate the samples can be probed using an example loading curve shown in Figure 2; the distance that was penetrated in each sample which was variable depending on the sample's modulus and hardness. The red line indicates the calculated stiffness (S) from the unloading curve which is used to determine the reduced modulus in equation 3.

$$E_r = \frac{S\sqrt{\pi}}{2\sqrt{A}} \quad (10)$$

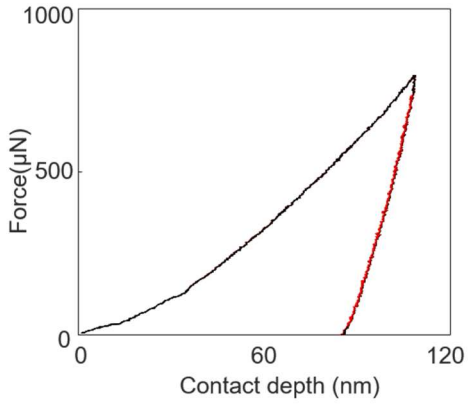

Figure 31. Loading and unloading curve of the nanoindenter at sample depth of 100 nm.

Afterwards, the reduced modulus is used to determine the young's modulus by using material properties from the berkovich diamond tip which has a young's modulus of 1.14 TPa (E_i) and poisson ratio of 0.07(ν_i). The other material parameters are indicated in Table 1. Finally, equation 4 is implemented with the material parameters for the indenter and the sample to conclude the final young's modulus of the probed samples.

$$E_s = \frac{(1-\nu_s^2)}{\frac{1}{E_R} - \frac{1-\nu_i^2}{E_i}} \tag{11}$$

Table 4. Bulk sample of young's modulus.

Sample	ν_s	Bulk Young's Modulus (GPa)
Polyimide	0.34	2.5
Gold	0.44	70-120
Nickel	0.30	190-220
Copper	0.36	117
PDMS	0.49	0.00057 – 0.0037
Silver	0.36	70-120

The hardness of the material is simply determined from the maximum load (P) over the area function (A) in equation 5.

$$H = \frac{P}{A} \tag{12}$$

In this work I probed 3x3 mm^2 samples of Gold, Silver, Nickel, Copper, Polydimethylsiloxane (PDMS) and polyimide (PI) (Figure 3) with the nanoindenter treated for varying conditions. This was followed by X-ray diffraction (XRD) and photoelectron spectroscopy (XPS) to determine the various grain orientation of the sample and a better understanding of the changes in chemical states of adsorbed oxygen and carbon as well as a decomposition of the capping agent. This was all supplemented with scanning electron microscopy (SEM) of the samples.

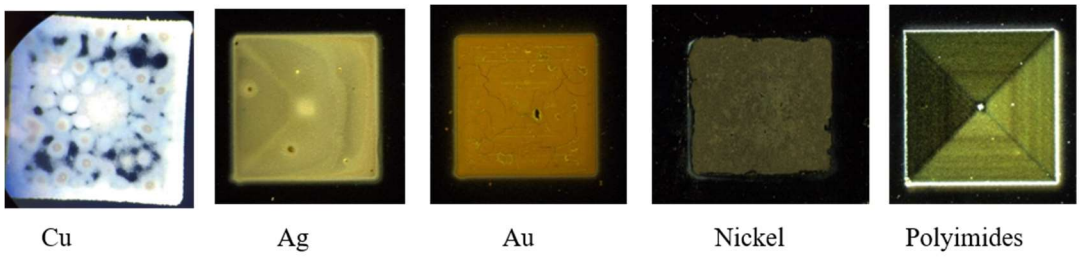

Figure 32. Various materials were printed on a silicon wafer for imaging and characterization. Only material not shown here is the PDMS sample.

1.15 AJP films characterization and results

The AJP printed samples were based off varying flow rates from the atomizer and the deposition head. Polyimide and PDMS were printed with the pneumatic atomizer (Figure 33a). The ultrasonic atomizer (Figure 33b) was used with low viscosity materials and inks such as the AgNPs, the AuNPs, NiNPs, and CuNPs. The aerosol stream carries the ink from the respective container to the deposition head with an inert gas flow of $N_{2,}$(Figure 33c) Gas flow rates for the ultrasonic atomizer is 30 SCCM and 20 SCCM on the atomizer. The pneumatic atomizer uses much higher flow rates for atomization which is better for viscous inks with higher weight percentage of NPs or polymers. The exhaust is held at

1470 while the atomizer flow is held at 1500 for the polyimide samples. The PDMS ink can be diluted significantly with toluene to print thick layers of PDMS. First, mix parts A:B of PDMS together and dilute the mixture with 40% toluene by weight. The toluene acts as the carrier solvent and maintains the material from curing during the atomizing process.

1.15.1 AJP printed metals and polymers sintering experiment

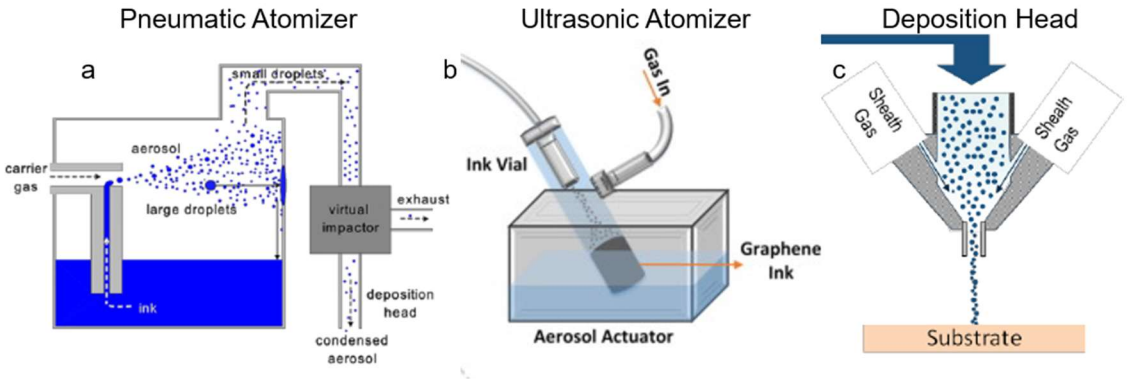

Figure 33. The different atomization techniques used in this work. (a) Pneumatic atomization with a single jet. (b) Ultrasonic atomization using a piezo transducer for excitation. (c) The aerosol stream is transferred to the deposition print head.

After printing, the first set of samples were sintered at 250 °C in an ambient oven or a hot plate. The nanoindentation results show high discrepancies in modulus from the bulk properties. A two point probe measurement is used to determine resistance of the sample to make sure it is low for flexible and stretchable electronic applications. Figure 34 shows promising results with low modulus aerosol jet printed thin films. The average modulus for the materials were measure to be between ~ 2 GPa and 8 MPa (Table 5). This extremely low modulus seems to be due to the lack of full sintering of the samples at low temperatures (250 °C) and time (< 1 hr) resulting in weak porous sections. The gold sample

appears to crack easily when heated up to high temperatures at higher ramp rates so a very slow ramping process (10°C) was used after the first test.

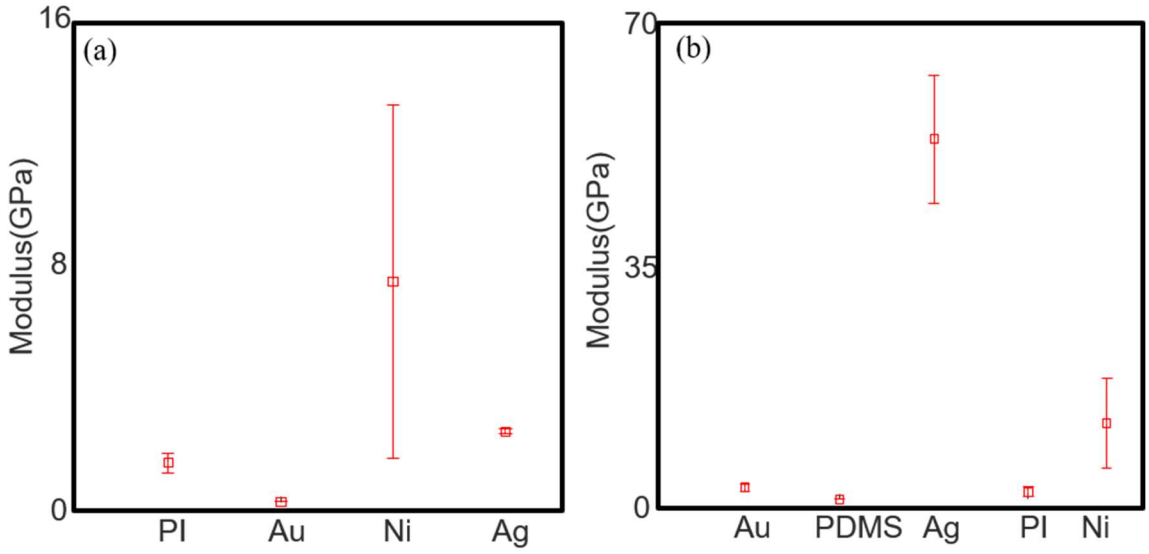

Figure 34. Sintered materials at (a) 250 °C for 1 hour and (b) 300 °C for 12 hours with the plotted young's modulus. The PDMS sample was cured at 110 °C

However, the gold sample wasn't the only problem, nickel, and copper both turned into nickel and copper oxide films which was evident from the color changes and lack of a metallic finish. The oxidation occurred because of the lack of an inert gas environment. The use of printed polymers in the AJP system enables for thick and thin film prints. The thin film properties are important when making capacitive sensors[63] for higher sensitivity. The thick film materials can be used for transfer processes in flexible and stretchable electrodes as well as thin film boards where a thick dielectric is necessary for Bluetooth antennas. Finally, PDMS has never been printed using aerosol jet printing because of its viscosity, but by dissolving the uncured polymer into a solvent such as toluene, it can be printed easily. This makes PDMS a good candidate for microfluidics for micropumps, valves and other applications.

Table 5. Two sets of samples sintered at different temperatures and time in an ambient oven.

	Sintered at 250 °C for 1 hour		Sintered at 300 °C for 12 hours	
Samples	Avg E_s (GPa)	Avg Hardness (GPa)	Avg E_s (GPa)	Avg Hardness (GPa)
Polyimide	1.27	0.115	1.13	0.0167
Au	0.0168	0.0034	1.7	0.141
Ni	7.15	0.0014	9.88	0.086
Ag	2.28	0.0684	52	0.39
PDMS*	N/A	N/A	0.016	0.0030

In the second set of samples a higher temperature was used which increases the conductivity and modulus of silver and gold. The gold modulus increased by an order of 100 but it is still lower than bulk gold by an order of 10. Silver on the other hand has an average modulus of 52 GPa which is closer to the bulk material young's modulus. The increased moduli for the metals is very good for stiffer applications where the metals need to have high strength. The PDMS sample was cured at 115 °C which is recommended by the manufacturer for a fast cure. Because of the thin film properties of PDMS, it was much stiffer than its bulk form. PDMS stiffness increases as it becomes thinner due to strain hardening, but this is controversial because it could be results of the underlying stiffness of the substrate[64]. Table 5 summarizes the modulus and hardness of the sintered samples for the first experiment at 250 °C for 1 hour and the second experiment at 300 °C for 12 hours.

Since not much work has been done on sintering gold nanoparticles, it was determined that another assessment of gold nanoparticle sintered at various temperature and times is necessary. Figure 35 shows sintering at 200, 250 and 300 C, for 1 hour, 3

hours, and 12 hours. The results of this were mixed because the samples would crack at longer times at the highest temperature. In this case the lowest time of sintering at 200 °C showed the highest modulus. This is highly conflicting with previous results but there is more variability in the lower temperature. The highest sintering temperature is 300 °C and it shows the most precision as well as a similar modulus with the 2nd set of data at 300 °C.

Table 6. Gold sintered at varying temperature and times

Samples	Avg E_s (GPa)	Avg Hardness (GPa)
Au – 200°C	5.40	0.50
Au – 250°C	1.33	0.043
Au – 300°C	1.11	0.164

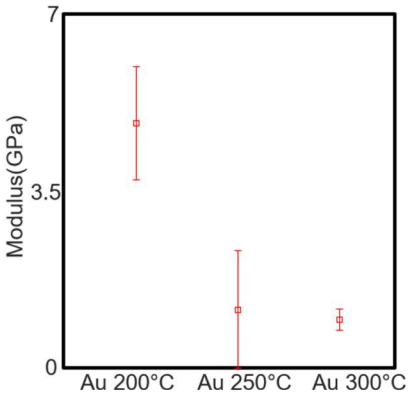

Figure 35. The third set of samples were tested for the sinterability of gold at temperatures 200 °C, 250 °C, and 300 °C for 1, 3 and 12 hours.

The copper ink was sintered in an ambient oven at first, but the ultimate result was oxidation of nanoparticles that penetrated deep into the sample's thickness. Therefore, rapid thermal annealing with formic acid for 30 minutes at 250°C creates a low modulus film, the average modulus of the nanoindented Cu films were 2 GPa, which is significantly lower than its bulk properties. It is assumed that long term treatment may increase its modulus over time.

1.15.2 AJP atomic characterization

After all mechanical properties were understood, some material studies using X-ray photoelectron spectroscopy (Thermo K-Alpha) and X-ray diffraction (Panalytical

Empyrean) were conducted. The XPS results are indicated in Figure 36a for the various silver nanoparticle results characterization where an increase of adsorbed oxygen is shown by almost 2x. Figure 36b shows the results for gold nanoparticles with an increase in oxygen content that of the gold NP. This is a surprising result because it is common knowledge of gold's unique ability to not tarnish when exposed to air. However, gold can form various oxides and it is evident form the changing of the full width half maximum of the oxygen as well as the increase in atomic % of oxygen, Figure 36c. Other studies have shown XPS results of thin film and gold nanoparticle oxidation but with catalyst reactions[65] and some demonstrate the oxidation of the thiol groups of the binder/capping agent[66].

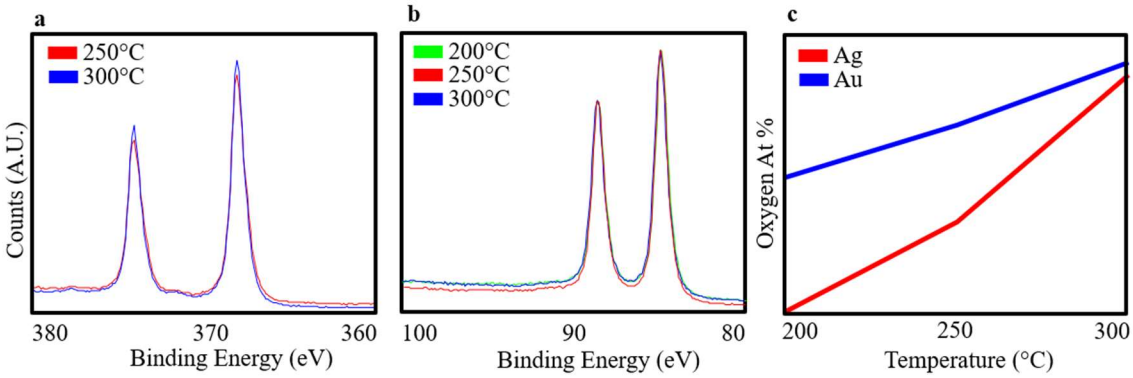

Figure 36. XPS results of (a) silver and (b) gold sample with a change in (c) oxygen adsorbed due to the ambient environment.

Finally, X-ray Diffraction (XRD) and scanning electron microscopy (SEM) results show the crystallography of the gold and silver film after sintering, although the grain sizes become larger the peaks do not become broader for the XRD results, signifying there is no increase in grain size. It can be seen in Figure 37a, that the silver nanoparticles are not very porous because of the high temperature for sintering which ensures higher mechanical stability and lower resistivity. Particles sizes have increased from 5 nm particles to more

than a few hundred nanometers. In the case of gold (Figure 37b) sintered at 250 °C, large cracks were formed and it seems to have fully sintered below the top layer but just like the silver, the size of each particle has increased. If we increase the temperature further and increase the time the nanoparticles are no longer visible because it seems to have formed into a melt and reorganized its entire grains to become much larger (Figure 37c). The final SEM image of nickel (Figure 37d) shows small particles dispersed with very little sintering and due to the lack of conductivity and XPS results of high oxygen %, it is assumed that the nickel is actually nickel oxide NPs.

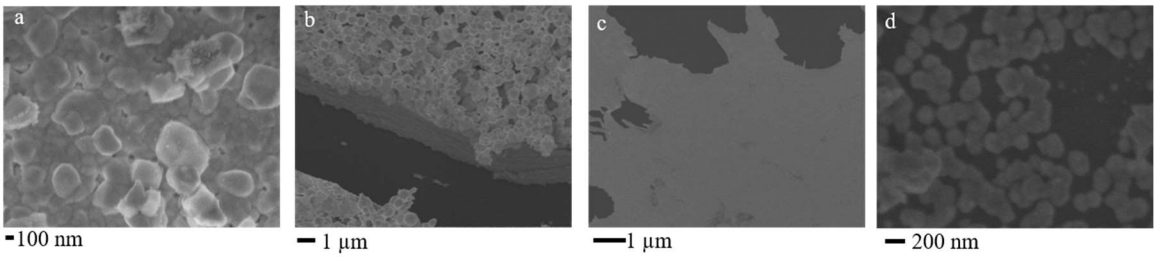

Figure 37. SEM images of Ag, Au and Ni. (a) Ag sintered at 250 °C for 1 hour; (b) Au sintered at 250 °C for 1 hour; (c) Au sintered at 300 °C for 12 hours; (d) Ni turned into nickel oxide nanoparticles sintered at 200 °C for 1 hour.

1.15.3 Conclusion

The use of aerosol jet printing enables the versatility of utilizing various material groups that is not possible with thin film deposition techniques. There is more novelty associated with utilizing the mechanical properties towards flexible electronics because we can increase the compliance by reducing the overall moduli of the composite structure. A variable modulus may yield higher strain with a larger elongation at break. Better sintering techniques need to be used to understand the properties of Nickel and Copper because of the ability to oxidize quickly. Furthermore, some additional testing with atomic force

microscopy and nanoindenter scratch function could enable a visual observation of the roughness and the adhesion force of the material to a silicon substrate.

1.16 AJP skin-electrode fabrication

A highly sensitive detection of electrophysiology signals requires a low skin-electrode contact impedance and minimized motion artifacts. Even though a conventional electrode offers a low-contact impedance due to the electrolyte gel, the combination of the sensor rigidity, size, and associated adhesive limits an application onto the sensitive and highly contoured regions of the nose and eye areas. Here, I developed a novel additive manufacturing technique (Figure 38a) for high throughput fabrication of an ultrathin, highly stretchable, comfortable dry electrode for electrophysiology detection. The potentially low-cost and scalable method using aerosol-jet printing (AJP)[67] allows a direct printing of an open-mesh structure onto a soft membrane (Figure 38a) without the use of expensive nano-microfabrication facility[68]. For successful printing, I conducted a parametric study to understand the material properties of silver nanoparticles (Ag40XL, UT Dots) along with the controlled deposition through various nozzles of the AJP (Figure 38b; AJ200, Optomec). The ultrasonic atomizer stores the 5 nm silver nanoparticles in xylene within a thin glass vial that allows ultrasonic acoustic waves to propagate and develop a standing wave at the interface. This transfers the solvent and particles into small droplets (Figure 38b). These droplets are transferred to the deposition head and nozzle before placement on the polymer substrate.

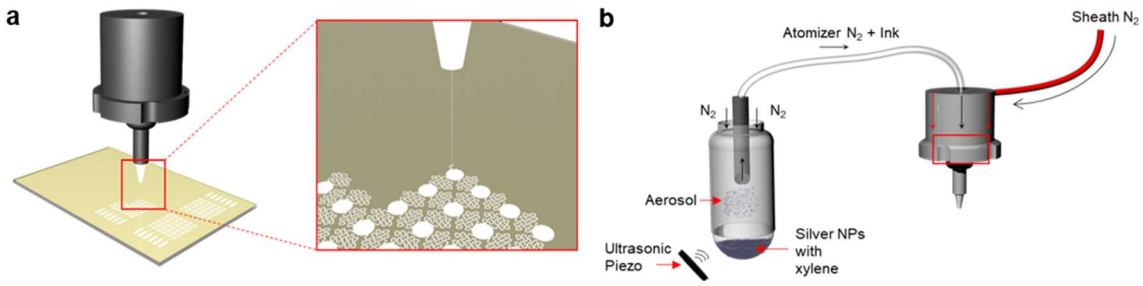

Figure 38. (a) Aerosol jet printing out of deposition head with a close up of deposition of a skin sensor. (b) Atomization begins in the ultrasonic vial and a carrier gas (N_2) flows the ink droplets through tubing, the diffuser, and the deposition head where a sheath gas focuses the particles into a narrow stream with ~ 5 µm diameter.

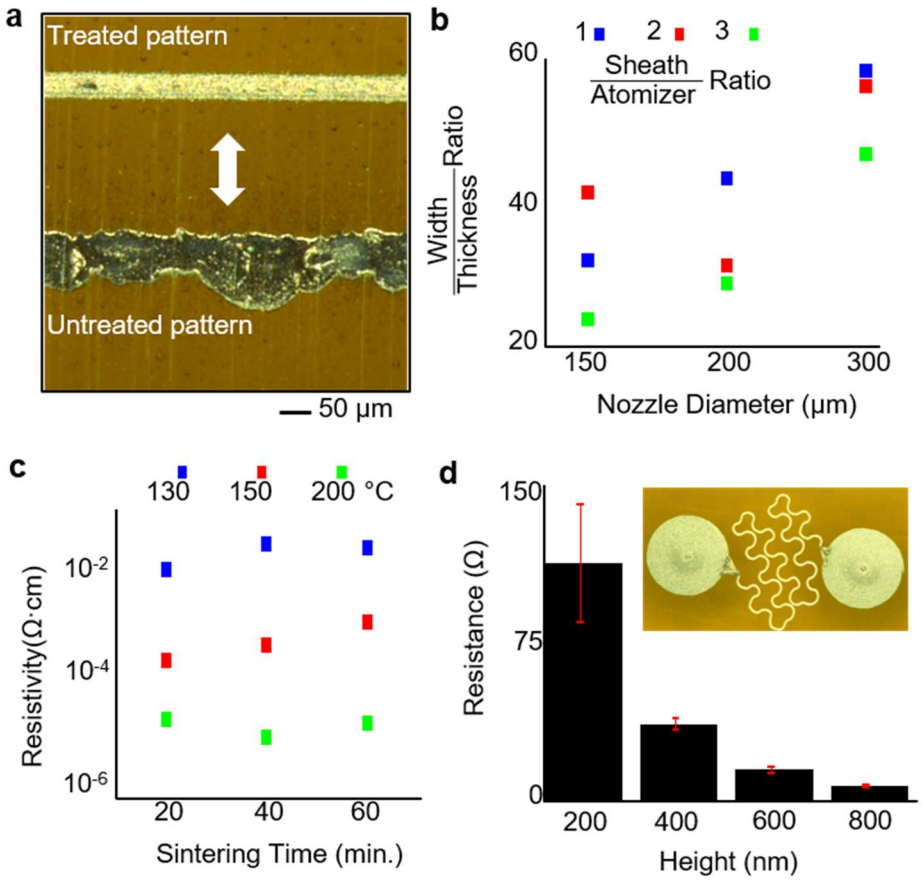

Figure 39. (a) Platen is heated to ensure evaporation of the solvents, but surface treatment with plasma cleaner enables clean lines (top). Otherwise the traces tend to form into low energy bubbles over a large area. (b) High focusing ratio with low width/thickness ratio enables lower resistivity. (c) Resistivity measurements from four point probe was determined for various sintering temperatures and time. (d) Ultimately, the resistance of the electrodes needs to be low so a two point probe measurement demonstrates the resistance across a fractal electrode in series.

Prior to the electrode fabrication, printed lines were assessed for its wettability by qualitatively determining the surface energy on a substrate (polyimide). Plasma treatment along with platen heat was used to produce fine features (Figure 39a). To find the optimal printed structure, we varied a few key parameters, including the ratio of line width and thickness for each nozzle diameter with different focusing ratios and sintering time with different temperatures (Figure 39b-c). In the focusing ratio (Figure 39b), the sheath flow

controls the material flow rate through the deposition head and the atomizer flow controls the material leaving the ultrasonic atomizer bath. The highest focusing ratio has the lowest width to thickness ratio, which ensures a smaller width for a higher thickness. A four point probe system (S-302-A, Signatone) measures the resistivity of the printed ink sintered at different temperatures and time periods (Figure 39c). As expected, multi-layer printing of AgNPs provides lowered resistance (Figure 39d).

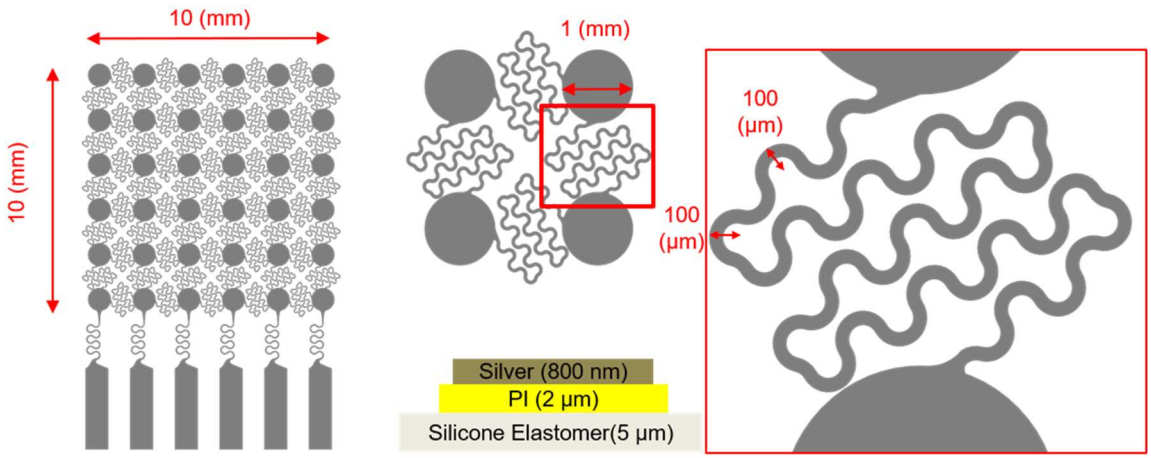

Figure 40. Design of electrode. Skin-electrode dimensions are 1x1 cm^2 and approximately 1 mm diameter circles. The fractal pattern is maximizing surface area for best contact, but also increases resistance from end-to-end of the electrode. The radius of each curve is 100 μm with a trace width ranging from 20 μm – 60 μm depending on the type process used.

This yields a lower resistance for finer traces which is necessary for the ideal sensor geometry (width of a trace: 30 μm and entire dimension: 1 cm^2; Figure 40). To print this geometry a maximum nozzle size of 150 μm may be used otherwise adjacent meanders sinter to each other reducing the maximum stretchability. The good conductivity of printed traces was ensured by the sintering process at 200°C (Figure 41a). Images from scanning electron microscopy (Figure 41b) reveal the agglomeration of NPs inside the oleylamine binder and after dissociation of the binder. In addition to the previous characterization, the

lowest possible modulus is desired to be compliant with the polymer layers, X-ray diffraction shows various crystalline planes of AgNPs that become more evident after sintering due to the increasing grain sizes, demonstrated by the decrease in broadband characteristics of the peaks in Figure 41c. This change in crystallinity is due to the decomposition of the oleylamine capping agent[69]. In Figure 41d, Raman spectroscopy shows a narrow peak at 2918 cm^{-1} before sintering which is converted to a much broader peak centered at 2932 cm^{-1} after sintering. This indicates a decrease of CH_2 bonds in the capping agent as well as small shift in the amine group (1400-1600 cm^{-1})[70].

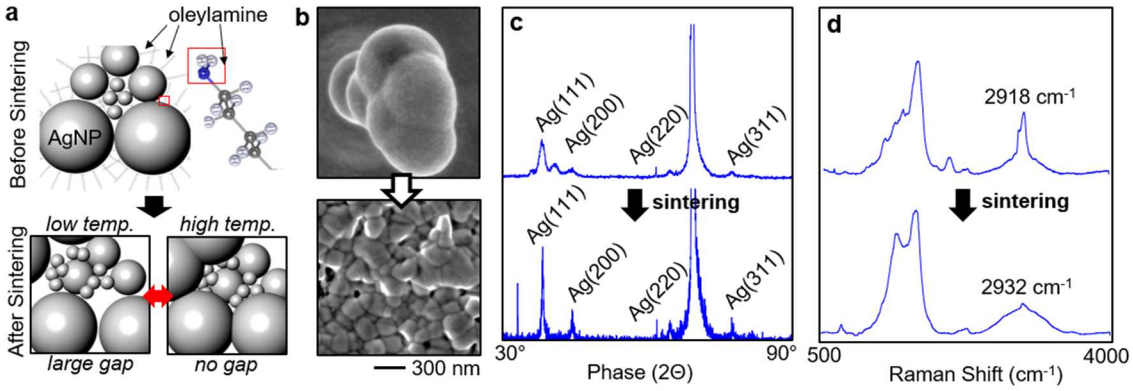

Figure 41. (a) AgNPs capped with oleylamine fatty acid that prevents agglomeration ends up breaking down after low temperature and high temperature sintering. The grain size for small NPs increases at low temperatures and then bigger NPs at higher temperatures. (b) SEM images indicate the dissociation of the binder material after sintering (c) XRD analysis shows larger crystallization peaks after sintering and the recrystallization of peaks along (111), (200), and (311) crystal planes. (d) Raman spectroscopy demonstrates the loss off carbon and hydrogen peaks from the binder dissociation near wave number 2900 cm^{-1}.

After a strong understanding of the AJP materials was determined, skin-electrodes were printed using a high throughput process. The ultrasonic atomizer was filled with 1.5 mL of AgXL ink and atomized at a current of 0.6 amps. Before atomizing, the sheath flow was turned on at the indicated flow rate for the nozzle to determine the feedback pressure of the

system for clogs or leaks. Sheath flow was dropped down to 30 sccm and the atomizer flow was set to 15-20 sccm depending on print quality. The deposition head was placed 3-5 mm from the substrate which ensures beam convergence onto the substrate. Line widths printed using the 150 µm nozzle range from 20 µm to 60 µm, but as shown in Figure 39d, each pass of the nozzle deposits 200 nm. This is the thinnest layer of silver that can be printed for skin-electronics at the maximum platen speed of 10 mm/s. The speed is limited by the geometry that is printed, and although curves are easier to print compared to 90 degree turns, the maximum speed for skin-electronics with the 100 µm radii in Figure 40 is 10 mm/s.

Setting up the system for long term processing needs meticulous preparation of the deposition head, the nozzle, and the tubing. A plethora of issues could ruin a long-term print of an array of sensors. The printing substrate was cleaned with isopropanol (IPA), acetone, and deionized (DI) water. Afterwards it was dehydrated and plasma cleaned for 1 minute. PI-2545 was then spin coated onto a 50 mm x 75 mm glass substrate at 2000 RPM and baked for 1 hour at 250 °C. An array of eight electrodes was printed with 2 layers of silver on the polyimide substrate at a speed of 10 mm/s. These samples were printed in 2 hours and then sintered in an ambient oven for 1 hour at 250 °C. At this point there are two options, either the sample can be placed in an oxygen RIE for etching or a second layer of polymer photoresist can be aligned and deposited onto the silver to protect it in the RIE. If the sensors are not protected, they will oxidize and will need to be reduced in argon plasma. However, if the photoresist is printed well, then the silver will not oxidize and will stay metallic. After removing from the RIE, if necessary, the photoresist is cleaned off with acetone and the resistance is measured to be between 50Ω and 100Ω with two point probe

measurement. The high resistance is due to the length of the interconnects between circular nodes of the sensor.

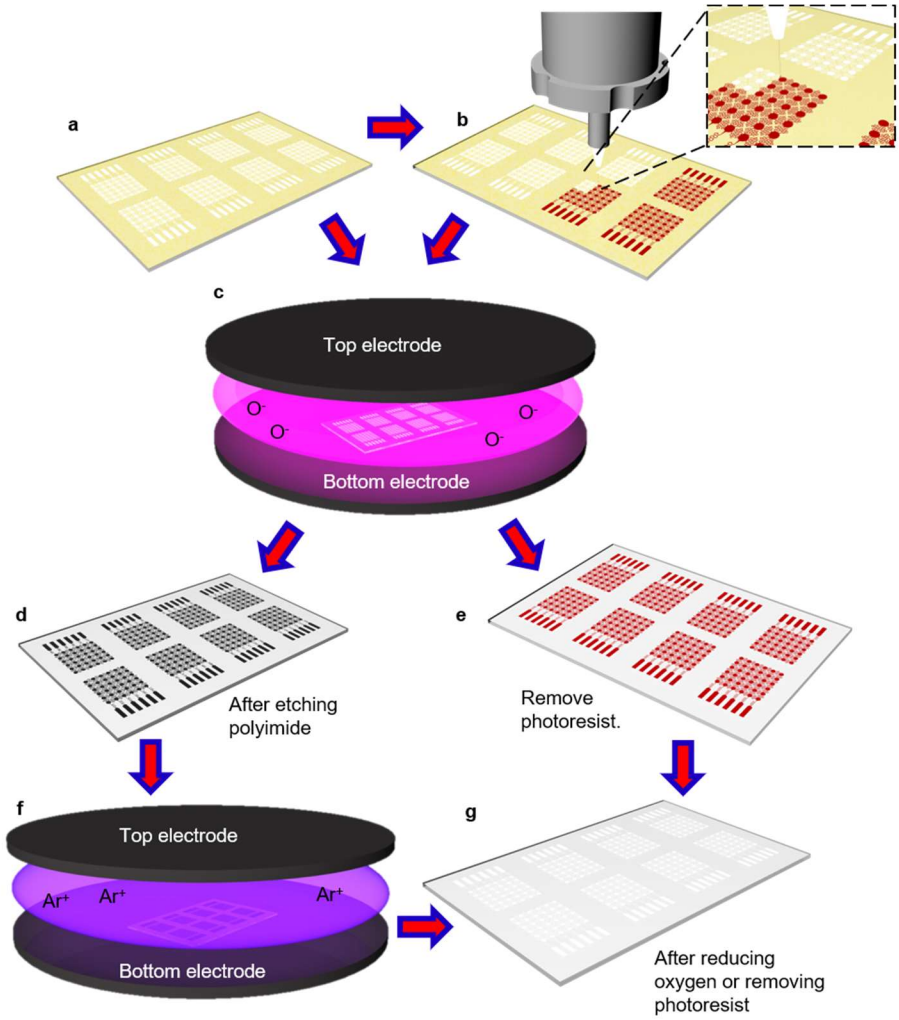

Figure 42. (a) After atomization and deposition, a full electrode array is ready to be processed by dry etching. There are two options for dry etching, first option is to just go ahead and etch the polyimide after printing and second option (b) is to deposit photoresist onto the silver patterns by alignment. A close up shows the deposition location and the beam diameter of 5 µm. (c) After depositing all electrodes on the substrate, the sample can be treated in oxygen plasma to etch the polyimide. (d) After etching, oxygen has impinged the silver and needs to be reduced or (e) the photoresist stays intact and the silver is untouched but the polyimide is etched away. (f) The final reduction step is conducted in a RIE with argon gas which removes most of the oxygen. (g) The final electrode array comes out of the RIE bright white after removing photoresist or reducing.

1.17 Conclusion

Ultimately, Aerosol Jet Printing is capable of versatility in printed electronics with the numerous nanoparticle inks. The surface tension of the inks does not need to be as finely tuned as inkjet printing because of the continuous stream. As shown in section 4.3.2, the materials characterization was limited to a set of metal NPs usable in flexible electronics. These metals are used in the packaging and printed board industry for creating interconnects and diffusion barriers for solders. The advantage of using aerosol jet printing in newer flexible electronic applications is the tunability of the mechanical properties of these materials to be electrically conductive while undergoing larger strains. This ensures long term stability and usability of sensors and circuits on the skin.

ELECTROCULOGRAMS FOR CONVERGENCE INSUFFICIENCY

In chapter 3, I discussed electrooculograms for human-machine interfacing with microfabricated sensors and a conventional Bluetooth radio. In this section, I continue to describe the impact of electrooculograms with a different method of recording that has not been done before with skin-electrodes or conventional electrodes. Additionally, I demonstrate the first flexible circuit for high resolution electrophysiology recording with a serpentine structure that conforms to the skin. EOG was used to record eye vergence motions from 14 subjects using a physical and virtual reality apparatus. Custom positions were designated towards the different locations that humans observe in daily life, smartphone, monitor, television. The goal of collecting the eye vergence data was to correlate it towards ocular disorders such as eye vergence and strabismus issues. The gold standard for clinical recording of ocular disorders is videooculography (VOG), but it cannot be used to measure eye vergence under a VR headset, therefore we use the alternative, electrooculography method. EOG has never been used for eye vergence measurements due to the limitation of conventional gel and hydrogel electrodes. Conventional electrodes are too bulky to conform to the contour of the nose along with a second limitation of their inability to compress underneath a VR headset. Fortunately, we fabricate skin-electrodes which are stretchable and flexible enough to compress under a VR headset as well as conform to the contour of the human nose. Surpassing these two limitations we herein present the first eye vergence study utilizing EOG signals with stretchable and flexible electronics for human-computer interfacing. A VR headset with a

customized android application presents our visual therapy program for eye convergence and divergence motions. An external MATLAB program is used to train and validate precise eye vergence motions of 14 healthy subjects for offline and real-time classification.

1.18 Overview of eye vergence and skin-electrode

Recording eye vergence via EOG has been deemed difficult[71] by ocular experts because of the signal sensitivity, warranted by the lower conformality and motion artifacts of conventional gel electrodes in comparison to skin-like, soft electrodes[27, 72, 73]. Additionally, a pragmatic experimental setup that can invoke a precise eye vergence response is lacking. Therefore we developed a VR-integrated eye therapy system and wearable ocular electronics (Figure 43a). The home-based therapeutic system (Figure 43a) incorporates a set of stretchable aerosol-jet printed electrodes, a VR device, and soft wireless electronics on the back of the user's neck. The portable system offers a highly sensitive, automatic detection of eye vergence via a data classification algorithm. The VR therapy environment (Figure 43b) simulates continuous movements of multiple objects in three varying depths of near, intermediate, and distance which corresponds to 1°, 2°, and 3° of eye motions, which enables home-based ocular therapeutics without the use of physical apparatus. Audio feedback in the system interface guides the user through the motions for high-fidelity, continuous signal acquisition towards training and testing purposes.

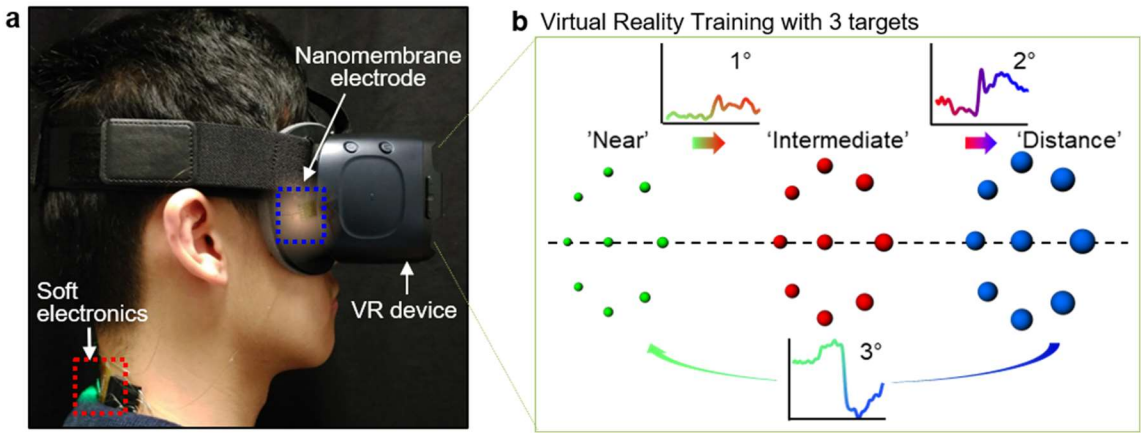

Figure 43. Therapeutic device with training program and wearable devices for disease diagnoses. (a) Virtual reality headset with skin electrodes are subtly placed underneath the gear VR. (b) Near-> Intermediate -> Distance signals are shown for the electrodes as the user follows the training program for the corresponding color and position.

The performance of the VR system (Figure 44a) in vergence recording is compared with a physical apparatus (Figure 44b). We engineered nanomaterials to design an ultrathin, nanomembrane sensor for high-fidelity detection of slight eye movements via conformal lamination on the contoured areas around the eyes and nasal region (Figure 45a). A scalable additive manufacturing method using aerosol jet printing was used to fabricate the skin-wearable sensor, which was connected to a fully portable, miniaturized wireless circuit that is ultralight and highly flexible for gentle lamination on the back of the neck. For optimization of sensor location and signal characterization, a commercial data acquisition system was initially utilized. The systematic integration of lithography-based open-mesh interconnects on a polyimide film, bonding of small chip components, and encapsulation with an elastomeric membrane enables the soft and compliant electronic system. Details of the fabrication methods and processes appear in Figure 46 and 47. The flexible electronic circuit consists of a few different modules that allow for wireless, high-throughput EOG detection.

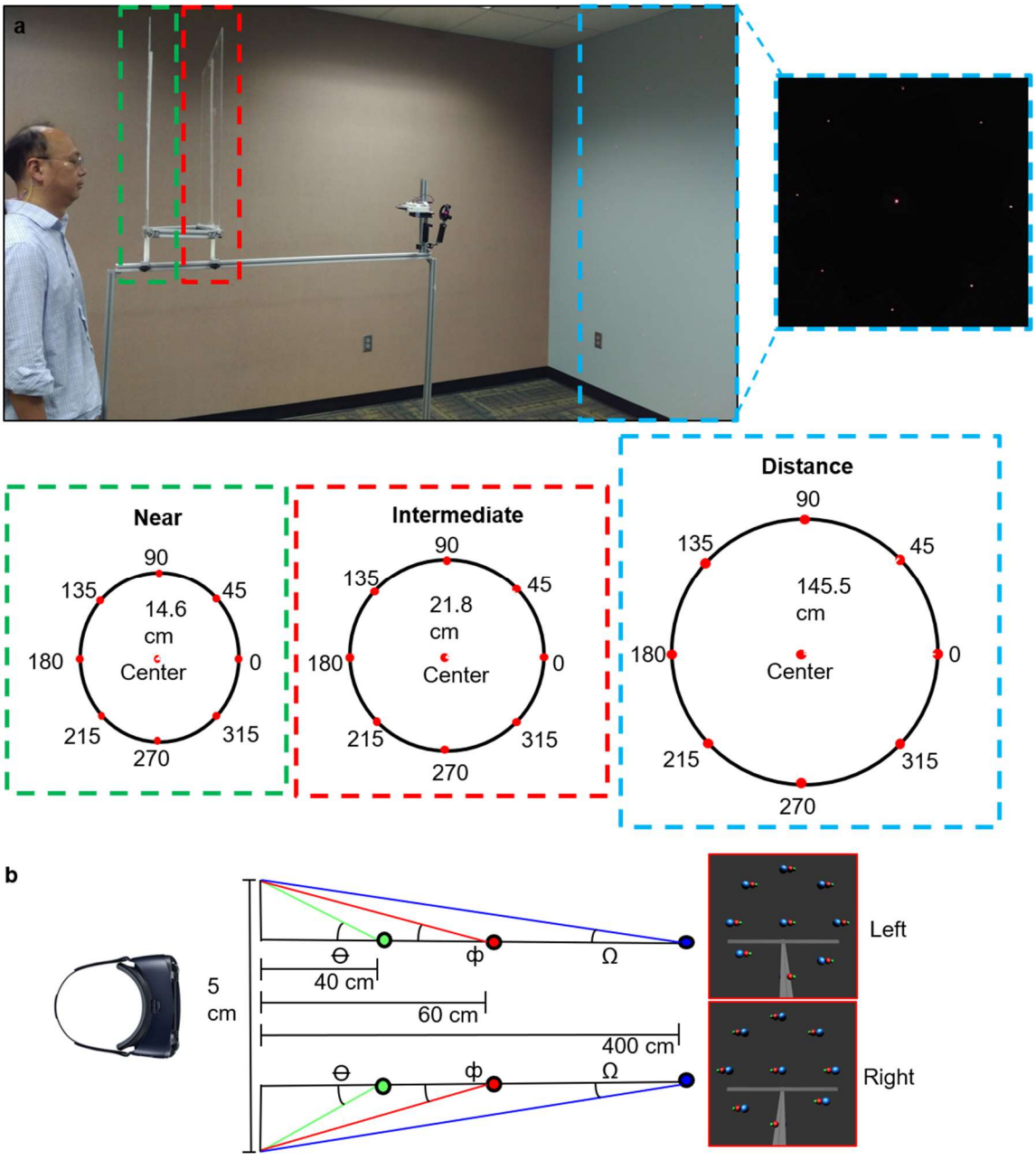

Figure 44. Apparatus for testing eye vergence motions Physical apparatus (top) and Virtual Reality (bot). Dimensions of the (a) physical apparatus consists of positions that approximate to 1º, 2º, and 3º of motion. (b) The VR images are offset for each eye to simulate binocular vision in the real world.

The antenna is a monopole ceramic antenna that is matched with a T-matching circuit to the impedance of the Bluetooth radio (nRF52, Nordic Semiconductor), which is serially connected to 4-channel 24-bit analog-to-digital converter (ADS1299, Texas Instrument)

for high resolution recording of EOG signals (Figure 45b). The bias amplifier is setup for a closed loop gain of the signals. In the electronics, an array of 1 µm-thick and 18 µm-wide interconnects (Figure 45c) ensures high mechanical flexibility by adsorbing applied strain to isolate it from chip components. Experiments of bending in Figure 45d capture the deformable characteristics of the system, even with 180° bending at a small radius of curvature (1 mm to 5 mm).

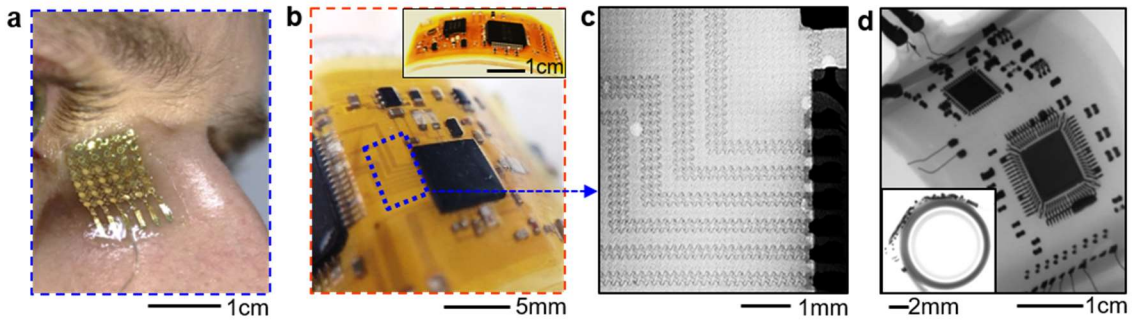

Figure 45. (a) A close up of the skin-electrode conformality and small form factor makes it ideal for contoured regions such as the nose. (b) A rolled up flex device can still continue to function with a bending radius of 13 mm. (c) A section in between the ADC and the Bluetooth radio has been bent with a radius of 1 mm showing low strain; the corresponding experimental test shows the device still functional. (d) Further X-ray images along the 13 mm bending radius shows the IC internals and all the soldered components.

The measured resistance change is less than 1% at the area of bending in between the two largest chips, which means the unit continues to function (Figure 48). In addition, the ultrathin, dry electrode (thickness: 1µm with a backing elastomer) makes an intimate and conformal bonding to the skin (Figure 49a-c) without the use of gel and adhesive due to the reduced bending stiffness [27, 41].

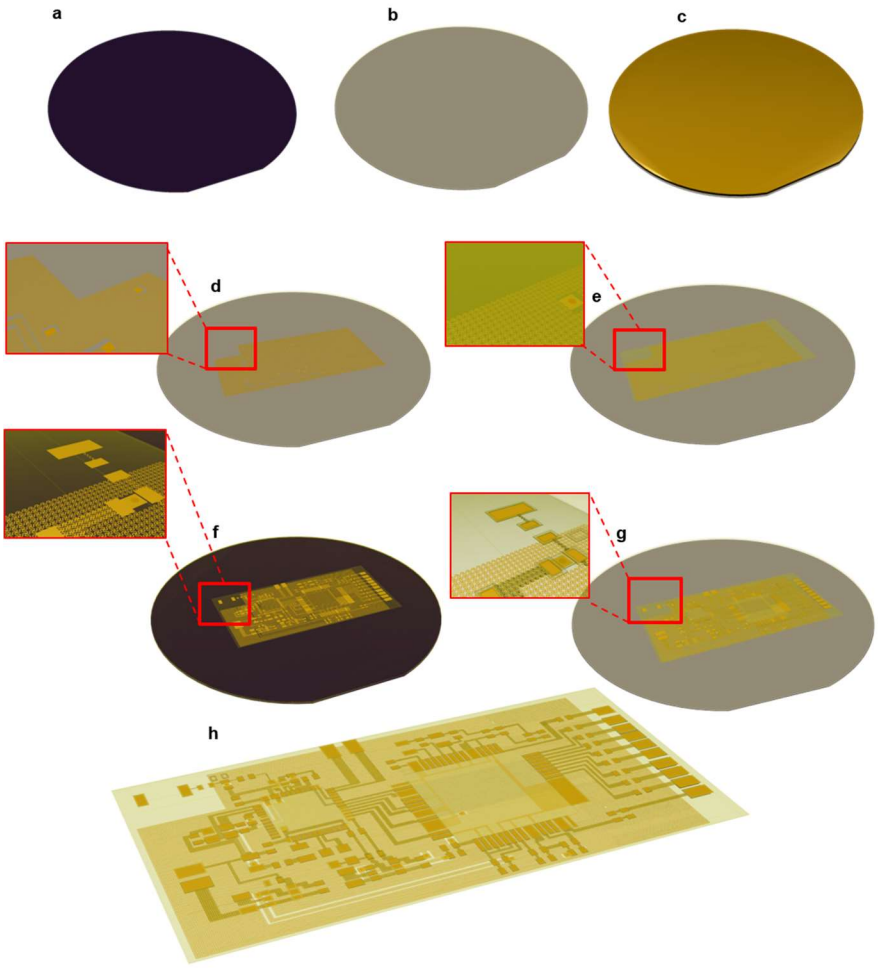

Figure 46. Flex device fabrication process. (a) Flex device fabrication is possible using a clean silicon wafer on which to build (b) a layer of PMMA and polyimide. (c) Sputter copper and then (d) etch the copper with APS-100. (e) Spin cast two layers of polyimide and etch the holes. (f) Deposit copper to fill in holes and create top interconnect layer. (g) Spin cast polyimide and etch away the top layer. (h) Finished design is ready to transfer after removing any copper oxides using stainless steel flux.

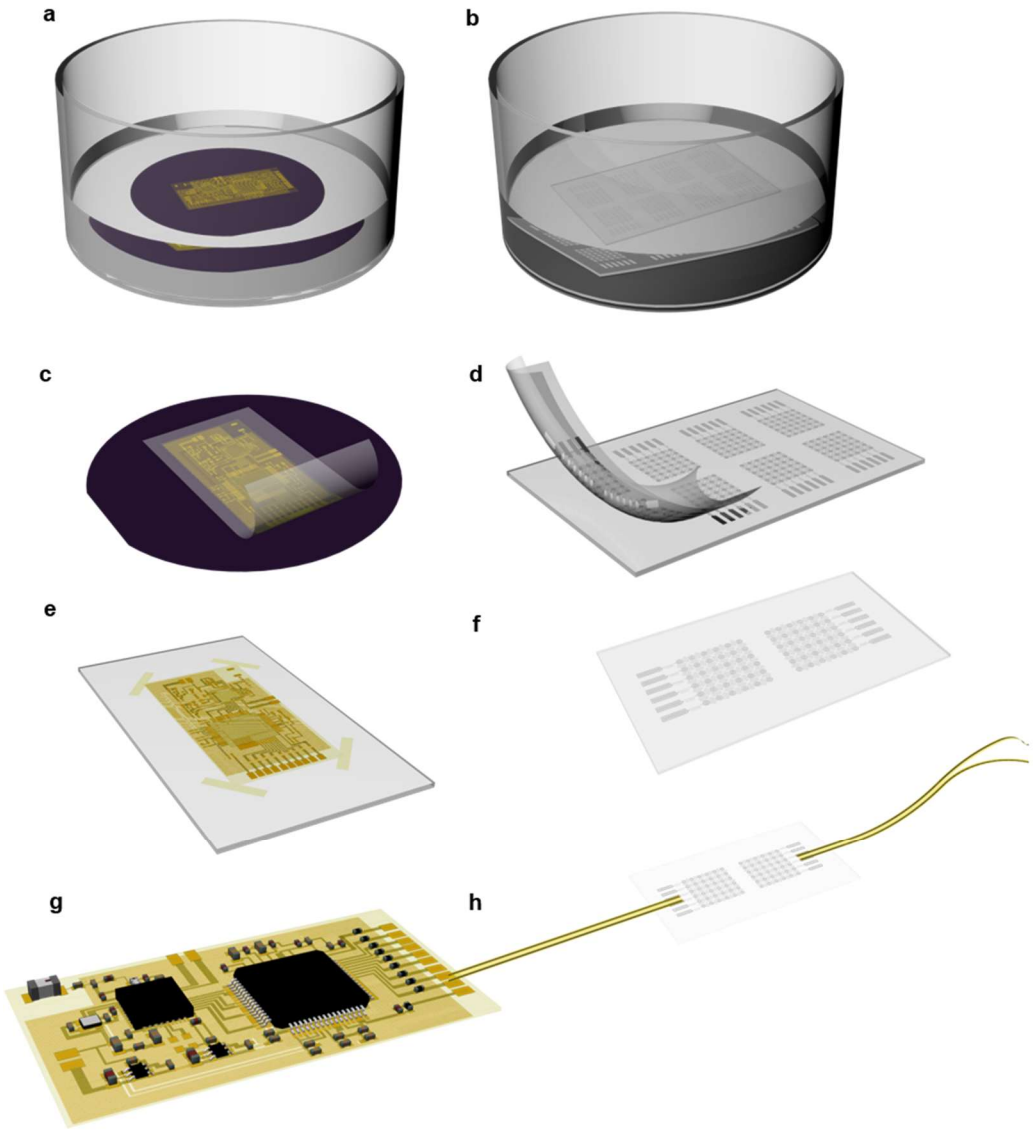

Figure 47. Skin electrode and Flex Device transfer process. (a) Flex device is submerged in a bath of acetone at 60 ºC overnight (b) while the skin-electrode is processed in the acetone bath for 1 hour. (c) Use the water soluble tape to transfer the device off the silicon wafer and (d) skin-electrode off the glass slide. (e) Prepare the ecoflex gel and ecoflex 30 mixture for the device and transfer simultaneously prepare the (f) ecoflex gel sample on PVA for the skin-electrodes. (g) Solder the IC chips onto the thin film flex board and (h) attach ACF wires to the skin-electrodes then configure the device and the skin-electrodes together.

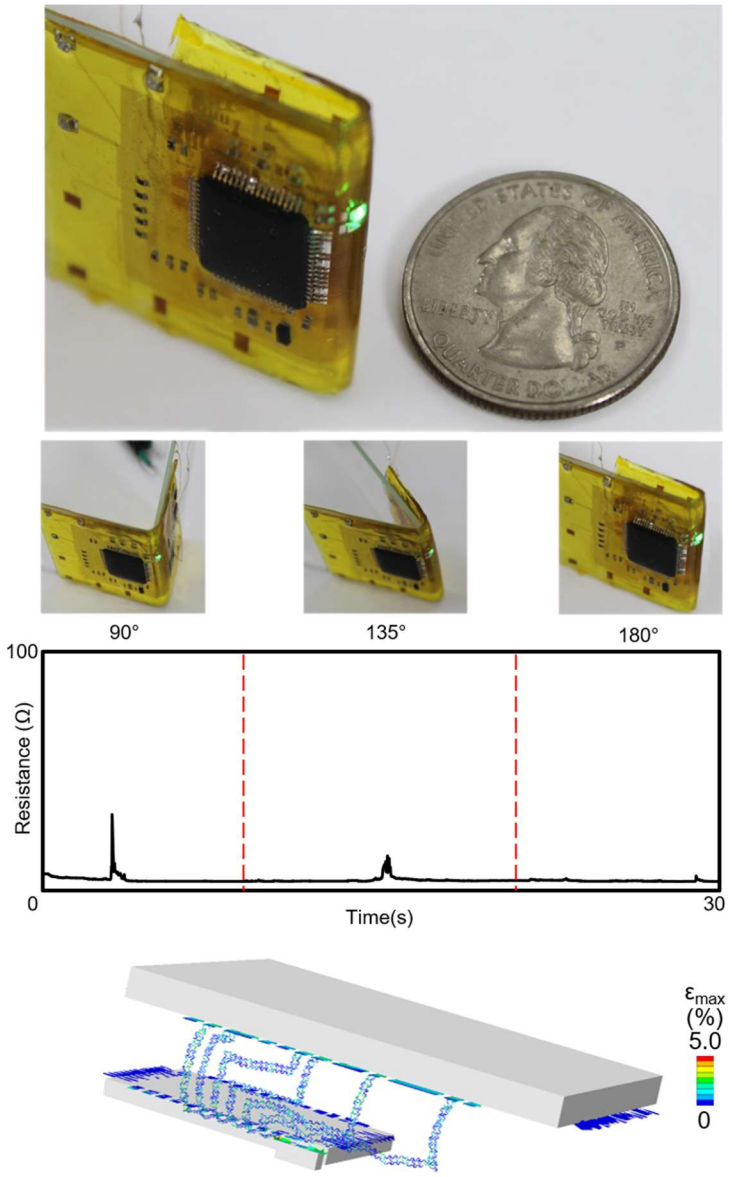

Figure 48. Experimental bending of EOG Device. Device is compared to the American quarter showing the size of the device. Successive bending of the device from 90°- 180° shows minor fluctuations in resistance and continuous operation of the device. Additional simulations indicate low strain near the bending locations.

The open-mesh, serpentine-like structure can even accommodate dynamic skin deformation and surface hairs near eyebrow for sensitive recording of EOG. The newly developed ocular electronic system, in conjunction with a data classification algorithm for eye vergence, aims to diagnose diseases like strabismus that is most commonly described

by the direction of the eye misalignment (Figure 49d-e). With the integration of a VR program, this portable system could offer a home-therapeutic tool to find many applications in eye disorder therapy.

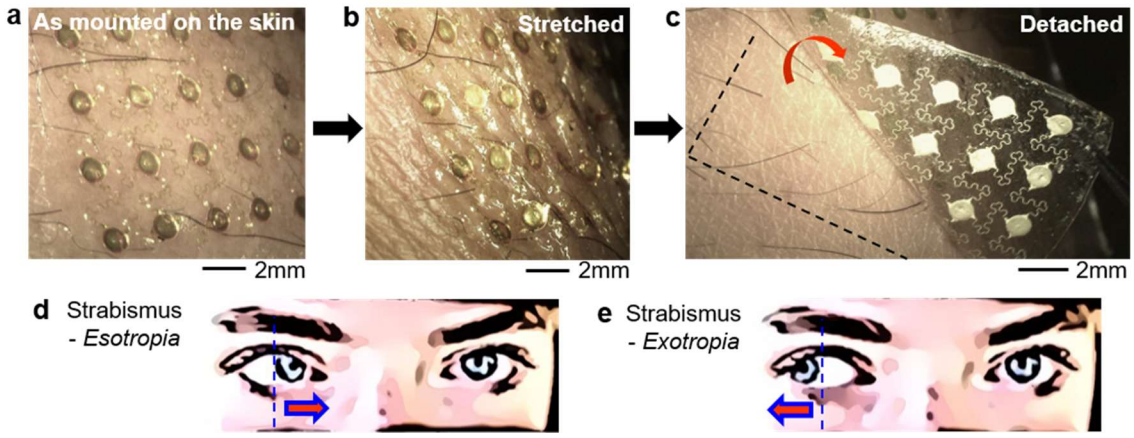

Figure 49. Skin-mounted above eye and disease diagnostic. (a) An unstretched electrode on the skin near the site of the ocular electrode positions. (b) Electrode is stretched to show the 180 degree bending characteristics (c) Removing the electrode still ensure functional electrode. (d) The strabismus diagnosis of esotropia and (e) exotropia can be extracted from a machine learning classification of numerous patients that can also be transmitted directly to a doctor.

1.19 Study of ocular vergence and electrode Positioning

Recording of ocular vergence via EOG requires meticulous optimization to produce the maximum functionalities. We assessed a series of distances with eye vergence to establish a metric for classification. The most common distances that humans observe in daily life was the basis for the procedure in the physical and virtual domain. The discrepancy of the degrees of eye motion is a necessary physical attribute for eye vergence classification. Figure 50 shows the individual converging and diverging ocular motions with the corresponding EOG signals.

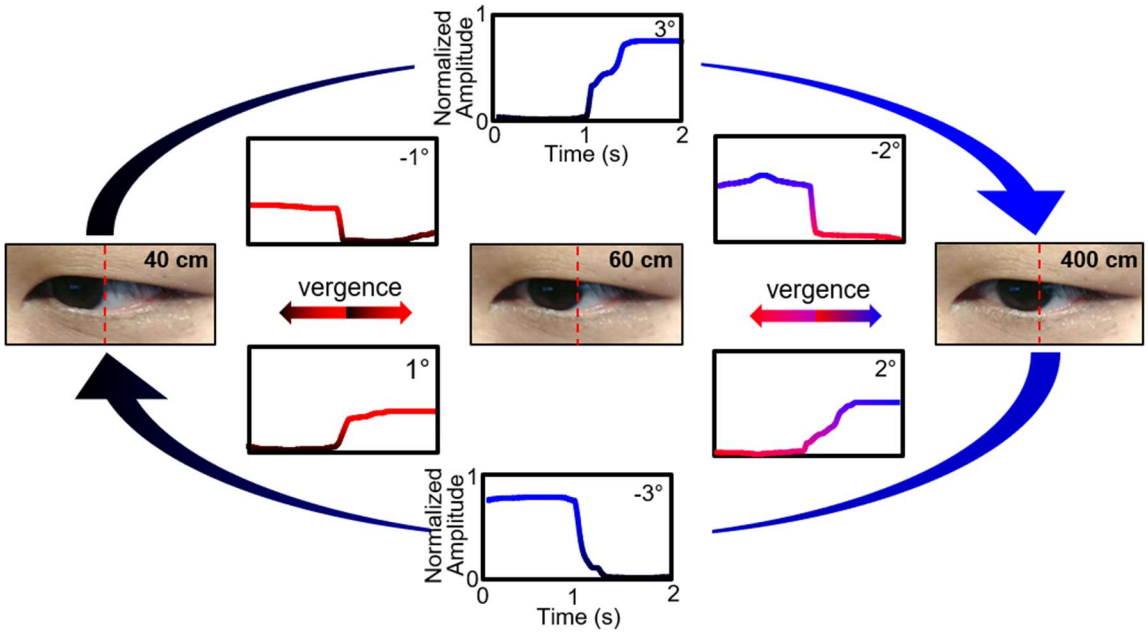

Figure 50. Eye vergence signals. (a) Forwards and backwards motion of the eye resemble eye vergence for 1° – 3° of motion. These signals are normalized from 0 to 1 for better clarity.

An example of diverging motions, from 40 cm to 60 cm and 400 cm, corresponds to positive potentials as the degree of eye vergence increases from 1° to 3° based of an interpupillary distance of 50 mm. Converging movements show an inverted potential in the negative direction, from 400 cm to 60 cm and 40 cm, corresponding from 3° to 1°. Conventional EOG sensor positioning aims to record synchronized eye motions with a large range of potentials in observing gaze tracking[74, 75]. An experimental setup in Figure 51a resembles the conventional setting (2 recording channels and one ground on the forehead) for typical vertical and horizontal movements of eyes. A subject wearing the soft sensors was asked to look at three objects, located 40 cm, 60 cm, and 400 cm away. The measured classification accuracy of eye vergence signals shows only 34% (Figure 51b) due to the combination of inconsistent potentials and opposing gaze motions. In order to preserve the signal quality of ocular vergence, we used three individual channels using a

unipolar setup with a combined reference electrode positioned on the contour of the nose (ocular vergence 1; Figure 51c), which results in the accuracy of 87% (Figure 51d). Lastly, we assessed the accuracy of our electrode positioning by adding two more electrodes (ocular vergence 2; Figure 51e), which yielded 91% accuracy (Figure 51f) with the least amount of deviation in the signals. The classification accuracy per each sensor location is the averaged value from 3 human subjects.

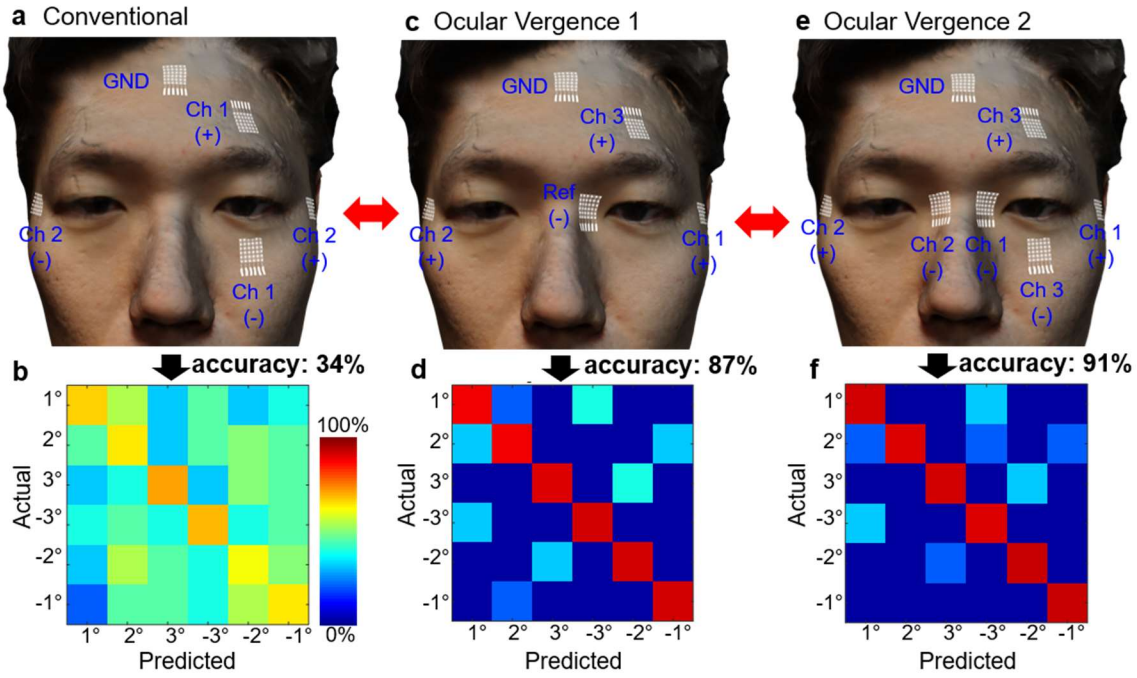

Figure 51. Electrode positioning with corresponding classification results. (a) Conventional EOG positioning based off synchronized eye movement demonstrates (b) low classification accuracy. (c) Ocular vergence 1 positioning with similar number of electrodes as conventional demonstrates much (d) higher classification accuracy. (e) Ocular vergence 2 (f) enhances classification accuracy with individual reference electrodes for each eye.

Additionally, the recording setup with the case of ocular vergence 2 (Figure 3e-f) shows signal resolution as high as ~26 μV/degree, which is a higher that of the prior work[72]

described in chapter 3 with ~11 μV/degree. This increased sensitivity of vergence amplitude is due to a better positioning of the electrodes closer to the eyes, on the nose, and the outer canthus. In addition to ocular vergence 2 resolution, the wireless wearable circuit has an increased gain of 12 in the internal amplifiers which results in higher amplitudes.

1.20 Eye vergence optimization with signal processing and feature selection

I assessed the variability of ocular vergence motions in both physical and VR domains to realize a fully portable vergence therapeutic program. The acquired EOG signals from vergence motions require a mathematical translation using statistical analysis for quantitative signal comparison (Figure 52). Prior to algorithm implementation, raw EOG signals (top graph in Figure 52a) from the ocular electronics are converted to the derivative data (bottom graph in Figure 52a). Due to the noise and baseline drift, a 3^{rd} order Butterworth bandpass filter is implemented from 0.1 Hz to 10 Hz. The bandpass filter removes the drift and high frequency noise so the derivative is much cleaner as shown in Figure 52b, according to the vergence motions. Data set shows that blink velocity is faster than vergence motions which corrupts thresholding. A 500-point median filter can remove any presence of the blink as shown in Figure 52c. However, stronger blinking from certain subjects still remain, which is removed by thresholding an amplified derivative signal. Increasing the 2^{nd} order derivative filter to 6^{th} order can assist in positively altering the range of thresholds by changing the signal to noise ratio (Figure 52d). The final step is to parse the data into a sliding window, compute features, and input it into the classifier. A decision boundary of two dimensions of the feature set with the ensemble classifier is shown in Figure 52e. A wrapper feature selection algorithm was applied to determine if

the utilization of 10 features was optimized for the recorded EOG signals. In addition to five features (definite integral, amplitude, velocity, signal mean, and wavelet energy) form our prior study[72], we studied other features that can be easily converted into C programming using a MATLAB coder.

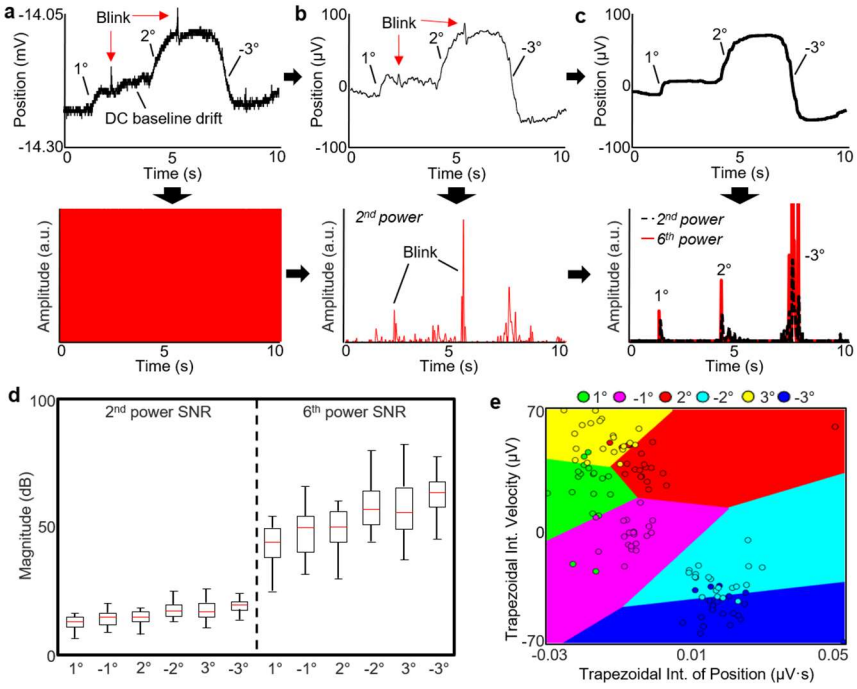

Figure 52. Data preprocessing to feature extraction: (a) Raw signal is acquired real-time via Bluetooth data acquisition unit and its corresponding derivative is shown. (b) The data is preprocessed with a bandpass Butterworth 0 phase filter with the corresponding derivative of that data raised to the second power. (c) The filtered data is further processed with a 500 point median filter and the corresponding derivative is raised to the 6^{th} power. A coefficient is multiplied to increase the amplitude of the 2^{nd} order and 6^{th} order differential filter. (d) A comparison of the 6^{th} order and 2^{nd} order differential filter shows an increased range of the 6^{th} order data by calculating the signal to noise ratio. The 6^{th} order data is used for thresholding the signal for real-time classification of the dataset. (e) The data from the sliding window is inputted into the ensemble subspace classifier which is shown by the decision boundaries of two dimensions of the feature set.

The first feature (Eq. 1) shows cumulative trapezoidal method in which the filtered signal f(t) is summed upon each unit step, i to i +1, using the trapezoidal method for quick computation. The next feature (Eq. 2) is the variance of the filtered signal. A root mean

square is utilized (Eq. 3), in conjunction with peak to root mean square ratio (Eq. 4). The final feature is a ratio of the maximum over the minimum of the filtered window (Eq. 5).

$$Ctrapz = \sum_{i=1}^{1000} \int_{i}^{i+1} f_i(t)\, dt \tag{13}$$

$$V = \frac{1}{1000-1} \sum_{i=1}^{1000} |f(t) - \mu|^2 \tag{14}$$

$$RMS = \sqrt{\frac{1}{1000} \sum_{i=1}^{1000} |f_i\,(t)|^2} \tag{15}$$

$$Peak2RMS = \frac{|\max(f(t))|}{RMS} \tag{16}$$

$$Peak2Peak = \frac{|\max(f(t))|}{|\min(f(t))|} \tag{17}$$

The rationalization of the use of the ensemble classifier is supported by the MATLAB's classification learner application. This application assesses numerous classifiers by applying k-fold cross validation using the aforementioned features and additional sixty features. The datasets from our *in vivo* test subjects indicated a couple classifiers, quadratic support vector machine and ensemble subspace discriminant were consistently more accurate than others. The latter is consistently higher in accuracy with various test subjects in cross validation assessments. The ensemble classifier utilizes a random subspace with discriminant classification rather than nearest neighbor. Unlike the other ensemble classifiers, random subspace does not use decision trees. The discriminant classification combines the best of the feature set and discriminant classifiers while removing the weak decision trees to yield its high accuracy. A custom feature selection script with the ideas of wrapper and embedded methods was conducted by incorporating the ensemble classifier.

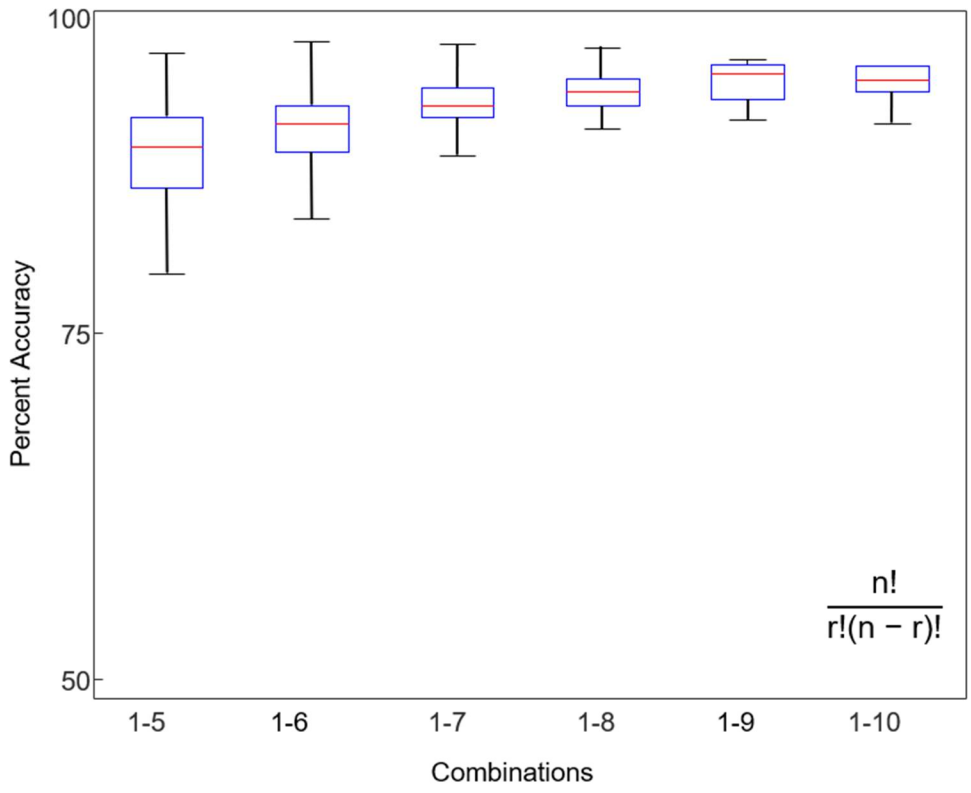

Figure 53. Percent of accuracy with permutations of features from all three channels for position and velocity.

The result of the wrapper feature selection indicates a saturation of the accuracy with a mean accuracy of 95% (Figure 53). Therefore, all ten features were used in the classification methods with a sliding window of 2 seconds. In order to achieve the highest accuracies for real-time and cross validation, the classification algorithm requires the test subject to follow protocols evoking a response of eye vergence in two directions. The test subject followed a repeated procedure from motion to blink, motion, and blink. This procedure allows the data to be segmented into its specific class for facile training with the classifier by following direction 1 and direction 2 four times each (Figure 54). The integration of the training procedure with filters, thresholds, and the ensemble classifier enables our high classification accuracies.

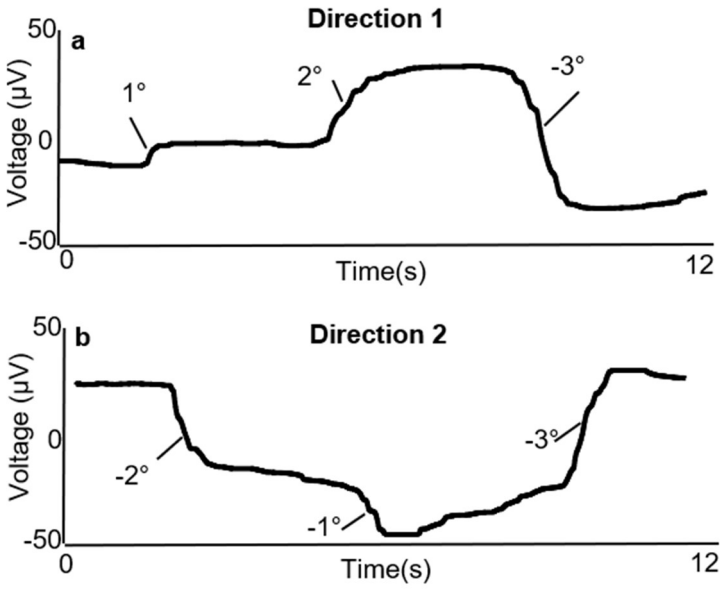

Figure 54. Training and testing direction for eye vergence. The procedure for recording and training eye vergence involves following a linear procedure to extract all eye motions equal number of times. (a) Direction 1 and (b) direction 2 are repeated four times.

1.21 Comparison of ocular classification accuracy between virtual reality and physical apparatus

This work summarizes the experimental results of ocular classification comparison between the soft ocular electronics with a VR headset (Figure 43a) and a conventional device with a physical target apparatus (Figure 44a). I analyzed and compared only the center position data among the circular targets (Figure 43b) because this resembles the most accurate vergence motions without any noise from gaze motions. I transferred our physical apparatus to the virtual domain by converting flat display screen images to fit the human binocular vision. The VR headset enables the capture of ideal eye vergence motions because head motions are disabled and the stimulus is perfectly aligned with the user's binocular vision. This is evident from the averaged signal and standard deviation of the

normalized position of the ideal datasets shown in Figure 55a-55b (red line: average and grey shadow: deviation).

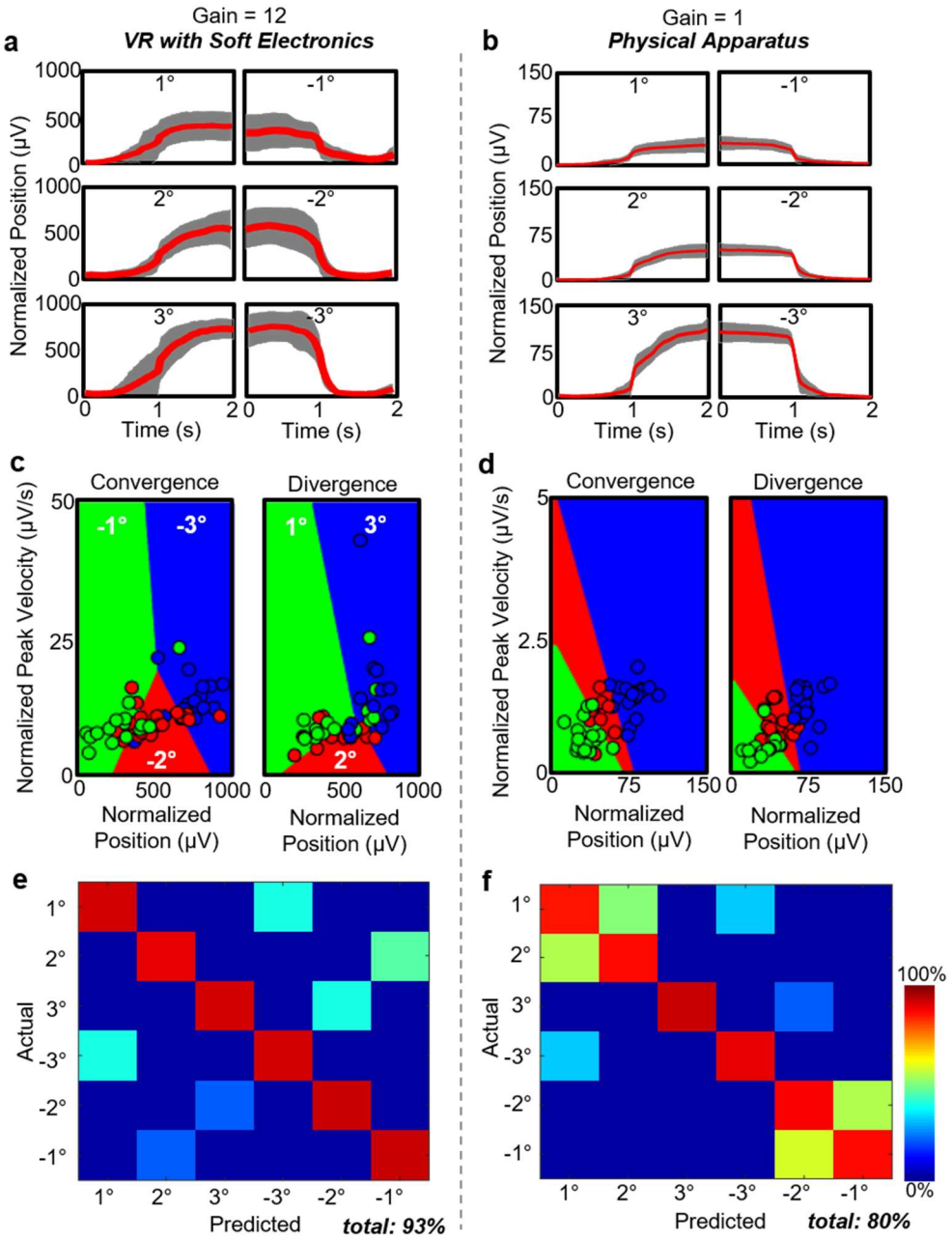

Figure 55. Eye vergence normalized amplitudes and peak velocity for classification results: (a) The normalized signal set with mean and deviation for flex device with subject 11 in VR apparatus and subject 9 with physical device. (b) Peak velocity comparison to normalized amplitude for the ideal case of eye vergence. (c) Cross validation results of

subject 11 with flex device in the VR apparatus and subjects 6-10 with the physical apparatus.

The physical apparatus data shows a larger variation in overall trials in comparison to the VR headset as observed in Figures 56 and 57.

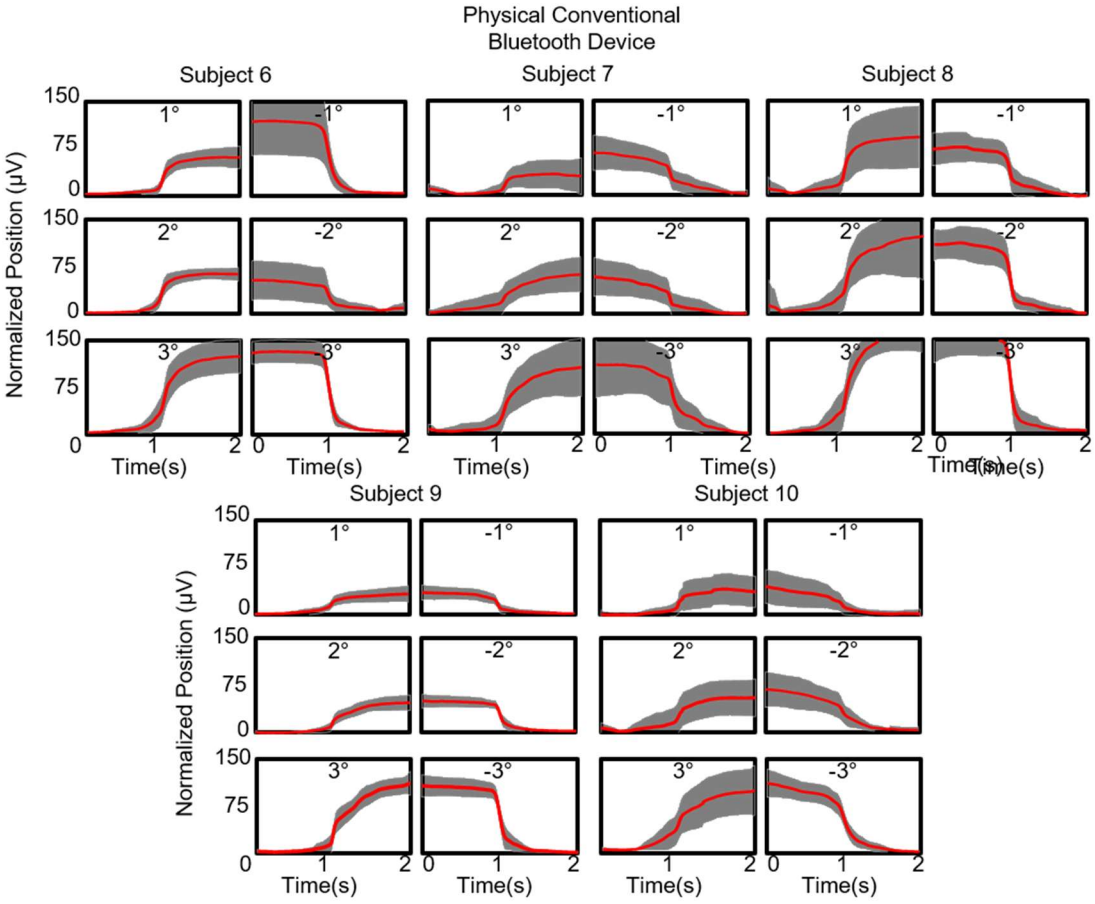

Figure 56. Normalized eye vergence motions recorded with subjects 6-10 using the physical apparatus. The normalized signals for each user for all vergence motions indicate high variability with signal collection with physical apparatus.

This is a consequence of the test apparatus with each user's variability in observation of the physical apparatus. We also compared the normalized peak velocities according to the normalized positions for both convergence and divergence in Figure 55c-d. The summarized comparison of classification accuracy based on cross validation with the VR-

equipped soft ocular electronics shows higher value (93%) than that with the physical apparatus (80%), as shown in Figure 55e-f. The intrinsic quality of the ensemble classifier we utilized shows high variance in cross validation assessments. Even with the real-time classification, the ensemble classifier yields about 83% and 80% for the VR environment and the physical apparatus, respectively. The VR real-time classification is higher than the physical apparatus due to less variation between opposing motions of positive and negative changes.

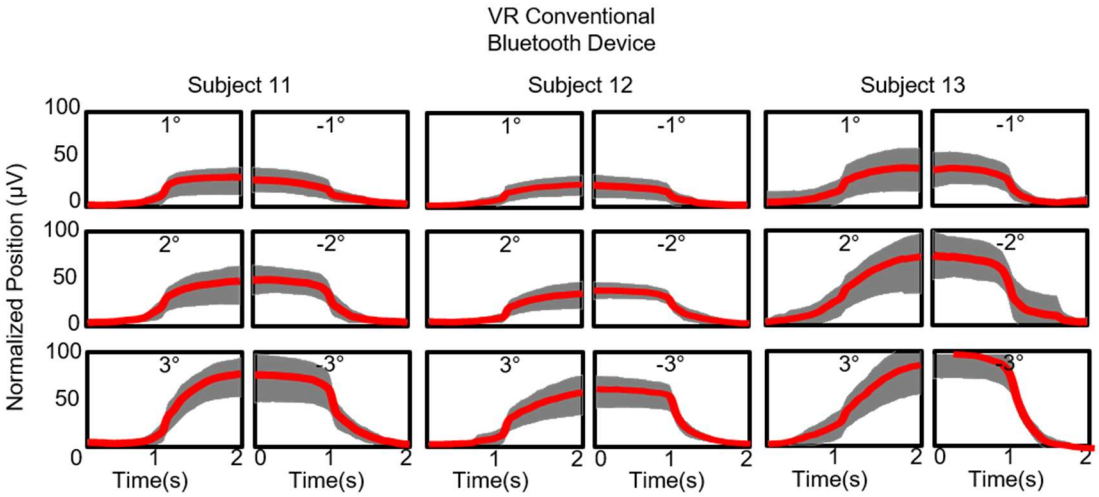

Figure 57. Normalized eye vergence motions recorded with subjects 11-13 using the virtual apparatus. The normalized signals for each user for all vergence motions indicate more precise responses in the VR display.

1.22 VR-enabled vergence therapeutic system

As the gold standard method, conventional home-based vergence therapy utilizes pencil pushups in conjunction with office based visual therapy[76]. Adding a VR headset to home based therapy with a portable data recording system can certainly make a patient use the same therapeutic program both at an optometrists office and home. To integrate with the developed ocular electronics, we designed two ocular therapy programs in a Unity

(https://unity3d.com/) engine (to work with the Samsung Gear VR Headset (https://www.samsung.com/global/galaxy/gear-vr/)). The first program enables a patient to use the virtual 'Brock String' (Figure 58a) which is string of 100 cm in length with three beads, originally designed to treat patients with strabismus[30]. The string is offset 2 cm below the eye and centered between the eyes with the three beads at varying distances. Three channels of soft sensors on the face (Figure 51e) measure EOG signals, corresponding to a subject's eye movements targeting on three beads (Figure 58a). The second therapy program uses a set of two cards with concentric circles on each card referred to as 'Eccentric Circle' (Figure 58b), which is also widely used program in vergence therapy[30]. The corresponding EOG signals show the user, wearing the VR headset, cross his eyes to yield the center card. The distance between the left and right card can be increased to make this task more difficult. The signal also demonstrates the difficulty of the eye crossing motion due to the lower velocity. These programs can be used as an addition to the office therapy of the CI treatment procedures. Continuous use of the VR headset program (Figure 58c) presents improved eye vergence, acquired from three human subjects with no strabismus issues from near point convergence. Users indicate the difficulty of converging in earlier tests (accuracy: ~75%), which improves over time (final accuracy: ~90%). In addition, we found a subject who had difficulty holding the near point convergence motions in the VR headset which was determined to be strabismus exotropia (Figure 58d). This subject was also asked to perform pencil pushups from 3 cm up to 60 cm in the physical domain (Figure 58d). The corresponding EOG signals upon convergence and divergence during the pencil pushups appear in Figure 58e. While the right eye signals ('blue' line) show the correct divergence and convergence positions, his left eye shows

slower response at convergence, followed by an exotropic incidence after the blink at the near position. Typically, a blink results in high velocity increase and decrease of potentials, but in this case the potential does not decrease after the blink moment. A divergence motion should increase the EOG potential (as the right eye), but the signal drops 100 µV, meaning that the left eye moved outwards.

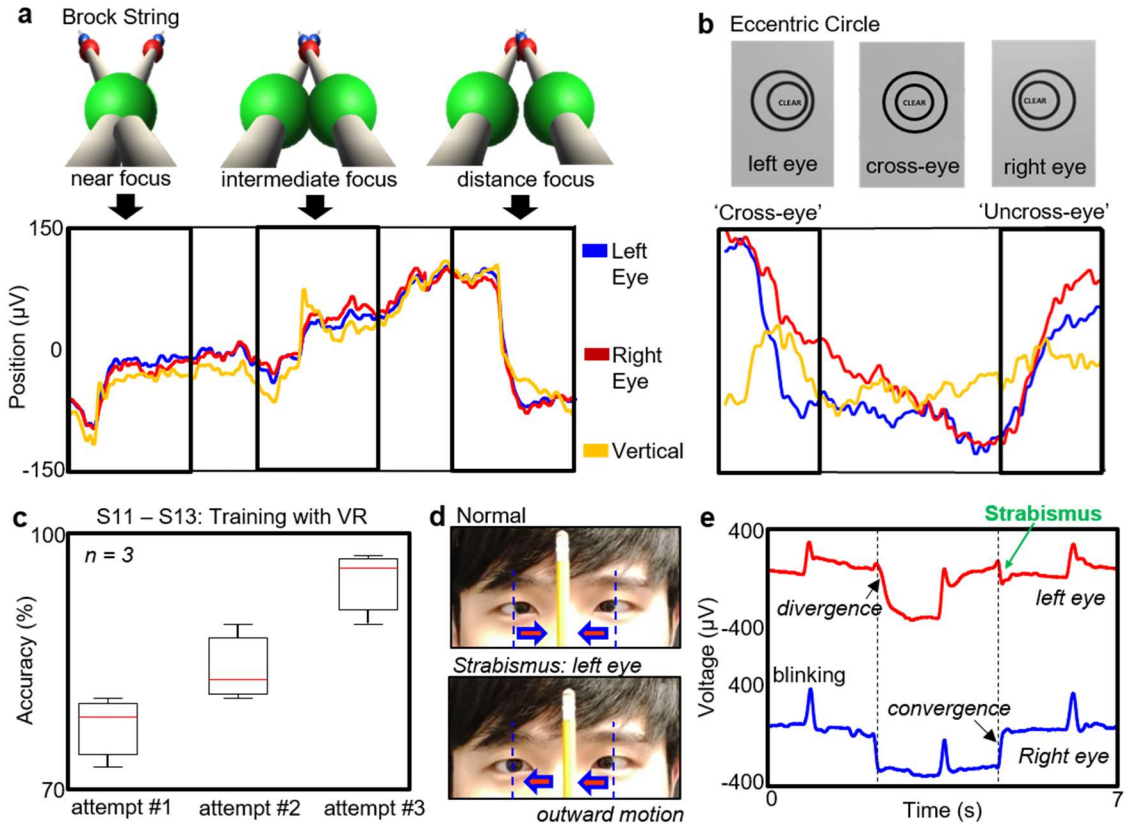

Figure 58. Therapeutic programs with corresponding signals and VR Rehabilitation. (a) Brock string program enables customizability of bead distance without the need of a physical object; the corresponding signal pin points the position of the user's vergence motion. (b) Eccentric circle program replaces conventional stereogram activities with customizability of the card distance. The user can practice crossing eyes at different distances to evoke the "third card" in the center. (c) Successive use of our VR program shows preliminary results of increasing accuracy using OV2 electrode positioning. (d) The same electrode positioning can assist in detecting strabismus conditions while using pencil pushups. (e) Pencil pushups evoke a strabismus response in the right eye.

1.23 Summary

Ultimately this work involving eye vergence therapeutics is the first of its kind using electrooculograms and machine learning classification. Eye vergence applications are severely limited as gaze tracking has been the focus of most EOG and VOG studies. However, as more people are facing strabismus, vergence, and neurological issues, optometrists are seeing stronger efficacies of office therapy. This work aims to supplement office vision therapy with home vision therapy protocols, programs, and classification results to accurately quantify these datasets. Table 7 shows this works novelty in comparison to others.

Table 7. Review of eye vergence studies in comparison to this work.

Name	Resolution	Device	Sensor	Type	Application	Classification	Fabrication	Stimulus
This work	1°	Flex Circuit	Skin-electrode	EOG	Eye Vergence Therapeutics	Ensemble subspace discriminant	Aerosol Jet Printing and Photolithography	Virtual Reality and Physical Apparatus
[77]	0.2°	N/A	Ag/AgCl Electrodes	EOG	N/A	N/A	N/A	Stereo, physical, and head mount
[36]	0.25°	Mobile Eye Brain Tracker	Camera	VOG	Binocular coordination and vergence capabilities	N/A	N/A	Stereo displays of text
[78]	0.25°	Mobile Eye Brain Tracker	Camera	VOG	Binocular coordination with strabismus conditions	N/A	N/A	Stereo displays of text
[31]	N/A	Infrared Camera	Infrared Camera	VOG	Vergence disparity in binocularly health people	Vergence Analyses and feature extraction	N/A	Stereo display

RADIO FREQUENCY IDENTIFICATION OF SALIVARY ELECTROLYTES

RFID is an established inventory tracking method via passive or active methods. Most systems consist of a small battery for increasing sensitivity of the chipset to an external reader. Passive mode is used in this work to prove the functionality of an RFID tag for sensor measurements without a battery using a portable reader. A reader provides power to a receiver tag which stores enough energy to radiate information back to the reader. Ultra-High Frequency (UHF) RFID tags have a centered resonance around 915 MHz. The communication protocols that will be discussed for my application involves UHF ISO 18000 Generation-2 using an android and windows reader.

Commercially available RFID transponder chipsets are used for configuring sensors using the UHF gen 2 protocol. I decided to use the only chip (AMS SL900a) available for sensor configuration and data acquisition. Most other tags have sensor capabilities for temperature, pressure, or humidity, but lack the versatility of other sensors that users may desire. I decided to use this IC for the measurement of linear resistance on the human body. Few RFID tags have shown their performance on the human body. No other publication has described the use of UHF technology in passive mode on skin for sensor measurements.

In this work I will describe the use of a linear resistance configuration for the passive recordings of galvanic skin resonance (GSR). GSR is also referred to as

electrodermal activity and it is used to measure the DC resistance of the skin. The resistance values are lowest on the fingers, forehead, and on the soles of the toes. This is because of the density of sweat glands at these locations which are higher than anywhere else on the body. Additionally, there is a low frequency response from the brain as a person becomes aroused, stressed, or relaxed. This is due to a subtle change from the sympathetic to the parasympathetic nervous system. In the section I will lay down the ground work on how to make this feasible on the human body.

1.24 UHF-RFID Tag Fabrication and Programming

Ultra-high frequency RFID signals use RF to power the tags which can be very similar to energy harvesting techniques. The read range corresponds to the stability of this method but can be highly variable. This is because of the sensitivity of the chip and the EIRP of the readers. It is not always true, but the higher the reader's EIRP the further the read distance. The readers used in this work involves the AS3933 development board meant for development in Visual Studio and the U Grok it reader that runs on the android platform. Both these readers were used for reading from the tag and show significantly differing results due to variability in orientation of reader antenna, reader antenna's electric field due to geometrical factors, and the power output of the readers.

The read range of the AS3993 with the passive mode of the Sl900a IC in air is limited by directionality in the 3-D space. However, the range is anywhere from a few cm to half a meter. The alternative U grok it reader transfers data through the aux port of a smartphone to display real-time results on the developed API. This reader has a maximum EIRP of 30 dbm, however the API loops through 22 to 30 dBm until the best

signal strength is achieved with the tag. With the use of the android based reader, our tag can achieve anywhere from a few centimeters on skin to over a meter in air.

The current design for tag is based off the development board design for a folded dipole antenna with a matching inductor at 39 nH. In order to prevent additional tuning of the tag, a thick elastomer (~1 mm) was placed underneath the antenna. I fabricated the antenna, chip, and sensor using aerosol jet printing.

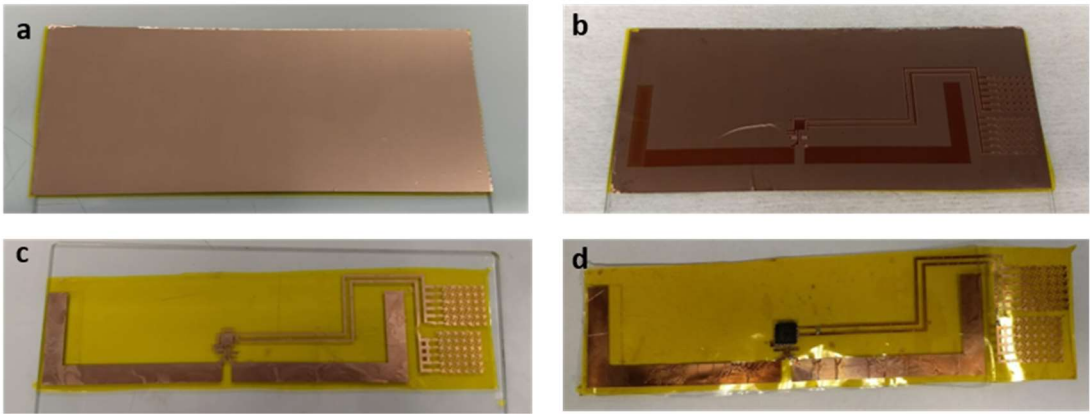

Figure 59. Aerosol jet printed fabrication process using unconventional lithography. (a) A 3 micron copper sheet is laminated onto Kapton tape. (b) Photoresist is deposited onto the substrate and (c) the copper is etched. (d) Soldering takes place after placing the substrate onto an elastomer layer.

First, double sided Kapton tape was adhered to a glass slide with atleast 125 mm in length. Next, a 3 μm copper foil was laminated to the Kapton tape and then plasma treated for 1 minute. Contradictory to the AJP's purpose of strictly additive fabrication, it was used to deposit photoresist as a mask for wet etching. The SC1813 photoresist is developed by Shipley to be 70% solvent and 30% polymer resins. The solvent level was increased to 95% at which point it was inviscid enough to be then atomized in the ultrasonic atomizer. The photoresist was deposited at various sheath flow rates, atomizer flow rate of 20 sccm, and a platen speed of 10 mm/s for high throughput fabrication.

Since the platen is heated to 80 ºC, there was no need for a photoresist curing step. Aluminum etchant type A was heated to 50 ºC for faster etching of the copper film. After etching and rinsing with DI water, the circuit was treated in diluted stainless steel flux to remove oxide layers. The circuit was then placed onto elastomer and the chips were soldered on using a reflow profile for silver solder paste. **Figure 59** shows the subtractive method of fabrication using unconventional lithography processing

1.25 *In vitro* and *In vivo* methods and measurements of sodium

Recording on the fingers is very easy, however I need to record on a location of the human body that invokes a response and can maintain the shape of the tag without excessive bending. This limitation is due to the changes in capacitive and inductive response of the antenna. For this reason, the wrist was chosen because it exhibited GSR and the antenna did not exhibit excessive bending. The results of the *in vitro*

measurements using a digital multimeter are shown in **Figure 60** where the sensor response is in the kOhms on the fingers and MOhms on the wrist.

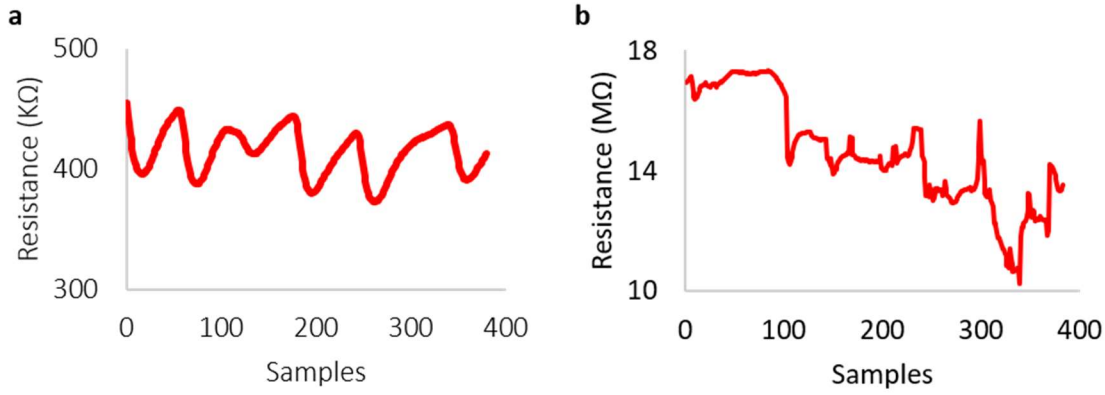

Figure 60. Digital multimeter results. (a) DMM results on the fingers show lower resistance while the (b) wrist location shows higher noise, resistance, and lower sensitivity.

It can be concluded that the sensitivity is much lower at the wrist due to the decreased sweat glands and increased resistance. Slow, deep breaths were inhaled and exhaled over a 5 second period to invoke the resistance response. Recording with amplifiers, and ADCs that are high resolution and high gain makes GSR recordings easy. However, recording from the UHF IC has one major drawback. The range of resistance readings with the sensor front end is a maximum of 4.9 MOhms using the EXT1 and VSS inputs. In order to lower the effective resistance, a load resistor was added in parallel with the electrodes so the effective resistance was dropped from 10 - 18 MOhms to 1 - 4 MOhms range using a parallel resistor (**Figure 61a)**. Additionally, the sensitivity can be tuned based off the load resistor, which is almost 3x higher when a load resistor at ~4 MOhms is used instead of 1 MOhm (**Figure 61b)**.

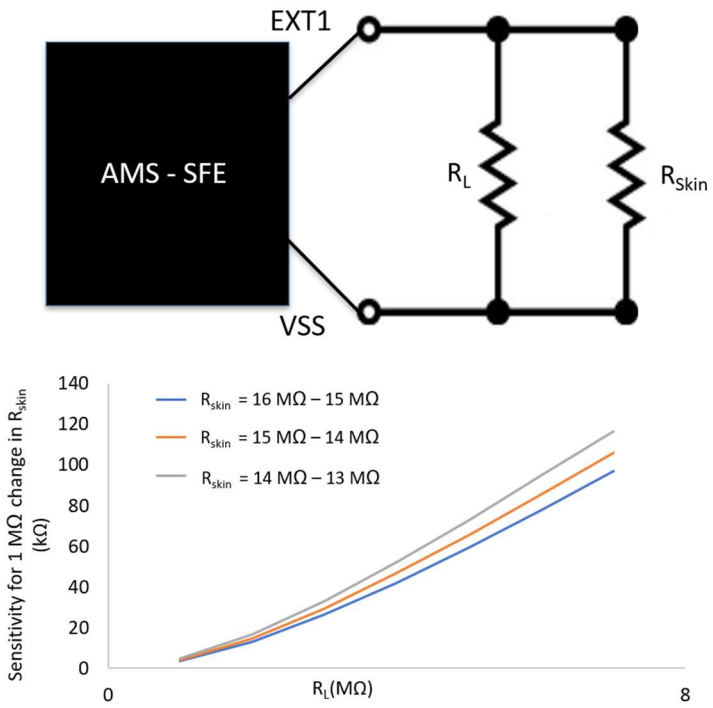

Figure 61. Sensor configuration for AMS. (a) Sensor front end configuration on the AMS to be able to read GSR directly from the skin. (b) Sensitivity of the sensor for change in skin resistance of 1 MΩ for load resistors from 1 MΩ - 8 MΩ

The final tag design with sensor recordings from direct interfacing on the skin is shown in top and bottom view of the tag. The sensor contacts the edge of the wrist at the location where most veins are located. This creates a low resistance and more sensitive response. A comparison between DMM and tag recordings after normalization is shown (Figure 62).

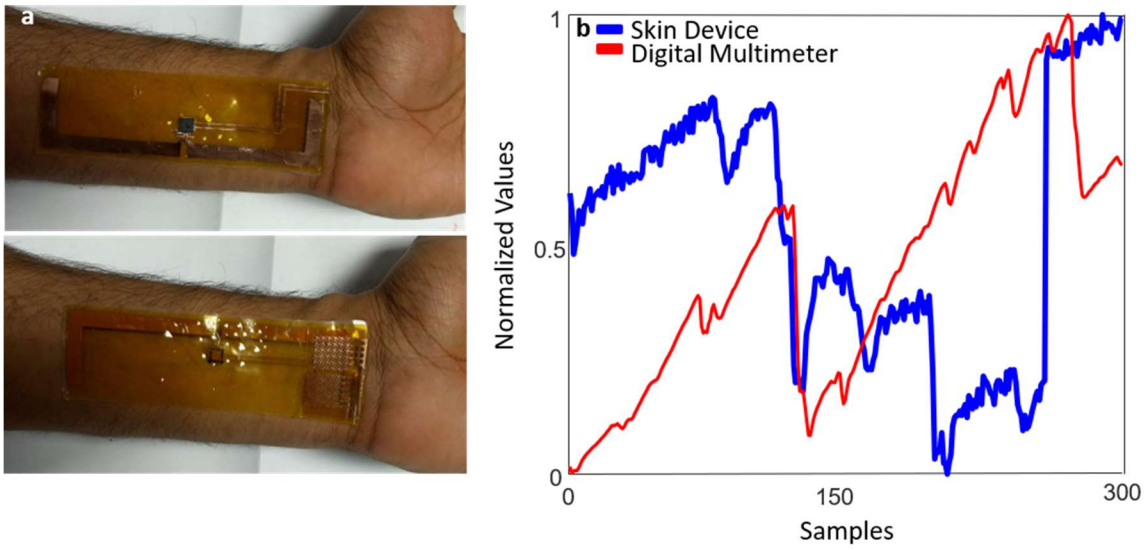

Figure 62. **Sensor recording on the skin.** (a) Top and bottom view of the tag on the skin shows the sensor in contact with the skin and the tag pointed up. (b) Data comparison between DMM and skin tag for GSR recordings.

1.26 Summary

The first passive skin electronic UHF-RFID integrative system for sensor recordings on the human body is shown here. Table 8 shows the novelties of this work over others as well as the limitations. The major limitation is the IC sensitivity which is due to the passive system and the sensor front end of the die. Because of the portability of the reader, a high powered system is not possible, therefore the maximum read distance in comparison to other works is not apples to apples due to differing readers and reader antennas that have been utilized. Increasing the power of the reader could result in a much further read range.

Table 8. Review of RFID data acquisition with various sensing mechanisms and materials.

Name	**RFID Type**	**Tag Vendor**	**Reader Power**	**Sensor Type**	**Application**	**Reading Distance**	**Sensor Materials**
This work	RFID – UHF	AMS Sl900a	1 W	Linear Resistance	Epidermal	3 cm to 1 m	Copper
[79]	RFID – NFC	N/A	N/A	Uric Acid – Amperometric	Wound monitoring	N/A	Ag/AgCl Prussian Blue Carbon Ink
[80]	RFID – UHF	IMPINJ Monza X-8K Dura	4 W	Chlorine Ions- Potentiometric	Cl^- concentration in concrete	1.5 m to 16 m	Ag/AgCl Pt
[81]	RFID – UHF	IMPINJ Monza X-2K Dura	1 W	ECG Sensor	ECG Recordings with simulator	14 feet	Simulator
[82]	RFID – NFC	MLX90129	500 mW	Sodium Ions – Potentiometric	Sodium analyte in sweat	N/A	Ag/AgCl Pd

FUTURE WORK

1.27 Summary and original contribution

The state of flexible electronics is in turbulence, with many research groups pursuing innovative and successful execution of ideas. However, the industry is slow to respond to these methods because of process and material reliability. Photolithography makes flexible electronics possible for manufacturing because of its versatility, but it is wasteful and expensive. Inkjet printing sought to reduce waste and costs, but it has limitations to its applications. Characteristics of various inks from viscosity to surface tension limit the versatility that photolithography provides. This is where aerosol jet printing steps in to improve the current processes by increasing process efficiency and inherently having versatility in ink formulation and print outputs. The resolution of traces can be fine-tuned to 10 μm widths, and as low as 200 nm in this study. In the future circuit printing and soldering needs to be assessed in detail.

This thesis contributes in a few different aspects to a broad and diverse reader set. Engineers, scientists, and clinicians can benefit from understanding each aspect of this thesis from the materials characterization, processing methodology, machine learning and algorithm development, to the ultimate testing of a full set of devices on participants. This iterative process of fine tuning the fabrication methods and classification algorithm also relays the importance of trial and error to the readers. The novelties in this are listed as such for each chapter.

The development of a skin-electrode system from wearable electrooculogram recordings and human-machine interfacing is outlined in this thesis. A custom algorithm is expressed to readers interested in using a higher accuracy classification method. From top to bottom, the microfabrication process, simulation methods, microcontroller programing and setup of a VR2 controller for wheelchair control is indicated.

Transitioning from the microfabrication process to an aerosol jet printing process is not easy. Geometrical changes in sensor layers is needed to ensure a reliable transfer process. Even then, I've included the limits of designs that are usable for direct writing vs. RIE processing. The atomization process is not easy, especially as inks age, but approximate parameters are described in this thesis for reliable atomization for long-term processing. Limited information is provided on Pneumatic atomization, due to the nature of the PA system, high viscous inks or agglomerating inks may clog the system during a long-term process. The only option as of yet is to maintain parameters at reliable flow rates (600 SCCM< atomizer flow rate <1000 SCCM), above or below those number, it is expect that the virtual impact may clog frequently or the deposition head develops bubbles. However, this thesis sheds light on various materials that can be printed using the AJP and its crystallography changes before and after sintering.

Designing an electrical circuit for electrophysiology recordings is not easy, especially when that design has to be transferred into a tedious program such as AutoCAD. Thin film circuits cause lots of problems with components over heating due to current saturation of passive components. Resistance issues are common with serpentines which reduces the current output of specific ICs from regulators to analog-digital-converters. A functional serpentine design and fabrication process was optimized to ensure these problems do not

occur for future readers. Other circuit considerations here compare BLE to RFID technology. Each has its own purpose and will effect the home based wearable health monitoring differently; lower resolution and sampling rates can be deciphered with batteryless RFID systems whilst, BLE can transmit much further distances with higher sampling rates and resolution using a battery integrated circuit.

Lastly, electrooculogram recordings were highly cited in the 1970s and 1980s; today EOG sees very little use in clinical applications, but more frequently observed in research. There are many different eye tracking methods, some more obtrusive than others. The advantages of EOG includes the mobility and high resolution, especially when skin-electrodes are used. This thesis discovered the conformality of skin-electrodes allows it to be used under a VR headset which cannot have a videooculograms system. Additionally, there is a lack of quantitative measurements of strabismus and convergence insufficiency therapeutics. Typically, a doctor assesses the patient in a qualitative manner and decides a set of metrics to explain the vision based off the patient's feedback. This thesis aims to remove the feedback of the patient and solely measure the eye movement and eye vergence during ocular therapy, especially in VR applications. Furthermore, I do not advise replacing office based vision therapy, but I do recommend the replacement archaic home pencil pushups with a home monitoring system as the gear VR allows. Below I have listed the specific novelties of each chapter as it addresses a broad readership.

1.27.1 Novelties - Chapter 3

(1) Development of new designs of electrodes with simulations and experiments to insure stability of the sensor.

(2) High accuracy classification system using linear discriminant analysis and easy to use features with a real-time logic algorithm.

(3) Integration of skin-electrode with a real-time human-machine interface for wheelchair control

(4) First skin-electrode electrooculogram study; comparison of conventional electrode to skin-electrode; amplitude changes in total areal coverage vs open mesh areal coverage; sensitivity tests

1.27.2 Novelties – Chapter 4

(1) First study of aerosol jet printed films for high throughput sensor fabrication.

(2) Nanoindentation of materials not observed in inkjet printing with the exception of silver nanoparticles.

(3) Tunable mechanical properties of aerosol jet printed films for flexible electronics while retaining conductivity.

(4) Relationship between focusing ratio and geometrical structure of traces for open mesh sensor.

(5) Simulation and experimentation of aerosol jet printed electrode and 3 different fabrication processes.

1.27.3 Novelties – Chapter 5

(1) First aerosol jet printed skin-electrode fabrication, transfer, and use on human subjects for electrooculograms

(2) Accuracy assessment of ocular vergence quality of human subjects in physical and virtual domain.

(3) Implementation of ocular therapies on a VR headset.

(4) Configuration of a flexible, wearable, thin film circuit on the skin for high resolution electrooculogram recordings using Bluetooth low energy system.

(5) First ocular therapeutic system with a real-time observational and classification algorithm with electrooculograms.

(6) First implementation of skin-electronics underneath a VR headset.

(7) Simulation of bending of a serpentine structured flexible thin film circuit.

(8) Fabrication of a flexible, serpentine, thin film circuit

1.27.4 Novelties – Chapter 6

(1) Batteryless RFID system using a integrated sensor front end

(2) Conversion from rigid to soft material platform for skin electronic data acquisition

(3) GSR readings on the wrist

(4) AJP fabricated antenna, circuit, and sensor integrated into a single flexible board.

(5) Atomization of photoresist in ultrasonic atomizer

1.28 Future direction

My recommendation for future readers is sectioned into multiple disciplines. The fabrication expert, the aerosol jet printing expert, the classification and algorithm expert, circuit design expert, and the ocular applications expert.

1.28.1 Fabrication expert

The fabrication expert needs to process and assemble the circuits from thin film metals to soft materials. This person needs to improve the quality of thin-film boards and keep it

cheap. In this case it may be best to electroplate rather than use deposition tools. Furthermore, dry etching is time consuming therefore wet etching, ultrasonic, or laser machining of vias is more advantageous. Additionally, process capability standards need to be implemented for industrial applications by assessing CPK values.

1.28.2 Aerosol jet printing expert

The Aerosol Jet Printing expert needs a strong understanding of chemistry, nanoparticle synthesis, and AJP processing parameters. Skin-electrode sensors are easily fabricated and transferred, but direct printing onto elastomer is desired. However, the commercially available silver inks do not provide low temperature processing on elastomers which is necessary for the high thermal expansion elastomers. Reactive silver inks can process and sinter nanoparticles below 100°C, but they are exclusive to research. Other inks, such as gold, platinum, copper, and nickel are available, but need specialized environments to be sintered to low resistivity. Photonic sintering is an appealing option that uses flash lamp technology, but the cost of the sintering tool can exceed $30,000. Additionally, the AJP system requires continuous maintenance, therefore 24/7 printing may not be possible without multiple deposition heads. In the future the pneumatic atomizer needs an in depth processing study, because of the versatility of that atomizer. Currently, it is limited by its short term processing capabilities.

1.28.3 Classification and algorithm expert

Developing a classifier is not easy but it can be done with the plethora of information available in the literature. Many different neural network classifiers could enable the classification of electrooculograms without specifying statistical features such as mean,

median, max, or wavelet transforms. Some logic algorithms may be necessary for multi class systems in the 1000s of classes. For example, there are 9 points on the eye vergence testing apparatus and a total of 3 distances. An eye gaze or vergence shift from one point to another is one class so there are over 700 possible classes. This is a difficult task to achieve using supervised learning due to the limited data available when gathering electrophysiology data.

1.28.4 Circuit design expert

The circuit design expert has a seeming easy task but in addition to schematic design and routing traces, the same process needs to be assessed on a thin-film board. This complicates the work due to material and geometrical constraints to maintain the board flexible. Additionally, automation from straight line to serpentine structure is needed. Other parameters such as components and sensor distance from amplifiers must also be considered from application to application.

1.28.5 Ocular applications expert

The final expert has the responsibility to determine the feasibility of the application for therapeutics or diagnostics. The current classifier outputs an accuracy for consistent eye vergence signals. If the user deviates any vergence motions, this reduces the accuracy. The accuracy needs to be assessed with unhealthy patients to confirm the reliability of the classification accuracy metric. More applications need to be implemented on the VR headset to provided therapeutics for a 12 week CITT. Strabismus treatment requires consistent readability of texts to be deemed healthy. Additionally, a system that is all inclusive needs to be implemented on the face. For example, a face mold can be developed

for each person with pre-selected electrode positions on the mask for greater precision of the device from day to day therapeutics (Figure 59).

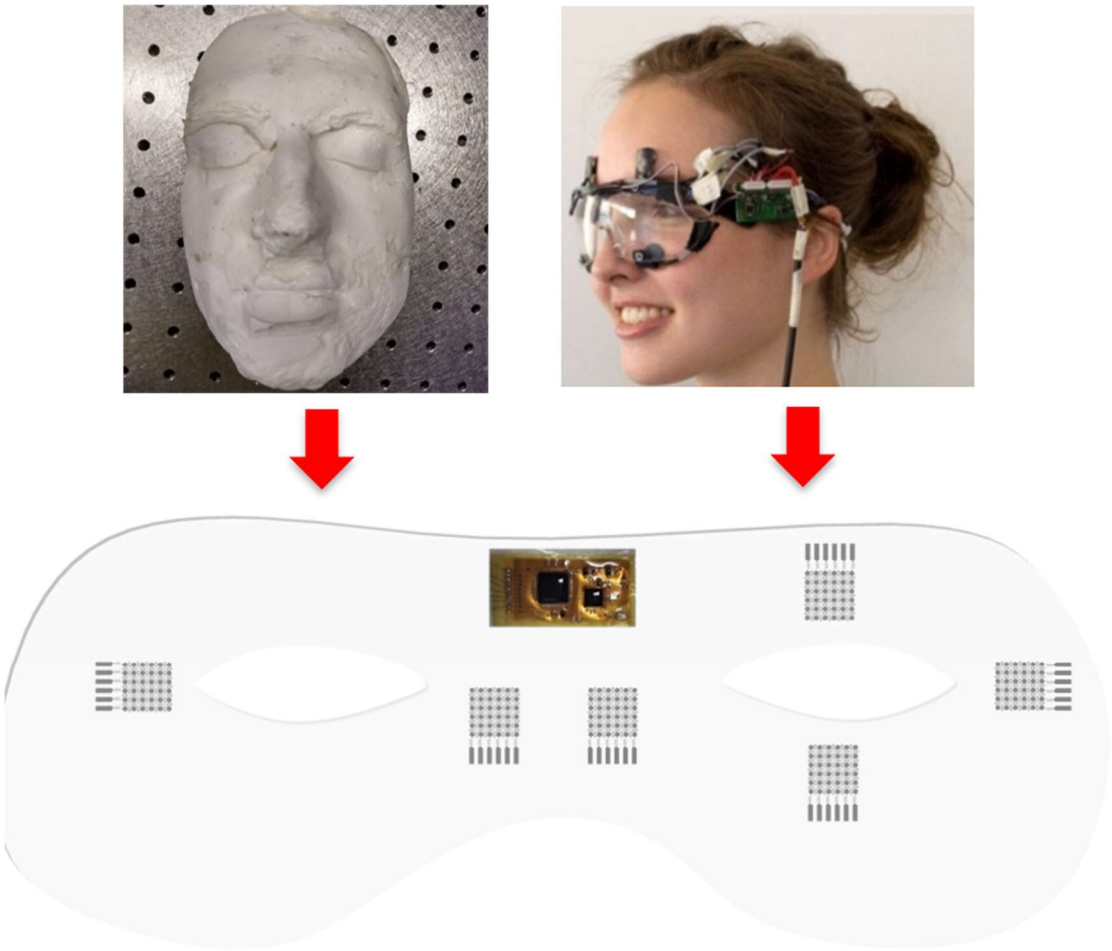

Figure 63. Face mold to develop a custom soft material mask for higher precision eye vergence recordings is recommended during therapeutic clinical trials.

REFERENCES

1. Arrieta, R.A., et al., *Cost–Benefit Analysis of Home Blood Pressure Monitoring in Hypertension Diagnosis and Treatment: An Insurer Perspective.* Hypertension, 2014. **64**(4): p. 891-896.

2. Plans, I.F.o.H., *International Federation of Health Plans 2012 Comparative Price Report: Variation in Medical and Hospital Prices by Country*. 2012. p. 9, 18.

3. Lawson, R.A. and A.P.G. Robinson, *Chapter 1 - Overview of materials and processes for lithography*, in *Frontiers of Nanoscience*, A. Robinson and R. Lawson, Editors. 2016, Elsevier. p. 1-90.

4. Kim, S., S. Lee, and H. Choi, *Review on Fabrication and Manipulation of Scaffold and Ciliary Microrobots.* Hanyang Med Rev, 2016. **36**(4): p. 235-241.

5. Krzeminski, J., et al., *Microscale Hybrid Flexible Circuit Printed With Aerosol Jet Technique.* IEEE Transactions on Nanotechnology, 2018. **17**(5): p. 979-984.

6. ten Kate, J., G. Smit, and P. Breedveld, *3D-printed upper limb prostheses: a review.* Disability and Rehabilitation: Assistive Technology, 2017. **12**(3): p. 300-314.

7. Brault, M.W., *Americans With Disabilities: 2010.* U.S. CENSUS BUREAU, 2012: p. P70-131.

8. Govindan, M., et al., *Incidence and types of childhood exotropia: A population-based study.* Ophthalmology, 2005. **112**(1): p. 104-108.

9. *The Convergence Insufficiency Treatment Trial: Design, Methods, and Baseline Data.* Ophthalmic Epidemiology, 2008. **15**(1): p. 24-36.

10. Alvarez, T.L., et al., *Concurrent Vision Dysfunctions in Convergence Insufficiency with Traumatic Brain Injury.* Optometry and vision science : official publication of the American Academy of Optometry, 2012. **89**(12): p. 10.1097/OPX.0b013e3182772dce.

11. Rouse, M.W., et al., *Validity and reliability of the revised convergence insufficiency symptom survey in adults.* Ophthalmic and Physiological Optics, 2004. **24**(5): p. 384-390.

12. Yazicioglu, R.F., C.V. Hoof, and R. Puers, *Biopotential Readout Circuits for Portable Acquisition Systems*. 2008: Springer Publishing Company, Incorporated. 180.

13. Wu, S.L., et al., *Controlling a Human-Computer Interface System With a Novel Classification Method that Uses Electrooculography Signals.* IEEE Transactions on Biomedical Engineering, 2013. **60**(8): p. 2133-2141.

14. Keegan, J., E. Burke, and J. Condron. *An electrooculogram-based binary saccade sequence classification (BSSC) technique for augmentative communication and control*. in *2009 Annual International Conference of the IEEE Engineering in Medicine and Biology Society*. 2009.

15. Aziz, F., et al., *HMM based automated wheelchair navigation using EOG traces in EEG.* J Neural Eng, 2014. **11**(5): p. 056018.

16. Belkacem, A.N., et al., *Online classification algorithm for eye-movement-based communication systems using two temporal EEG sensors.* Biomedical Signal Processing and Control, 2015. **16**: p. 40-47.

17. Barea, R., et al., *System for assisted mobility using eye movements based on electrooculography.* IEEE Transactions on Neural Systems and Rehabilitation Engineering, 2002. **10**(4): p. 209-218.

18. Fayeem, A., et al., *HMM based automated wheelchair navigation using EOG traces in EEG.* Journal of Neural Engineering, 2014. **11**(5): p. 056018.

19. Bulling, A., et al., *Eye movement analysis for activity recognition*, in *Proceedings of the 11th international conference on Ubiquitous computing*. 2009, ACM: Orlando, Florida, USA. p. 41-50.

20. Mala, S. and K. Latha, *Feature selection in classification of eye movements using electrooculography for activity recognition.* Comput Math Methods Med, 2014. **2014**: p. 713818.

21. Barea, R., et al., *Wheelchair Guidance Strategies Using EOG.* Journal of Intelligent and Robotic Systems, 2002. **34**(3): p. 279-299.

22. Bulling, A., et al., *Eye movement analysis for activity recognition using electrooculography.* IEEE transactions on pattern analysis and machine intelligence, 2011. **33**(4): p. 741-753.

23. Hortal, E., et al., *Combining a Brain–Machine Interface and an Electrooculography Interface to perform pick and place tasks with a robotic arm.* Robotics and Autonomous Systems, 2015. **72**: p. 181-188.

24. Lee, Y. and W.-H. Yeo, *Skin-Like Electronics for a Persistent Brain-Computer Interface.* Journal of Nature and Science, 2015. **1**(7): p. e132.

25. Xu, B., et al., *An Epidermal Stimulation and Sensing Platform for Sensorimotor Prosthetic Control, Management of Lower Back Exertion, and Electrical Muscle Activation.* Advanced Materials, 2015.

26. Jeong, J.W., et al., *Capacitive epidermal electronics for electrically safe, long-term electrophysiological measurements.* Adv Healthc Mater, 2014. **3**(5): p. 642-8.

27. Jeong, J.-W., et al., *Materials and Optimized Designs for Human-Machine Interfaces Via Epidermal Electronics.* Advanced Materials, 2013. **25**(47): p. 6839-6846.

28. Yeo, W.H., et al., *Multifunctional epidermal electronics printed directly onto the skin.* Advanced Materials, 2013. **25**(20): p. 2773-2778.

29. Yeo, W.-H., et al. *Bio-integrated electronics and sensor systems*. in *SPIE Defense, Security, and Sensing*. 2013. International Society for Optics and Photonics.

30. Convergence Insufficiency Treatment Trial Study, G., *Randomized clinical trial of treatments for symptomatic convergence insufficiency in children.* Archives of Ophthalmology, 2008. **126**(10): p. 1336-1349.

31. Talasan, H., et al., *Disparity vergence responses before versus after repetitive vergence therapy in binocularly normal controls.* Journal of Vision, 2016. **16**(1): p. 7-7.

32. Chita-Tegmark, M., *Social attention in ASD: A review and meta-analysis of eye-tracking studies.* Research in Developmental Disabilities, 2016. **48**(Supplement C): p. 79-93.

33. Gorges, M., et al., *Regional microstructural damage and patterns of eye movement impairment: a DTI and video-oculography study in neurodegenerative parkinsonian syndromes.* Journal of Neurology, 2017. **264**(9): p. 1919-1928.

34. Kapoula, Z., et al., *Objective Evaluation of Vergence Disorders and a Research-Based Novel Method for Vergence Rehabilitation.* Translational Vision Science & Technology, 2016. **5**(2): p. 8-8.

35. Hirota, M., et al., *Relationship between reading performance and saccadic disconjugacy in patients with convergence insufficiency type intermittent exotropia.* Japanese Journal of Ophthalmology, 2016. **60**(4): p. 326-332.

36. Gaertner, C., et al., *Binocular coordination of saccades during reading in children with clinically assessed poor vergence capabilities.* Vision Research, 2013. **87**(Supplement C): p. 22-29.

37. Farivar, R. and D. Michaud-Landry, *Construction and Operation of a High-Speed, High-Precision Eye Tracker for Tight Stimulus Synchronization and Real-Time Gaze Monitoring in Human and Animal Subjects.* Frontiers in Systems Neuroscience, 2016. **10**: p. 73.

38. Benjamin, E.J., et al., *Heart Disease and Stroke Statistics—2017 Update: A Report From the American Heart Association.* Circulation, 2017. **135**(10): p. e146-e603.

39. Fan, J.A., et al., *Fractal design concepts for stretchable electronics.* Nat Commun, 2014. **5**.

40. Hattori, Y., et al., *Multifunctional Skin-Like Electronics for Quantitative, Clinical Monitoring of Cutaneous Wound Healing.* Advanced healthcare materials, 2014. **3**(10): p. 1597-1607.

41. Yeo, W.-H., et al., *Multifunctional Epidermal Electronics Printed Directly Onto the Skin.* Advanced Materials, 2013. **25**(20): p. 2773-2778.

42. Norton, J., et al., *Soft, curved electrode systems capable of integration on the auricle as a persistent brain–computer interface*. Vol. 112. 2015.

43. Kim, Y.-S., et al., *Scalable Manufacturing of Solderable and Stretchable Physiologic Sensing Systems.* Advanced Materials, 2017. **29**(39): p. 1701312.

44. Vuorinen, T., et al., *Inkjet-Printed Graphene/PEDOT:PSS Temperature Sensors on a Skin-Conformable Polyurethane Substrate*. Vol. 6. 2016. 35289.

45. Lilah, I., et al., *Printed facial skin electrodes as sensors of emotional affect.* Flexible and Printed Electronics, 2018. **3**(4): p. 045001.

46. Gao, W., et al., *Fully integrated wearable sensor arrays for multiplexed in situ perspiration analysis.* Nature, 2016. **529**(7587): p. 509-514.

47. Lee, Y., et al., *Wireless, intraoral hybrid electronics for real-time quantification of sodium intake toward hypertension management.* Proceedings of the National Academy of Sciences, 2018. **115**(21): p. 5377.

48. Chepesiuk, R., *Where the chips fall: environmental health in the semiconductor industry.* Environmental health perspectives, 1999. **107**(9): p. A452-A457.

49. Wang, Y., J. Bokor, and A. Lee, *Maskless lithography using drop-on-demand inkjet printing method*. 2004. p. 628-636.

50. Kim, M.-H., H. Kim, and D. Paek, *The health impacts of semiconductor production: an epidemiologic review.* International journal of occupational and environmental health, 2014. **20**(2): p. 95-114.

51. Jillek, W. and W.K.C. Yung, *Embedded components in printed circuit boards: a processing technology review.* The International Journal of Advanced Manufacturing Technology, 2005. **25**(3): p. 350-360.

52. Lim, J.-E., D.-Y. Lee, and H.-K. Kim, *Mechanical Stretchability of Screen-Printed Ag Nanoparticles Electrodes on Polyurethane Substrate for Stretchable Interconnectors and Thin Film Heaters.* ECS Journal of Solid State Science and Technology, 2018. **7**(9): p. P468-P472.

53. Seifert, T., et al., *Additive Manufacturing Technologies Compared: Morphology of Deposits of Silver Ink Using Inkjet and Aerosol Jet Printing.* Industrial & Engineering Chemistry Research, 2015. **54**(2): p. 769-779.

54. Xu, B.L., et al., *Aerosol Jet Printing on Radio Frequency IDentification Tag Applications.* Key Engineering Materials, 2013. **562-565**: p. 1417-1421.

55. Rahman, M.T., et al., *3D printed high performance strain sensors for high temperature applications.* Journal of Applied Physics, 2018. **123**(2): p. 024501.

56. Yeo, L.Y. and J.R. Friend, *Ultrafast microfluidics using surface acoustic waves.* Biomicrofluidics, 2009. **3**(1): p. 012002.

57. Chen, Y., et al., *Microstructured Thin Film Nitinol for a Neurovascular Flow-Diverter.* Scientific reports, 2016. **6**.

58. Ma, Y., et al., *Design of Strain-Limiting Substrate Materials for Stretchable and Flexible Electronics.* Advanced Functional Materials, 2016.

59. Zhang, Y., et al., *Experimental and theoretical studies of serpentine microstructures bonded to prestrained elastomers for stretchable electronics.* Advanced Functional Materials, 2014. **24**(14): p. 2028-2037.

60. Hattori, Y., et al., *Multifunctional Skin-Like Electronics for Quantitative, Clinical Monitoring of Cutaneous Wound Healing.* Adv Healthc Mater, 2014.

61. Bao, S., et al., *A New Simple Technique for Making Facial Dimples.* Aesthetic Plastic Surgery, 2007. **31**(4): p. 380-383.

62. Sakharova, N.A., et al., *Comparison between Berkovich, Vickers and conical indentation tests: A three-dimensional numerical simulation study.* International Journal of Solids and Structures, 2009. **46**(5): p. 1095-1104.

63. Howe, C., et al., *Stretchable, Implantable, Nanostructured Flow-Diverter System for Quantification of Intra-aneurysmal Hemodynamics.* ACS Nano, 2018.

64. Xu, W., N. Chahine, and T. Sulchek, *Extreme Hardening of PDMS Thin Films Due to High Compressive Strain and Confined Thickness.* Langmuir, 2011. **27**(13): p. 8470-8477.

65. Juodkazis, K., et al., *XPS studies on the gold oxide surface layer formation.* Electrochemistry Communications, 2000. **2**(7): p. 503-507.

66. Coutts, M.J., et al., *Rapid and Controllable Sintering of Gold Nanoparticle Inks at Room Temperature Using a Chemical Agent.* The Journal of Physical Chemistry C, 2009. **113**(4): p. 1325-1328.

67. Blumenthal, T., et al., *Aerosol Jet® Printing onto 3D and Flexible Substrates.* Quest Integrated Inc., Kent, WA, USA, 2017.

68. Saengchairat, N., T. Tran, and C.-K. Chua, *A review: Additive manufacturing for active electronic components.* Virtual and Physical Prototyping, 2017. **12**(1): p. 31-46.

69. Na Rae, K., et al., *Surface modification of oleylamine-capped Ag–Cu nanoparticles to fabricate low-temperature-sinterable Ag–Cu nanoink.* Nanotechnology, 2016. **27**(34): p. 345706.

70. Socrates, G., *Infrared and Raman Characteristic Group Frequencies*. 3rd ed. John Wiley & Sons, ed. J.W. Sons. 2001: John Wiley & Sons. 362.

71. Hung, G.K., J.L. Semmlon, and K.J. Ciuffreda, *The Near Response: Modeling, Instrumentation, and Clinical Applications.* IEEE Transactions on Biomedical Engineering, 1984. **BME-31**(12): p. 910-919.

72. Mishra, S., et al., *Soft, conformal bioelectronics for a wireless human-wheelchair interface.* Biosensors and Bioelectronics, 2017. **91**: p. 796-803.

73. Herbert, R., et al., *Soft material-enabled, flexible hybrid electronics for medicine, healthcare, and human-machine interfaces.* Materials, 2018. **11**(2): p. 187.

74. Ma, J., et al., *A novel EOG/EEG hybrid human–machine interface adopting eye movements and ERPs: Application to robot control.* IEEE Transactions on Biomedical Engineering, 2015. **62**(3): p. 876-889.

75. Moon, E., et al. *Novel Design of Artificial Eye Using EOG (Electrooculography)*. in *Robotic Computing (IRC), IEEE International Conference on*. 2017. IEEE.

76. Baek, J.-Y., et al., *Flexible polymeric dry electrodes for the long-term monitoring of ECG.* Sensors and Actuators A: Physical, 2008. **143**(2): p. 423-429.

77. Morahan, P., et al., *Ocular Vergence Measurement in Projected and Collimated Simulator Displays.* Human Factors, 1998. **40**(3): p. 376-385.

78. Lions, C., et al., *Binocular Coordination of Saccades During Reading In Strabismic Children.* Investigative Ophthalmology & Visual Science, 2013. **54**(1): p. 620-628.

79. Kassal, P., et al., *Smart bandage with wireless connectivity for uric acid biosensing as an indicator of wound status.* Electrochemistry Communications, 2015. **56**: p. 6-10.

80. Zhou, S., et al., *A Novel Passive Wireless Sensing Method for Concrete Chloride Ion Concentration Monitoring.* Sensors, 2017. **17**(12).

81. Vora, S., K. Dandekar, and T. Kurzweg. *Passive RFID tag based heart rate monitoring from an ECG signal*. in *2015 37th Annual International Conference of the IEEE Engineering in Medicine and Biology Society (EMBC)*. 2015.

82. Rose, D.P., et al., *Adhesive RFID Sensor Patch for Monitoring of Sweat Electrolytes.* IEEE Transactions on Biomedical Engineering, 2015. **62**(6): p. 1457-1465.